Structural and Electrical Characterisation of some ABO_3 Perovskites

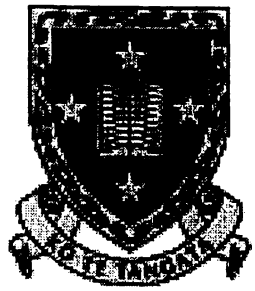

The University of Waikato
Te Whare Wānanga o Waikato

A thesis
submitted in partial fulfillment
of the requirements for the degree of
Doctor of Philosophy
at the University of Waikato
by

Roslyn June Phillips

The University of Waikato, Hamilton, New Zealand
June 1999

Dedication

To my supervisor, for his unending patience and understanding.

Abstract

Powder X-ray diffraction and Raman spectroscopy have been used to characterise the electrolyte materials $La_{1-x}Sr_xGaO_{3-\delta}$ (x = 0-0.2) and $LaGa_{1-y}M_yO_{3-\delta}$ (y = 0-0.2, M = Cr, Mg). XRD of $La_{1-x}Sr_xGaO_{3-\delta}$ (x = 0-0.2) showed the secondary phase of $SrGa_3O_7$ at >5 mol% Sr. The cell deformed with increasing Sr dopant concentration. In the XRD patterns of $LaGa_{1-y}Cr_yO_{3-\delta}$ (y = 0-0.2) the cell also deformed with increasing Cr dopant concentration. The peak at ca. 32° showed a second peak at 32.37°, likely to be due to a phase change, since the peaks did not alter in relative intensity with increase in dopant concentration (above x = 0). $LaGa_{1-y}Mg_yO_{3-\delta}$ (y = 0-0.2) showed, from the powder X-ray diffraction pattern, the formation of the secondary phase of $La_4Ga_2O_9$ at >5 mol% Mg. Raman spectra of $LaGaO_3$ showed 18 features at room temperature, and 14 at −196 °C with the disappearance of the band at 92 cm^{-1}. Raman spectra of the doped material, $LaGa_{1-y}Mg_yO_{3-\delta}$ at y = 0-0.2 showed the formation of a secondary phase of $La_4Ga_2O_9$ with bands at 243, 295 and 356 cm^{-1} which become more predominant at 20 mol% Mg.

$LaFeO_3$ was prepared using a reverse-strike coprecipitation method. The Raman spectrum of $LaFeO_3$ were obtained at both low-temperature and room temperature, with 9 bands observed of a predicted 24 Raman active modes. Mode assignment was determined from comparison of the Raman profile and band position with perovskites with the same structure, namely, $SmAlO_3$ and $LaGaO_3$ and are as follows: 102 (B_{1g}), ca.140 (B_{2g}), 150 (B_{1g}), 176 (A_g), 227 (B_{3g}), 261 (A_g), 289 (A_g), 413 (A_g), 429 (B_{3g}). $LaFe_{1-x}Mg_xO_3$ was prepared using a reverse-strike coprecipitation method. The XRD patterns obtained at room temperature showed single phase, but also included small amounts of impurity of La_2O_3 and La_2MgO_x. Lattice calculations based on $FeLaO_3$ showed that Mg dopant concentration had a minor effect on the overall unit cell volume, with the minimum volume achieved being 241.68Å^3 at 1450 °C, 15%Mg concentration. In summary, Mg-doped $LaFeO_3$ produced a single phase material in the range 0-20 mol% Mg as observed from X-ray diffraction. However, a small amount of impurities in each of the samples was observed, containing La_2O_3 and La_2MgO_x. The presence of the impurities suggested that an extra calcination step be included in the processing of the material.

$LaGdO_3$ was fabricated using reverse strike co-precipitation method and sintered at temperature of 1350, 1400 and 1450 °C. X-ray diffraction showed the presence of a single monoclinic phase. Raman spectroscopy showed a spectrum similar for that reported for the B-type rare earth oxide Gd_2O_3 and the band positions of the low temperature Raman spectrum were assigned in comparison with this. A total of 18 bands were identified. Intense broad profile in the region 1000-2000 cm^{-1} was observed for $LaGdO_3$, likely due to fluorescent/luminescent bands.

The acceptor-doped perovskite proton conductor $SrCe_{1-x}Y_xO_{3-\delta}$ (x=0.025 to 0.20, δ = x/2) was prepared and characterised using X-ray diffraction and AC impedance spectroscopy, and the effect of the yttrium dopant concentration on structure and electrical properties has been investigated. X-ray diffraction studies showed a decrease in lattice volume with increasing yttrium content. Electrical conductivity

studies were made as a function of oxygen partial pressure, and a partial pressure of water vapour of 0.001 and 0.01 atm. The total conductivity was separated into different components by fitting procedures and regions of ionic and *p*-type conduction were identified. At 800°C, and at the water vapour partial pressure of 0.01 atm, the ionic conductivity showed a maximum at a doping level of $x = 0.10$, reaching a value of 5 mS/cm. The conductivity component appearing at low oxygen partial pressure, which according to recent studies may be regarded as protonic rather than *n*-type, decreased with doping, while the *p*-type component at high oxygen partial pressure increased.

Acknowledgments

There is a vast amount of people that have assisted and influenced me over the time frame of my Ph.D. First and foremost is my supervisor, Professor Nigel Sammes, and I would like to thank him for his support (both financial and mental), knowledge and encouragement throughout the length of my thesis.

To my other supervisors, I would like to thank Dr. Geoff Tompsett, for his Raman spectroscopy expertise and overall helpfulness and selflessness. To Dr. Mike Fee of IRL in Lower Hutt, thanks for being available if I needed another ear. To Dr. Nikos Bonanos of Risø National Laboratories in Denmark, many thanks for the opportunity to study with you again, and thanks to NEDO of Japan for the financial assistance while in Denmark. Also thanks to Finn Willy Poulsen and Eric Ahlgren of Risø for their assistance with my research and the paper we four have published.

To my parents, sister, brother-in-law and new nephew, many thanks for the support, encouragement and inspiration over the last few years. To Joseph, words cannot express my deepest gratitude for your love and support.

No research can be undertaken smoothly without the assistance of Lab staff, so my thanks to the staff, both in New Zealand and Denmark, whom made my studies that little bit easier, especially to Yuangi and Kjel.

A smile costs nothing and gives so much, so to the people that made things fun, thanks to Mike Brown, Charles Hatchwell, Mike Phillipps, Bazz Fenton, Luisa Andruzzi, Johannes Reynisson, Darja Kek, Lutz Kindermann, Stefan Garber, Olga Marina, Tracy and Ivan Murray, Robert Torrens, Russell Cross, Matt Henderson, Reinder Boersma, Karen Murphy, Emma Sammes, Bill Munro, Garrett Butt, Jenny Richmond, John Davidson, Angela, Garry and Oliver Vincent, the Waitomo Rugby Club, Niels, Anita, Maja and Anders Tiedje and of course, the ever present technology secretary, Lesley Falconer.

Many thanks to the Monckton Trust and Geoff and Helen Monckton for their support and interest in my progress. To Grant Anderson, thank you for helping me keep it all in perspective.

And finally, thank you to the University of Waikato for the financial assistance and opportunity to study. To Gwenda Pennington, my grateful thanks for all your efforts.

Chapter One: Introduction Part I Introduction to ABO_3 Perovskite Oxide Ion Conductors

Chapter Two: Introduction Part II Introduction to ABO_3 Perovskite Protonic Conductors

Chapter Three: Experimental Methods for ABO_3 Perovskite Oxide Ion Conductors

Chapter Four: Experimental Methods for ABO_3 Perovskite Protonic Conductors

Chapter Five: Theory of Techniques

Chapter Six: Results and Discussion for ABO_3 Perovskite Oxide ion conductors

Chapter Seven: Results and Discussion for ABO_3 Perovskite Protonic conductors

Chapter Eight: Conclusions and Recommendations

Index of Figures

Index of Tables

Glossary

Abbreviations used in this text:

LSGM	$La_{1-x}Sr_xGa_{1-y}Mg_yO_{3-\delta}$, where x=0-0.2 and y=0-0.2
XRD	X-ray Diffraction
RT	Room Temperature
TEC	Thermal expansion coefficient
YSZ	yttria stabilised zirconia
MOR	Modulus of Rupture
CSZ	calcia stabilised zirconia
FET	Field effect transistor
EMF	Electromotive Force
SOFC	Solid oxide fuel cell
SIMS	Secondary ion mass spectrometry
HTPC	High temperature proton conductor
PSZ	Yttria partially stabilised zirconia
M	concentration
IS	Impedance spectroscopy
UCV	unit cell volume
LT	Low Temperature
HT	High Temperature

SI units have been used throughout this thesis. However, °C has been retained where appropriate as a convenient unit as used by P.W. Atkins, Physical Chemistry, Third Edition, Oxford University Press, (1998). The most common units used in this thesis are listed below:

Molar percentage concentration	mol%
Pressure	atm. = 1.01325×10^5 Nm^{-2} (Pa) also Mpa (10^6 Nm^{-2})
Wavenumber (or Raman Shift)	cm^{-1}
Length	mm (10^{-3} m)
Wavelength	nm (10^{-9} m)
Conductivity	Scm^{-1}
Concentration	M ($molL^{-1}$)
Frequency	Hz (s^{-1})
Lattice Parameters	Å (10^{-10}m)
Time	min. (minute) and h. (hour)
Density	gcm^{-3}
Thermal expansion coefficient	$°C^{-1}$
Laser power	mW (10^{-3} W)

Chapter One

Introduction to ABO_3 Perovskite Oxide Ion Conductors

1.1 Introduction

Chapter one examines the structures adopted by ABO_3 type perovskite materials and gives an overview of a number of the perovskite materials used in fuel cell applications. This chapter also outlines properties that lead to, and enhance, their conductivity, and briefly examines some of their applications. The materials examined in this thesis are ABO_3 type perovskites where A = La and B = Ga, Fe and Gd.

1.2 Perovskites

1.2.1 Introduction

There are a vast number of oxides having two or more different kinds of cation. Most of them occur in one of a few basic structural types, the names of which are derived from the first or principal compound shown to have that type of structure. There are three main structures that oxides adopt, the spinel, the ilmenite and the perovskite structure. As the perovskite structure is the structure observed for $LaGaO_3$ based materials[1] it is therefore examined in detail.

1.2.2 The Perovskite Structure

Over the past 35 years, the class of materials known as perovskites or pseudo-perovskites has received a considerable amount of attention. This is because these compounds display many useful properties, for example, high melting points, tailored electrical properties, ferroelectricity, and ferromagnetism[2].

The perovskite structure can be represented by the general formula ABO_3 in which A, the large cation site, may be an alkali, alkaline earth, or rare earth ion, and B, the small cation site, a transition metal cation. The mineral 'perovskite' ($CaTiO_3$) has a structure in which the oxide ions and the large cation (Ca^{2+}) form a *ccp* (cubic close packed) array with the smaller cation (Ti^{4+}) occupying those octahedral holes formed exclusively by oxide ions, as shown in Figure 1.1. The crystal structure itself is a very simple one. The structure in its idealised form is cubic, with Ti^{4+} ions at the corners of the unit cell, a Ca^{2+} ion at the body centre, and O^{2-} ions at the mid-points of the edges; this A-type cell is shown in Figure 1.1(a). When the origin of the cubic unit cell is taken at the Ca^{2+} ion, then the Ti^{4+} ion occupies the body centre and the O^{2-} ions occupy the face centres; this B-type unit cell is shown in Figure 1.1(b).

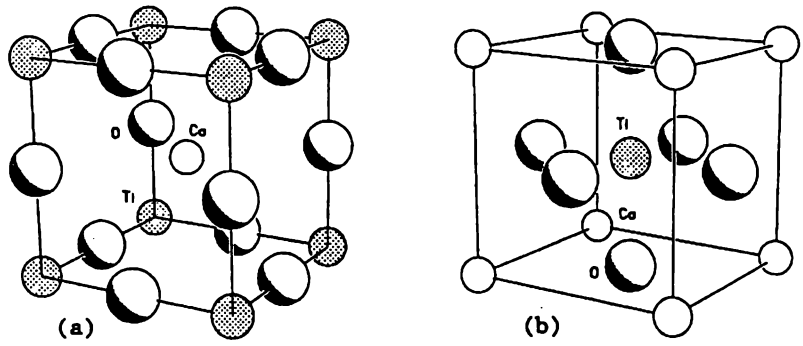

Figure 1.1 (a) A-type and (b) B-type unit cell of perovskite[3] where Ca = Ca^{2+}, Ti = Ti^{4+} and O = O^{2-}.

Each Ca^{2+} ion is thus 12 co-ordinated with each Ti^{4+}, which is 6 co-ordinated by oxygen neighbours, while each O^{2-} is linked to four Ca^{2+} and two Ti^{4+} ions. It is the larger metal ion which occupies the site of higher co-ordination[3].

The perovskite structure is often slightly distorted, as observed in $CaTiO_3$, for example[4]. This structure is adopted by many ABO_3 oxides in which one cation is comparable in size to O^{2-}, and the other much smaller, with the cation charges variable so long as their sum is +6; this is found in $Sr^{II}Ti^{IV}O_3$, $Ba^{II}Ti^{IV}O_3$, $La^{III}Ga^{III}O_3$, $Na^{I}Nb^{V}O_3$, and $K^{I}Nb^{V}O_3$[4].

Many ABO_3 crystals give simple diffraction patterns that can be accounted for in terms of a cubic cell containing one formula unit, like $CaTiO_3$. Some of these have true cubic symmetry, whereas others, owing to strain or to small departures from perfect cubic symmetry, have appreciably distorted atomic arrangements. A large number of the ABO_3 compounds are orthorhombic, rhombohedral or tetragonal, but are so close to cubic that they can be approximated by the cubic structure. These pseudo-perovskite compounds encompass the majority of the ABO_3 compounds, e.g. $BaTiO_3$ (tetragonal), $LaCrO_3$ (orthorhombic), $LaAlO_3$ (rhombohedral), $SrZrO_3$ (orthorhombic), $CaZrO_3$ (orthorhombic) and $NaNbO_3$ (orthorhombic). Because ionic size rather than valency primarily determines the interchangeability of cations in this type of structure, it is possible to substitute selectively for either the A or B ion by introducing isovalent or aliovalent ions. This means that there is the possibility to alter physical properties by making systematic composition changes.

A number of the materials studied in this work have an orthorhombic P*nma* structure. Table 1.1 lists the seven crystal systems with their parameters and lattice symmetry. Figure 1.2 illustrates a unit cell with the parameters shown, as are listed in Table 1.1.

Table 1.1. The Seven Crystal Systems[4].

Crystal System	Number of Independent Parameters	Parameters	Lattice Symmetry
Triclinic	6	$a\neq b\neq c$; $\alpha\neq\beta\neq\gamma$	1-
Monoclinic	4	$a\neq b\neq c$; $\alpha=\gamma=90°$; $\beta>90°$	2/*m*
Orthorhombic	3	$a\neq b\neq c$; $\alpha=\beta=\gamma=90°$;	*mmm*
Tetragonal	2	$a=b\neq c$; $\alpha=\beta=\gamma=90°$;	4/*mmm*
Trigonal Rhombohedral lattice	2	$a=b=c$; $\alpha=\beta=\gamma\neq90°$;	3-*m*
Hexagonal Lattice	2	$a=b=c$; $\alpha=\beta=90°$; $\gamma=120°$	6/*mmm*
Hexagonal	2	$a=b=c$; $\alpha=\beta=90°$; $\gamma=120°$	6/*mmm*
Cubic	1	$a=b=c$; $\alpha=\beta=\gamma=90°$	*m*3*m*

Lattice symmetry is a fundamental part of a crystal structure description. It should be noted that 3- is a 3-fold rotary inversion axis, i.e., a rotation of 360°/3 and then an inversion through the origin which gives a position coincident with the initial position. The symbols 2/*m* for the monoclinic lattice indicate a 2-fold axis with a mirror plane perpendicular to it. The symmetry of the orthorhombic lattice is designated by *mmm*, indicating three mutually perpendicular mirror planes.

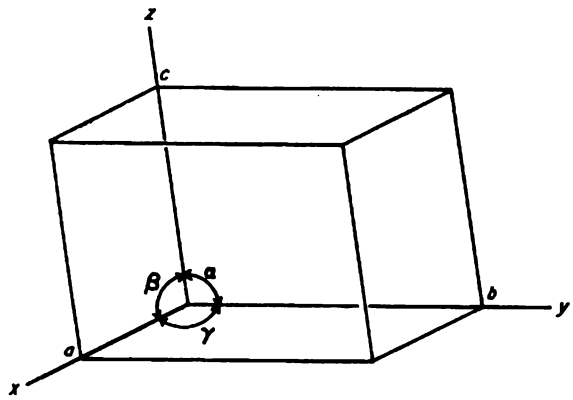

Figure 1.2 A basic unit cell of a general crystal identifying parameters listed in Table 1.1[4].

The simple lattice in each of the crystal systems in Table 1.1 have lattice points only at the corners of the unit cell, ie. there is the equivalent of one lattice point per unit

cell. Such lattices are termed primitive and are designated by the letter P preceding the symmetry symbols (except in the rhombohedral lattice, where R is used). Thus the seven primitive lattices are denoted as P1-, P2/*m*, P*mmm*, P4/*mmm*, R3-*m*, P6/*mmm* and P*m*3*m*.

1.3 Structure and Crystallographic Information

1.3.1 Introduction

The perovskite materials used in electrochemical devices typically consist of doped – gallate, manganite, ferrite, cobaltite and chromite based materials. These can be divided into types used for differing functions based on their inherent conductivity properties. These are typically electrolyte materials, such as doped lanthanum gallate, interconnect materials that require high electronic conductivity, such as lanthanum chromite and lanthanum ferrite, and cathode materials such as lanthanum manganite and lanthanum cobaltite. The structures of these components typically fall into either the orthorhombic or rhombohedral perovskite modification. Tables 1.2 to 1.8 list the literature data of structures, space groups and sample preparation methods for various perovskites based on gallate oxygen ion conductors, rare earth ferrites, chromites, manganites and cobaltites. Also included are tables that cover gadolinium-based perovskites and other various perovskite materials not grouped under the initial listed headings.

1.3.2 ABO_3 Structure where B = Ga

In 1957 Geller reported the structure of $LaGaO_3$ as being orthorhombic at room temperature, having the space group P*bnm*[5]. He also reported the high temperature (above 900 °C) phase to be rhombohedral. Later, Ishihara et al.[1] reported the structure of both $LaGaO_3$ and doped $LaGaO_3$ ($La_{1-x}Sr_xGa_{1-y}Mg_yO_{3-\delta}$, known as LSGM where x=0-0.2 and y=0-0.2 and δ is the oxygen deficiency per unit formula, normally x/2) to be orthorhombic at room temperature. Feng and Goodenough[6] also reported $LaGaO_3$ to be an orthorhombic perovskite (a=5.20 Å, b=7.752 Å, and

c=5.487 Å), iso-structural with $GdFeO_3$, but found that the structure of $La_{0.9}Sr_{0.1}Ga_{0.8}Mg_{0.2}O_{2.85}$ was a cubic perovskite, where a=3.911±0.003 Å. Studies since 1994 have predominantly reported all LSGM variations to be an orthorhombic perovskite at room temperature, refined to the space group of P*nma* (No. 62), with lattice parameters a=5.494 Å, b=5.525 Å and c=7.776 Å[7]. However, Huang et al.[8] reported $La_{0.85}Sr_{0.15}Ga_{0.85}Mg_{0.15}O_{2.85}$ to be a pseudocubic perovskite with lattice parameters varying according to doping concentrations x (A site variation) and y (B site variation). They constructed a quaternary $La_{0.15}$-SrO-$GaO_{1.5}$-MgO phase diagram, based on powder X-ray diffraction, identifying the single phase field for the cubic perovskite and two different impurities indexed to $LaSrGaO_4$ and $LaSrGa_3O_7$[8], as shown in Figure 1.3.

Subsequent studies on LSGM have found that the perovskite structure will only tolerate a very limited amount of A-site cationic deficiency in its lattice before the secondary phases indexed by Huang et al.[8], begin to form.

High temperature structural analysis using X-ray diffraction has shown there to be a change from the room temperature structure to a rhombohedral R-*3c* structure at approximately 145 °C [8] to 150 °C[9] for pure $LaGaO_3$, and 172 °C for doubly doped $LaGaO_3$[8], and $LaGaO_3$ is completely rhombohedral by 1000 °C, where a=3.925 Å[6].

Subsequent studies into doped $LaGaO_3$ have lead to the addition of other A and B site cations, including Pr and Nd for the A site and Mn, Fe, In, Al, Cr, and Fe for the B site. Ishihara et al.[10] have shown that substitution of La with Nd in $La_{0.9}Sr_{0.1}Ga_{0.8}Mg_{0.2}O_{3\pm\delta}$ suppresses the p-type conduction under high oxygen partial pressure, although no mechanism for this effect was described. Later work by Baker et al.[11] showed that small additions of Fe or Cr in $La_{0.9}Sr_{0.1}Ga_{1-x}Mg_xO_{3\pm\delta}$ (M = Fe or Cr from 0 to 0.2) increases the p-type conductivity. Ishihara et al.[12] investigated the change in the electrical properties of $La_{0.8}Sr_{0.2}Ga_{0.8}(Mg,Co)_{0.2}O_{3\pm\delta}$ with increasing Co dopant, and showed that the electrical conductivity of the material increased with increasing Co content; the conductivity of $La_{0.8}Sr_{0.2}Ga_{0.8}Mg_{0.05}Co_{0.15}O_{3\pm\delta}$, for example, was observed as being approximately 0.6 Scm^{-1} at 850 °C.

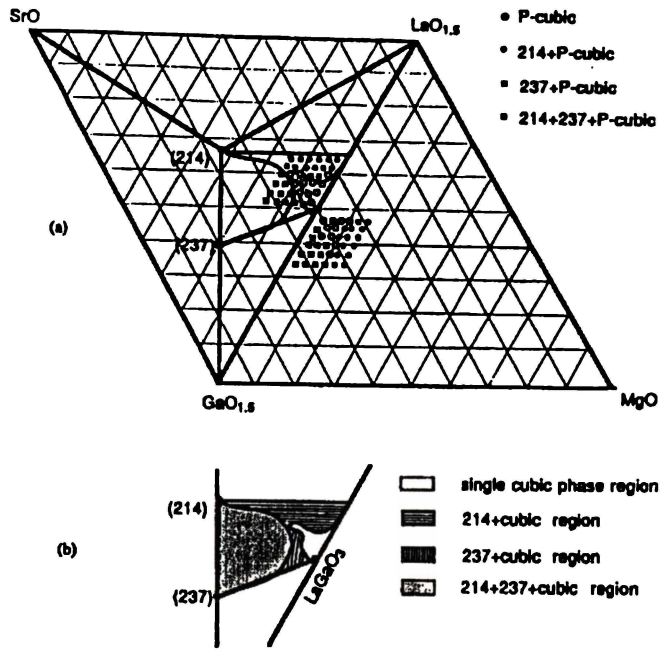

Figure 1.3. Quaternary phase diagram of $LaO_{1.5}$-SrO-$GaO_{1.5}$MgO up to 800 °C; three-phase, and single phase regions are shown: (a) overall look and (b) enlarged multiphase region. Reproduced from Huang et al.[8] where p-cubic = primitive cubic, 214 = $LaSrGaO_4$ and 237 = $LaSrGa_3O_7$.

1.3.2.1 Synthesis of the ABO_3 Structure where B = Ga

Most syntheses of gallate based materials is based on the solid state mixing technique, measuring and mixing the oxides at the required stoichiometry, then calcination and sintering. However, co-precipitation[13] and other techniques[14,15] have been shown to give finer particle sizes and therefore lead to greater densification of the material and the reduction of some glassy phases formed, which are not necessarily apparent in powder X-ray diffraction[16].

Huang et al.[16] prepared LSGM using a sol-gel synthesis technique. Their results showed that a single phase material could be realised by this technique, but it was more difficult to obtain a dense ceramic, in comparison with the solid state method. Huang et al.[8] also found that the synthesis of stoichiometric $La_{1-x}Sr_xGa_{1-y}Mg_yO_{3-0.5(x+y)}$ required calcination of the nominal La_2O_3 and MgO or $MgCO_3$ being used in the initial mix. Figure 1.4 shows the effect of using

commercial MgO versus MgO that had been precalcined or have come from $MgCO_3$. The relatively small formula weight of MgO makes small errors in weighing translate to large errors in the final composition.

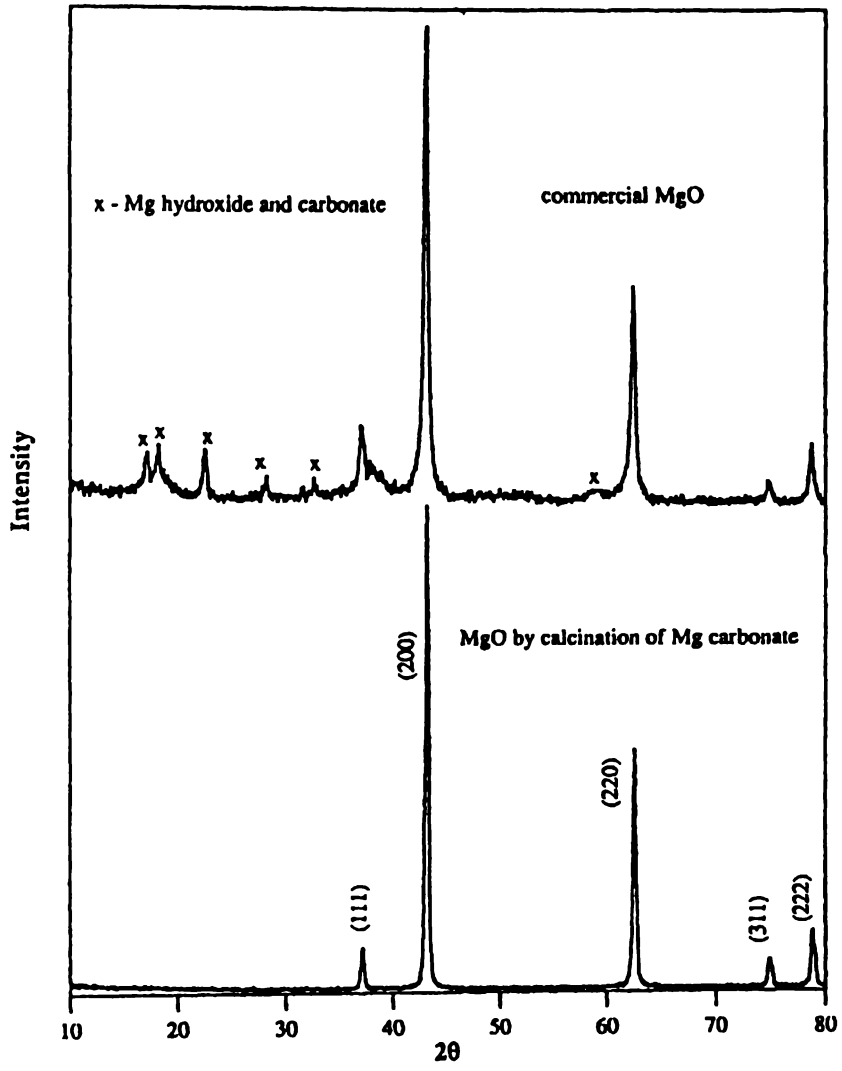

Figure 1.4. X-ray diffraction patterns of undried and dried commercially available MgO, reproduced from Huang et. al.[8]

Table 1.2 Structure for various gallate based perovskites

Compound	Structure	Space group	Preparation	Reference
$LaGaO_3$	Orthorhombic	*Pbnm*	Solid state reaction, 1000 °C/10h calcine, 1500 °C/10h sinter	17
$LaGaO_3$	Orthorhombic	*Pbnm*	Single crystal	18
$LaGaO_3$	Orthorhombic	*Pnma*	Solid State reaction, 700 °C/1 calcine, 1500 °C/6h sinter	19
$LaGaO_3$	Orthorhombic		Solid State reaction	20
$LaGaO_3$	RT, Ortho-rhombic, Rhombohedral >150 °C	*Pbnm* *R3-c*	Single crystals grown in Czochralski system	21
$LaGaO_3$	RT Ortho-rhombic 151 °C - rhombohedral		Single crystal by stoichiometric melt	7
$LaGaO_3$	Orthorhombic-Rhombohedral transition	877 °C		22
$LaGaO_3$	Orthorhombic		Solid state reaction, 1300 °C/24h calcine, 1430-1500 °C/24h	23
$LaGaO_3$	Orthorhombic	*Pnma* (no 62)	Solid state reaction, 1150 °C/4h calcine, 1450 °C/15h sinter	9
$LaGaO_3$	Orthorhombic		Solid state reaction	1
$La_{0.9}Sr_{0.1}GaO_3$	Orthorhombic		Solid state reaction, 1500 °C/4h calcine, 1500, 1550, 1600 °C /4h sinter	24
$La_{0.95}Sr_{0.05}GaO_{3-\delta}$	Orthorhombic		Solid state reaction, 1100 °C/12h calcine, 1500 °C/4h sinter	25
$La_{0.9}Sr_{0.1}GaO_{3-\delta}$	Orthorhombic	*Pbnm*	Solid state reaction 1300 °C/10h calcine, 1500 °C/10h sinter	26
$La_{1-x}Sr_xGaO_3$ (x=0.05-0.2)	Orthorhombic (distorted)		Solid State reaction, 700 °C/1 calcine, 1500 °C/6h sinter	19
$La_{0.9}Sr_{0.1}GaO_3$	Orthorhombic		Solid state reaction 1000 °C/6h calcine, 1500 °C/6h sinter.	1
$La_{0.9}Sr_{0.1}GaO_3$	Orthorhombic		Solid state reaction, 1150 °C/4h calcine, 1450 °C/15h sinter	9
$LaSrGa_3O_7$	Tetragonal	*P421m* (No 113)	Solid state reaction, 1250 °C/8h calcine, 1470 °C/36h sinter	27
$LaSrGaO_4$	Tetragonal	*I4/mmm*	Solid state reaction, 1250 °C/8h calcine, 1470 °C/36h sinter	27
$LaGa_{1-x}Mg_xO_3$ (x=0.05-0.2)	Orthorhombic (distorted)		Solid State reaction, 700 °C/1 calcine,	19

			1500 °C/6h sinter	
$La_{0.9}Sr_{0.1}Ga_{0.8}Mg_{0.2}O_{2.85}$	Primitive Cubic		Co-precipitation/ peptization, 1350 °C/ 36h sinter	16
$La_{0.9}Sr_{0.1}Ga_{0.8}Mg_{0.2}O_{2.85}$	Primitive cubic		Solid state reaction, 1250 °C/8h calcine, 1470 °C/36h sinter	28
$La_{1-x}Sr_xGa_{1-y}Mg_yO_3$ (where x=0.1-0.2 and y=0.15-0.25	Cubic			23, 29
$La_{0.9}Sr_{0.1}Ga_{0.8}Mg_{0.2}O_{2.85}$	Orthorhombic		Solid state reaction, 1150 °C/4h calcine, 1450 °C/15h sinter	9
$La_{0.9}Sr_{0.1}Ga_{0.75}Mg_{0.25}O_{2.825}$	Cubic		Solid state reaction, 1150 °C/4h calcine, 1450 °C/15h sinter	9
$La_{0.85}Sr_{0.15}Ga_{0.8}Mg_{0.2}O_{2.825}$	Cubic		Solid state reaction, 1150 °C/4h calcine, 1450 °C/15h sinter	9
$La_{0.8}Sr_{0.2}Ga_{0.85}Mg_{0.15}O_{2.825}$	Cubic		Solid state reaction, 1150 °C/4h calcine, 1450 °C/15h sinter	9
$La_{0.9}Sr_{0.1}Ga_{0.8}Mg_{0.2}O_{2.85}$	Orthorhombic (RT)	*Pnma* (no 62)	Solid state reaction, 1150 °C/4h calcine, 1450 °C/15h sinter	9
$La_{0.9}Sr_{0.1}Ga_{0.8}Mg_{0.2}O_{2.85}$	Rhombohedral at T=172 °C	*R3c*	Solid state reaction, 1150 °C/4h calcine, 1450 °C/15h sinter	9
$La_{0.9}Sr_{0.1}Ga_{0.8}Mg_{0.2}O_{3-\delta}$	Cubic		Solid state reaction, 1350 °C/20h calcine, 1450 °C/20h sinter	30
$La_{0.8}Sr_{0.2}Ga_{1-y}Mg_yO_{3-0.5(0.2+y)}$	Primitive Cubic (y=0.05-0.15) +$LaSrGa_3O_7$		Solid state reaction, 1250 °C/8h calcine, 1470 °C/36h sinter	27
$La_{0.8}Sr_{0.2}Ga_{1-y}Mg_yO_{3-0.5(0.2+y)}$	Primitive Cubic (y=0.2)		Solid state reaction, 1250 °C/8h calcine, 1470 °C/36h sinter	27
$La_{0.8}Sr_{0.2}Ga_{1-y}Mg_yO_{3-0.5(0.2+y)}$	Primitive Cubic (y=0.25-0.3) + $LaSrGaO_4$		Solid state reaction, 1250 °C/8h calcine, 1470 °C/36h sinter	27
$La_{0.9}Sr_{0.1}Ga_{0.9}Mg_{0.1}O_3$	Orthorhombic		Solid state reaction 1000 °C/6h calcine, 1500 °C/6h sinter.	1
$La_{0.85}Sr_{0.15}Ga_{0.85}Mg_{0.15}O_{2.85}$	Primitive Cubic	*Pm3m*	Solid State reaction 1250 °C/8h calcine, 1470 °C/24h sinter (air quench at 500 °C)	8
$La_xSr_{1-x}Ga_{1-y}Mg_yO_{3-x+y/2}$	Primitive Cubic + impurities of $LaSrGaO_4$ and $LaSrGa_3O_7$	Where x=0.05, 0.1, 0.15, 0.2, 0.25, 0.3 and y=0.05, 0.1, 0.15, 0.2, 0.25, 0.3	Solid State reaction 1250 °C/8h calc., 1470 °C/24h sint (air quench at 500 °C)	8
$LaGa_{1-x}Cr_xO_3$ (x=0.05-0.2)	Orthorhombic		Solid State reaction,	19

	(distorted)		700 °C/1 calcine, 1500 °C/6h sinter	
$La_{0.9}Sr_{0.1}Ga_{0.95}Cr_{0.05}O_3$	Orthorhombic		Solid state reaction, 1500 °C/4h calcine, 1500, 1550, 1600 °C/ 4h sinter	24
$La_{0.9}Sr_{0.1}Ga_{0.8}Cr_{0.2}O_3$	Orthorhombic		Solid state reaction, 1500 °C/4h calcine, 1500, 1550, 1600 °C/ 4h sinter	24
$La_{0.9}Sr_{0.1}(Ga_{0.9}Cr_{0.1})_{0.8}Mg_{0.2}O_{3-x+\delta}$	Cubic		Solid state reaction, 1350 °C/20h calcine, 1450 °C/20h sinter	30
$La_{0.9}Sr_{0.1}(Ga_{0.8}Co_{0.2})_{0.8}Mg_{0.2}O_{3-x+\delta}$	Hexagonal		Solid state reaction, 1350 °C/20h calcine, 1450 °C/20h sinter	30
$La_{0.9}Sr_{0.1}(Ga_{0.75}Co_{0.25})_{0.8}Mg_{0.2}O_{3-x+\delta}$	Hexagonal		Solid state reaction, 1350 °C/20h calcine, 1450 °C/20h sinter	30
$La_{0.9}Sr_{0.1}(Ga_{0.7}Co_{0.3})_{0.8}Mg_{0.2}O_{3-x+\delta}$	Hexagonal		Solid state reaction, 1350 °C/20h calcine, 1450 °C/20h sinter	30
$La_{0.85}Sr_{0.1}(Ga_{0.9}Co_{0.1})_{0.8}Mg_{0.2}O_{3-x+\delta}$	Hexagonal		Solid state reaction, 1350 °C/20h calcine, 1450 °C/20h sinter	30
$La_{0.9}Sr_{0.1}(Ga_{0.9}Co_{0.1})_{0.8}Mg_{0.2}O_{3-x+\delta}$	Cubic		Solid state reaction, 1350 °C/20h calcine, 1450 °C/20h sinter	30
$La_{0.9}Sr_{0.1}(Ga_{0.9}Mn_{0.1})_{0.8}Mg_{0.2}O_{3-x+\delta}$	Cubic		Solid state reaction, 1350 °C/20h calcine, 1450 °C/20h sinter	30
$La_{0.9}Sr_{0.1}Ga_{0.9}Fe_{0.05}O_3$	Orthorhombic		Solid state reaction, 1500 °C/4h calcine, 1500, 1550, 1600 °C/ 4h sinter	24
$La_{0.9}Sr_{0.1}Ga_{0.8}Fe_{0.2}O_3$	Orthorhombic		Solid state reaction, 1500 °C/4h calcine, 1500, 1550, 1600 °C/ 4h sinter	24
$La_{0.9}Sr_{0.1}(Ga_{0.9}Fe_{0.1})_{0.8}Mg_{0.2}O_{3-x+\delta}$	Cubic		Solid state reaction, 1350 °C/20h calcine, 1450 °C/20h sinter	30
$La_{0.9}Sr_{0.1}(Ga_{0.8}Fe_{0.2})_{0.8}Mg_{0.2}O_{3-x+\delta}$	Cubic		Solid state reaction, 1350 °C/20h calcine, 1450 °C/20h sinter	30
$La_{0.9}Sr_{0.1}(Ga_{0.7}Fe_{0.3})_{0.8}Mg_{0.2}O_{3-x+\delta}$	Cubic		Solid state reaction, 1350 °C/20h calcine, 1450 °C/20h sinter	30
$La_{0.85}Sr_{0.1}(Ga_{0.9}Fe_{0.1})_{0.8}Mg_{0.2}O_{3-x+d}$	Cubic		Solid state reaction, 1350 °C/20h calcine, 1450 °C/20h sinter	30
$La_{0.9}Sr_{0.1}Ga_{0.9}In_{0.1}O_3$	Orthorhombic		Solid state reaction 1000 °C/6h calcine, 1500 °C/6h sinter.	1
$La_{0.9}Sr_{0.1}Ga_{0.9}Al_{0.1}O_3$	Orthorhombic		Solid state reaction 1000 °C/6h calcine, 1500 °C/6h sinter.	1
$3Ln_2O_3.5Ga_2O_3$ (Ln=Nd, Sm, Eu,	Garnet type	*Ia3d*		31

Gd, Dy, Ho, Er, Yb)				
$LnGaO_3$, (Ln=La, Pr, Nd)	Perovskite type	($LaGaO_3$ reversible ortho-rhombic/ rhombo. trans. at 900 °C		31
$2Ln_2O_3.Ga_2O_3$ (Ln=La, Pr, Nd, Sm, Eu, Gd)	Monoclinic			31
$Ln_2O_3.Ga_2O_3$ (Ln=Sm, Eu, Gd, Dy, Ho, Er)	Orthorhombic			31
$NdGa_{1-y}Mg_yO_3$ where y=0-0.15	Orthorhombic	JCPDS # 21-0972	Solid state reaction, 1300 °C/24h cal, 1350-1500 °C/24h sinter	32
$Nd_{1-x}Sr_xGaMg\text{-}O_{3-\delta}$ where x<0.1	Orthorhombic		Solid state reaction, 1300 °C/24h cal, 1350-1500 °C/24h sinter from oxides & carbonates.	32
$Nd_{1-x}Ca_xGaMgO_{3-\delta}$ where x<0.1	Orthorhombic		Solid state reaction, 1300 °C/24h cal, 1350-1500 °C/24h sinter	32
$NdGaO_3$	Orthorhombic		Single crystal by stoichiometric melt	7
$NdGaO_3$	Orthorhombic	P*bn*21		20
$NdGaO_3$	RT, Orthorhombic	P*bnm*	Single crystals grown in Czochralski system	21
$PrGaO_3$	Orthorhombic		Single crystal by stoichiometric melt	7
$PrGaO_3$	Orthorhombic			20
$PrGaO_3$	RT, Orthorhombic	P*bnm*	Single crystals grown in Czochralski system	21

1.3.3 ABO_3 Structure where B = Fe

Strontium substituted lanthanum ferrites, such as $La_{1-x}Sr_xFeO_{3-x/2}$, are known for their good electrical conductivities and electrocatalytic activities[33,34], and are useful in applications such as the cathode material in high temperature SOFCs or oxygen separation membranes. Lanthanum ferrite, $LaFeO_3$, also belongs to the orthorhombic perovskite group of materials having the space group P*nma*[35]. Like $LaGaO_3$, $LaFeO_3$ also undergoes a phase transition from the orthorhombic (P*nma*) structure to a rhombohedral R-*3c* phase, occurring, for $LaFeO_3$, at 980 °C[35]. The ionic radii of Ga^{3+} and Fe^{3+} are similar, Ga^{3+} = 0.76 Å and Fe^{3+} = 0.79 Å[36], hence the adoption of the same structure is not unexpected. Research on the lanthanum ferrites has centred mainly around their application as a cathode material, and as such, materials such as

$La_{0.6}Sr_{0.4}Co_{0.2}Fe_{0.8}O_{3-(x+y/2)}$ have been examined[37]. However, substitution of Fe^{3+} for Ga^{3+} in $La_{0.9}Sr_{0.1}GaO_3$ has also been studied[24]. It was found that the structure of LSGM was very tolerant to the incorporation of foreign cations and a large number of cations could be used to partially substitute for either La or Ga. However, research has shown that the incorporation of some cations (i.e. Fe^{3+} or Cr^{3+}) cause the evolution of secondary phases, most being Sr-rich and the presence of these phases can cause an increase in *p*-type conductivity[24].

1.3.3.1 Synthesis of the ABO_3 Structure where B = Fe

Most syntheses of ferrite based materials is based on the solid state mixing technique, measuring and mixing the oxides at the required stoichiometry, then calcination and sintering. However, co-precipitation[13] and other techniques[14,15] have been shown to give finer particle sizes and therefore lead to greater densification of the material.

Waller et al.[37] found that citrate and glycine complexation methods, combined with a low temperature calcination, led to the formation of a cubic perovskite (from rhombohedral) with a high degree of cation deficiency on the A-site. Heating the A-site deficient perovskite in the presence of Sr(II), at temperatures in excess of 950 °C, led to the incorporation of Sr into the perovskite lattice, causing a change in the symmetry from cubic to rhombohedral, and a decrease in the unit cell volume.

Table 1.3 Structure for various ferrite based perovskites

Compound	Structure	Space Group	Preparation	Reference
$LaFeO_3$	Orthorhombic		Solid state reaction 950 °C/12h calcine, 1250 °C/ 10h, sinter	38
$LaFeO_3$	Orthorhombic		Citric acid, 1000 °C/8h calcine	39
$LaFeO_3$	Orthorhombic	*Pbnm*	Single crystal	35
$LaFeO_3$	Orthorhombic		Thermal decomposition	40
$LaFeO_3$	Orthorhombic		Solid state mixing, calcine 1000 °C, 1400 °C sinter	41
$LaFeO_3$	Orthorhombic/ Rhombohedral transition	987 °C		22
$LaFe_yCo_{1-y}O_3$	Orthorhombic (y=0.6-1.0)		Explosion method	42

$LaFe_yMn_{1-y}O_3$	Orthorhombic (y=0.3-1.0)		Explosion method, decomp 600 °C/1h, calcine 950 °C/6h	42
$La_{0.6}Sr_{0.4}Fe_{0.8}Cr_{0.2}O_{3-\delta}$	Orthorhombic		Solid state mixing,	43
$La_{0.6}Sr_{0.4}Fe_{0.8}Mn_{0.2}O_{3-\delta}$	Rhombohedral		Solid state mixing	43
$La_{0.6}Sr_{0.4}Fe_{0.8}Co_{0.2}O_{3-\delta}$	Pseudocubic		Solid state mixing	43
$La_{0.6}Sr_{0.4}Fe_{0.8}Ni_{0.2}O_{3-\delta}$	Pseudocubic		Solid state mixing	43
$(La_{0.6}Sr_{0.4})_{0.9}Fe_{0.8}Cr_{0.2}O_{3-\delta}$	Pseudocubic		Solid state mixing	43
$(La_{0.6}Sr_{0.4})_{0.9}Fe_{0.8}Mn_{0.2}O_{3-\delta}$	Pseudocubic		Solid state mixing	43
$(La_{0.6}Sr_{0.4})_{0.9}Fe_{0.8}Co_{0.2}O_{3-\delta}$	Pseudocubic		Solid state mixing	43
$(La_{0.6}Sr_{0.4})_{0.9}Fe_{0.8}Ni_{0.2}O_{3-\delta}$	Pseudocubic		Solid state mixing	43
$La_{0.6}Sr_xCo_{0.2}Fe_{0.8}O_{3-\delta}$	For x=0.4-0.2, Rhombohedral		Pechini method, calcine 1000 °C	37
$La_{0.6}Sr_xCo_{0.2}Fe_{0.8}O_{3-\delta}$	For x=0.15-0.1, Cubic		Pechini method, calcine 1000 °C	37
$LaCr_{0.5}Fe_{0.5}O_3$	Orthorhombic		Solid state mixing, calcine 1000 °C, 1400 °C sinter	41
$LaCr_{0.25}Fe_{0.75}O_3$	Orthorhombic		Solid state mixing, calcine 1000 °C, 1400 °C sinter	41
$PrFeO_3$	Orthorhombic		Solid state reaction 950 °C/ 12h calcine, 1250 °C/10h, sinter	38
$PrFeO_3$	Orthorhombic	*Pbnm*	Single crystal	35
$GdFeO_3$	Orthorhombic	*Pbnm*	Single crystal	35
$GdFeO_3$	Orthorhombic		Solid state reaction 950 °C/ 12h calcine, 1250 °C/10h, sinter	38
$GdFeO_3$	Orthorhombic	*Pbnm* (no. 62)	Coprecipitation & urea evaporation	44
$NdFeO_3$	Orthorhombic	*Pbnm*	Single crystal	35
$NdFeO_3$	Orthorhombic	*Pbnm* (no. 62)	Coprecipitation & urea evaporation	44
$NdFeO_3$	Orthorhombic		Solid state reaction 950 °C/ 12h calcine, 1250 °C /10h, sinter	38
$TbFeO_3$	Orthorhombic		Solid state reaction 950 °C/ 12h calcine, 1250 °C/10h, sinter	38
$TbFeO_3$	Orthorhombic	*Pnma*	Crystal prep - flux method	45
$DyFeO_3$	Orthorhombic	*Pnma*	Crystal prep - flux method	45
$HoFeO_3$	Orthorhombic	*Pnma*	Crystal prep - flux method	45
$HoFeO_3$	Orthorhombic		Solid state reaction 950 °C/ 12h calcine, 1250 °C/10h, sinter	38
$ErFeO_3$	Orthorhombic	*Pnma*	Crystal prep - flux method	45
$ErFeO_3$	Orthorhombic		Solid state reaction 950 °C/ 12h calcine, 1250 °C/10h, sinter	38
$TmFeO_3$	Orthorhombic	*Pnma*	Xtals prep by flux method	45
$YFeO_3$	Orthorhombic	*Pbnm*	Single crystal	35
$YFeO_3$	Orthorhombic		Solid state reaction 950 °C/ 12h calcine, 1250 °C/10h, sinter	38
$YbFeO_3$	Orthorhombic		Solid state reaction 950 °C/ 12h calcine, 1250 °C/10h, sinter	38
$EuFeO_3$	Orthorhombic	*Pbnm*	Single crystal	35

$Eu_3Fe_5O_{12}$		*Ia3d* (230)	Coprecipitation	46
$EuFeO_3$	Orthorhombic	*Pbnm* (no. 62)	Coprecipitation	46
$SmFeO_3$	Orthorhombic	*Pbnm*	Single crystal	35
$SmFeO_3$	Orthorhombic	*Pbnm* (no. 62)	Coprecipitation & urea evaporation	44

1.3.4 ABO_3 Structure where B = Cr

Lanthanum chromite, $LaCrO_3$, also belongs to the orthorhombic perovskite group of materials. Calcium-doped lanthanum chromite $(La,Ca)CrO_3$ has been considered as an interconnect material for the solid oxide fuel cell[47]. It has a high melting point (> 2400 °C) and an electrical conductivity at 1000 °C ranging from 1 to 60 Scm^{-1} in an oxygen partial pressure range of $1.013x10^{-15}$ to $1.013x10^{5}$ Pa[48] respectively, and its thermal expansion coefficient can be matched with yttria-stabilised zirconia[49]. Lanthanum chromite has an orthorhombic to rhombohedral phase-transition at approximately 255 °C[50], and the rhombohedral phase is stable at higher temperatures. These features make $LaCrO_3$ similar to $LaGaO_3$ and $LaFeO_3$ and the ionic radii of Ga^{3+} and Cr^{3+} are similar, Ga^{3+} = 0.76 Å and Cr^{3+} = 0.755 Å[36].

1.3.4.1 Synthesis of the ABO_3 Structure where B = Cr

Most syntheses of chromite based materials is based on the solid state mixing technique[38], measuring and mixing the oxides at the required stoichiometry, then calcination and sintering. However, firing of the citrate and citrate-nitrate gels has also been a successful method[50] in fabricating a single phase perovskite material.

Table 1.4 Structure for various chromite based perovskites

Compound	Structure	Space Group	Preparation	Reference
$LaCrO_3$	Orthorhombic		Solid state reaction 950 °C /12h calcine, 1250 °C/10h, sinter	38
$LaCrO_3$	Orthorhombic	RT	firing of citrate gels	50
$LaCrO_3$	Rhombohedral	260 °C transition	firing of citrate gels	50
$LaCrO_3$	Ideal cubic	1647 °C transition	firing of citrate gels	50
$LaCrO_3$	Melting point	2227 °C	firing of citrate gels	50
$LaCrO_3$	Orthorhombic		Liquid mix method	51

			1450 °C/2h sinter	
$LaCrO_3$	Rhombohedral at 271 °C	R*3-m* most likely	Spray drying from nitrates at 1300 °C, 1450 °C/2h sinter	52
$LaCrO_3$	Orthorhombic		Citrate-nitrate gel, 850 °C pre-calcine 1400 °C/10h sinter	53
$LaCrO_3$	Orthorhombic - Rhombohedral transition	260 °C	Single crystal	22
$LaCrO_3$	Rhombohedral-cubic transition	+1600 °C	Single crystal	22
$LaCrO_3$	Orthorhombic		Solid state mixing, 1000 °C calcine, 1400 °C sinter.	41
$LaCrO_3$	Orthorhombic	Achieved as low as 800 °C	Hydrazine method	54
$LaCo_{1-y}Cr_yO_3$	Rhombohedral for y>0.84		firing of citrate gels	50
$LaCr_{0.75}Fe_{0.25}O_3$	Orthorhombic		Solid state mixing, 1000 °C calcine, 1400 °C sinter.	41
$LaCr_{0.75}Mn_{0.25}O_3$	Orthorhombic		Solid state mixing, 1000 °C calcine, 1400 °C sinter.	41
$LaCr_{0.5}Mn_{0.5}O_3$	Orthorhombic		Solid state mixing, 1000 °C calcine, 1400 °C sinter.	41
$La(Cr_{1-x}Mn_x)O_3$	X=0, Orthorhombic-Rhombohedral, 256 °C		Pechini method, 850 °C/8h calcine, 1400 °C/16h sinter	55
$La(Cr_{1-x}Mn_x)O_3$	X=0.25, Orthorhombic-Rhombohedral, 305 °C		Pechini method, 850 °C/8h calcine, 1400 °C/16h sinter	55
$SmCrO_3$	Orthorhombic		Solid state reaction 950 °C /12h calcine, 1250 °C/10h, sinter	38
$GdCrO_3$	Orthorhombic		Solid state reaction 950 °C /12h calcine, 1250 °C/10h, sinter	38
$DyCrO_3$	Orthorhombic		Solid state reaction 950 °C /12h calcine, 1250 °C/10h, sinter	38
$HoCrO_3$	Orthorhombic		Solid state reaction 950 °C /12h calcine, 1250 °C/10h, sinter	38
$YbCrO_3$	Orthorhombic		Solid state reaction 950 °C /12h calcine, 1250 °C/10h, sinter	38
$LuCrO_3$	Orthorhombic		Solid state reaction 950 °C /12h calcine, 1250 °C/10h, sinter	38
$YCrO_3$	Orthorhombic		Solid state reaction 950 °C /12h calcine, 1250 °C/10h, sinter	38
$YCrO_3$	Orthorhombic	P*bnm*	Single crystal	35

1.3.5 ABO_3 Structure where B = Mn

Lanthanum manganite, $LaMnO_3$, also belongs to the orthorhombic perovskite group of materials, having the space group P*nma*. $La_{1-x}Sr_xMnO_3$ (LSM) has been widely applied as the cathode material for solid oxide fuel cells[56]. Its structure is dependent on the concentration of x in the system and varies from orthorhombic P*nma* ($LaMnO_3$), to rhombohedral R*3-c* ($La_{0.7}Sr_{0.3}MnO_3$) and monoclinic ($La_{0.84}Sr_{0.16}MnO_3$)[57].

LSM ($La_{0.83}Sr_{0.17}MnO_3$) has an orthorhombic (P*nma*) to rhombohedral (R*3-c*) phase-transition point at approximately 285 °C[57], where the rhombohedral phase is stable at higher temperatures. This is similar to $LaGaO_3$ and $LaFeO_3$ and the ionic radii of Ga^{3+} and Mn^{3+} are similar, Ga^{3+} = 0.76 Å and Mn^{3+} = 0.785 Å[36].

1.3.5.1 Synthesis of the ABO_3 Structure where B = Mn

Like $LaCrO_3$ based materials, the synthesis of manganite based materials is most commonly undertaken by the solid state mixing technique, measuring and mixing the oxides at the required stoichiometry, then calcination and sintering[41].

Table 1.5 Structure for various manganite based perovskites

Compound	Structure	Space Group	Preparation	Reference
$LaMnO_3$	Orthorhombic	P*nma*	Drip pyrolysis, calcine 1100-1300 °C/4-12h	56
$LaMnO_3$	Orthorhombic	MnO_6 coord.	Citrate gel	38
$LaMnO_3$	Hexagonal		Solid state mixing, 1000 °C calcine, 1400 °C sinter.	41
$La_{1-x}Sr_xMnO_3$	X=0, 0.1, 0.2, Orthorhombic		Single crystal	58
$La_{0.7}Sr_{0.3}MnO_3$	Rhombohedral		Single crystal	58
$La_{0.7}Sr_{0.3}MnO_3$		R*3-c*	Citrate gel, sinter 1200 °C	59
$La_{1-x}Sr_xMnO_3$	X=0.17, 290 °C, Rhombohedral	R*3-c* (no 167)	Floating zone method, sinter 1350 °C/24h	57
$La_{1-x}Sr_xMnO_3$	X=0.17, 280 °C, Orthorhombic	P*nma* (no 62)	Floating zone method, sinter 1350 °C/24h	57
$La_{0.84}Sr_{0.16}MnO_3$	Monoclinic		Solid state mixing, 1250 °C/8h calcine,	28

			1470 °C/36h sinter	
$La_{0.7}Ca_{0.3}MnO_3$	Pseudocubic Perovskite		Solid state	60
$LaMn_yCo_{1-y}O_{3-\delta}$	Hexagonal (y=0.7-1.0)		Explosion method calcine 950 °C/6h	42
$LaFe_yMn_{1-y}O_{3-\delta}$	Hexagonal (y=0-0.3)		Explosion method calcine 950 °C/6h	42
$La(Co_{0.2}Mn_{0.8})O_3$	Orthorhombic	*Pbnm*	Solid state mixing 1300 °C/16h in N_2	61
$LaCr_{0.25}Mn_{0.75}O_3$	Hexagonal		Solid state mixing, 1000 °C calcine, 1400 °C sinter.	41
$YMnO_3$	Orthorhombic	*Pnma*	High temp. anneal	62
$YMnO_3$	Hexagonal	MnO_5 coord.	Citrate gel	38
$PrMnO_3$	Orthorhombic	MnO_6 coord.	Citrate gel	38
$NdMnO_3$	Orthorhombic	MnO_6 coord.	Citrate gel	38
$HoMnO_3$	Hexagonal	MnO_5 coord.	Citrate gel	38
$YbMnO_3$	Hexagonal	MnO_5 coord.	Citrate gel	38

1.3.6 ABO_3 Structure where B = Co

Lanthanum Cobaltite materials have applications as the cathode material for solid oxide fuel cells[63]. Lanthanum cobaltite, $LaCoO_3$, while having the perovskite structure, varies slightly from the preceding materials in that it does not have an orthorhombic structure at room temperature. The ionic radii of Ga^{3+} and Co^{3+} are similar, Ga^{3+} = 0.76 Å and Co^{3+} = 0.75 Å[36], Fe^{3+}, Mn^{3+} and Cr^{3+} also have similar ionic radii, but the structure adopted by $LaCoO_3$ is not similar to that of $LaFeO_3$, $LaMnO_3$ or $LaCrO_3$. Ni doped $LaCoO_3$ appears to take on the cubic symmetry at low Ni concentrations and then becomes two phase before transforming to tetragonal symmetry at higher Ni concentrations[56].

1.3.6.1 Synthesis of the ABO_3 Structure where B = Co

Table 1.6 shows that most syntheses of cobaltite based materials is based on liquid citrate method[56], or the firing of stearic acid/sol gel method[63].

Table 1.6 Structure for various cobaltite based perovskites

Compound	Structure	Space Group	Preparation	Reference
$LaCoO_3$			Citric acid method	39
$LaCoO_3$	Hexagonal <500 °C Perovskite-like >500 °C		Stearic acid/sol gel method	63
$LaCoO_3$	Rhombohedral	RT	Multiple firing of citrate gels	50
$LaCoO_3$	Melts	1467 °C	Multiple firing of citrate gels	50
$La_{0.8}Sr_{0.2}CoO_3$			Polyethylene glycol	39
$La_{0.6}Sr_{0.4}CoO_{3-\delta}$	Simple cubic symmetry and no change after anneal in He from 700 °C		Liquid citrate method, 1000-1100 °C/5h calcine, 1160 °C/5h sinter	64
$La_{0.5}Sr_{0.5}CoO_{3-\delta}$	Primitive cubic		Solid state reaction, 1250 °C/8h calcine, 1470 °C/36h sinter	28
$La_{0.6}Sr_{0.4}CoO_{2.80}$	Cubic		Liquid citrate method, 1000 °C/10h calcine, 1250 °C/10h sinter	56
$La_{0.8}Sr_{0.2}CoO_{2.9}$	Cubic		Liquid citrate method, 1000 °C/10h calcine, 1250 °C/10h sinter	56
$La_{0.8}Sr_{0.2}Co_{0.8}Ni_{0.2}O_{2.8}$	Cubic		Liquid citrate method, 1000 °C/10h calcine, 1250 °C/10h sinter	56
$La_{0.6}Sr_{0.4}Co_{0.8}Ni_{0.2}O_{2.7}$	Cubic		Liquid citrate method, 1000 °C/10h calcine, 1250 °C/10h sinter	56
$La_{0.5}Sr_{0.5}Co_{0.8}Ni_{0.2}O_{2.65}$	Cubic		Liquid citrate method	56
$La_{0.4}Sr_{0.6}Co_{0.8}Ni_{0.2}O_{2.6}$	Cubic		Liquid citrate method, 1000 °C/10h calcine, 1250 °C/10h sinter	56
$La_{0.6}Sr_{0.4}Co_{0.6}Ni_{0.4}O_{2.6}$	Cubic & Tetragonal (2 phases observed)		Liquid citrate method, 1000 °C/10h calcine, 1250 °C/10h sinter	56
$La_{0.5}Sr_{0.5}Co_{0.6}Ni_{0.4}O_{2.55}$	Cubic & Tetragonal (2 phases observed)		Liquid citrate method, 1000 °C/10h calcine, 1250 °C/10h sinter	56
$La_{0.4}Sr_{0.6}Co_{0.6}Ni_{0.4}O_{2.5}$	Cubic & Tetragonal (2 phases observed)		Liquid citrate method, 1000 °C/10h calcine, 1250 °C/10h sinter	56
$La_{0.6}Sr_{0.4}Co_{0.4}Ni_{0.6}O_{2.5}$	Tetragonal		Liquid citrate method, 1000 °C/10h calcine, 1250 °C/10h sinter	56

$La_{0.5}Sr_{0.5}Co_{0.4}Ni_{0.6}O_{2.45}$	Tetragonal		Liquid citrate method, 1000 °C/10h calcine, 1250 °C/10h sinter	56
$La_{0.4}Sr_{0.6}Co_{0.4}Ni_{0.6}O_{2.4}$	Tetragonal		Liquid citrate method, 1000 °C/10h calcine, 1250 °C/10h sinter	56
$LaMn_yCo_{1-y}O_{3-\delta}$	Rhombohedral (y=0-0.5)		Explosion method	42
$LaFe_yCo_{1-y}O_{3-\delta}$	Rhombohedral (0-0.6)		Explosion method	42
$LaCo_{1-y}Cr_yO_3$	Rhombohedral for y<0.76		Multiple firing of citrate gels	50
$SrCo_{0.8}Cr_{0.2}O_{3-\delta}$	Cubic after quenching in air from 1100 °C		Liquid citrate method, 1000-1100 °C/5h calcine, 1160 °C/5h sinter	64
$SrCo_{0.8}Fe_{0.2}O_{3-\delta}$	Cubic perovskite	If slow cooled from 700 °C in helium, Orthorhombic	Liquid citrate method, 1000-1100 °C/5h calcine, 1160 °C/5h sinter	64
$SrCoO_{3-\delta}$	Transform from Hexagonal to Perovskite at 900 °C	Depends on annealing etc though	Liquid citrate method, 1000-1100 °C/5h calcine, 1160 °C/5h sinter	64
$SrCo_{0.8}Cu_{0.2}O_{3-\delta}$	Cubic after quenching in air from 1100 °C		Liquid citrate method, 1000-1100 °C/5h calcine, 1160 °C/5h sinter	64

1.3.7 ABO_3 Structure where B = Gd

$LaGdO_3$ is a mixed rare earth oxide with a B-type monoclinic structure, having a space group C2/*m*[65]. The phase remains stable to temperatures above 1800 °C[66]. Although $LaGdO_3$ is of the ABO_3 structure, the size of Gd^{3+} (1.078 Å) in relation to Ga^{3+} (0.76 Å) or Fe^{3+} (0.79 Å)[36] makes the overall structure of the material completely different to that of $LaGaO_3$, where Ga^{3+} is of a much smaller size than La^{3+}. Gd^{3+} is closer to the size of La^{3+} (1.36 Å)[36].

1.3.7.1 Synthesis of the ABO_3 Structure where B = Gd

The synthesis of $LaGdO_3$ has only been undertaken using the solid state mixing technique, measuring and mixing the oxides at the required stoichiometry, then calcination and sintering at a high pressure[67-69].

Table 1.7 Structure for various gadolinium based perovskites

Compound	Structure	Space Group	Preparation	Reference
$GdFeO_3$	Orthorhombic	*Pnma* (No. 62)	coprecipitation	46
$LaGdO_3$	Monoclinic	*C2/m*	Solid state mixing and high pressure 1350 °C sinter	67-69

1.3.8 Other Perovskite Materials

There are a vast number of both A and B site variations in the ABO_3 type perovskite structure. Listed in Table 1.8 is a cross-section of a number of such materials. It should be noted that a large number of these materials adopt the orthorhombic structure, with the space group, *Pnma*. The size difference between the A and B cations is what appears to influence the final structure of the material[2], as shown in sections 1.3.2 to 1.3.6. $LaGaO_3$, $LaFeO_3$, $LaCrO_3$ and $LaMnO_3$ are all of comparable sizes[36], and all adopt the same structure, however, $LaCoO_3$ (whose ionic radii is similar to Ga, Fe, Cr and Mn) differs. The ratio of ionic radii is not always the predominant factor in deciding what structure an ABO_3 type material will adopt, however, it does influence the choice of A and B cations in attempting to fabricate a material of a certain structure.

Table 1.8 Structure for various other perovskites

Compound	Structure	Space Group	Preparation	Reference
$MgSiO_3$	Orthorhombic (high pressure >25GPa	*Pbnm*	Multiple anvil press @25Gpa 1700 °C	70
$YBa_2Cu_3O_{7-\delta}$	Orthorhombic (OI)		Single crystal	71
$YBa_2Cu_3O_{6.5}$	Orthorhombic (OII)		Single crystal	71
$YBa_3Cu_3O_6$	Tetragonal (T)		Single crystal	71
$PbMg_{1/3}Nb_{2/3}O_3$		*Pm3m* to *Fm3m* at high temp, T>627 °C		72
$PbMg_{1/3}Ta_{2/3}O_3$		*Pm3m*		72
$PbSc_{1/2}Ta_{1/2}O_3$		*Pm3m*		72
$CeLuO_3$	Orthorhombic		In $Ar+H_2$ at 1400 °C	73
$PrLuO_3$	Orthorhombic		Solid phase reaction in air	73
$NdLuO_3$	Orthorhombic		Solid phase reaction in air	73
$LaYO_3$	Orthorhombic	*Pnma*	Co-crystallisation of nitric acid solution or	74

			by coprecipitation	
$LaErO_3$	Orthorhombic	*Pnma*	Co-crystallisation of nitric acid solution or by coprecipitation	74
$LaTmO_3$	Orthorhombic	*Pnma*	Co-crystallisation of nitric acid solution or by coprecipitation	74
$LaYbO_3$	Orthorhombic	*Pnma*	Co-crystallisation of nitric acid solution or by coprecipitation	74
$LaLuO_3$	Orthorhombic	*Pnma*	Co-crystallisation of nitric acid solution or by coprecipitation	74
$BaCeO_3$	Orthorhombic	*Pnma*	Single crystal, zone melting	75
$BaCeO_3$	Cubic <900 °C			76
$CaTiO_3$	Orthorhombic			77,78
$PbTiO_3$	Tetragonal			77,78
$SrTiO_3$	Cubic	*Pm3m*		77,78
$BaTiO_3$	Tetragonal			78
$CaZrO_3$	Orthorhombic			78
$PbZrO_3$	Tetragonal			78
$SrZrO_3$	Cubic			78
$BaZrO_3$	Cubic			78
$YAlO_3$		*Pbnm*	Single crystal	18, 35 - powder XRD
$NdAlO_3$	Rhombohedral	*R3-c*		79
$LaNiO_3$	Rhombohedral at room temp	*R3-m*	Spray drying of nitrates	52
$LaNiO_3$	Cubic at 1020 °C	*Pm3-m*	Spray drying of nitrates	52
$YBa_2Cu_3O_{7-\delta}$	RT Orthorhombic, transition to Tetragonal		Single crystal Czochralski grown	7
$NdBa_2Cu_3O_{7-\delta}$	RT Orthorhombic, transition to Tetragonal		Single crystal Czochralski grown	7
$GdAlO_3$	Orthorhombic	*Pbnm*	Single crystal	80
$EuAlO_3$	Orthorhombic	*Pbnm*	Single crystal	80
$SmAlO_3$	Orthorhombic	*Pbnm*	Single crystal	80
$NdAlO_3$	Rhombohedral	*R3-m*	Single crystal	80
$PrAlO_3$	Rhombohedral	*R3-m*	Single crystal	80
$LaAlO_3$	Rhombohedral	*R3-m* (simple cubic above 435 °C)	Single crystal	80
$PrAlO_3$	Rhombohedral – Cubic	Transition at 1370 °C		22
$NdAlO_3$	Rhombohedral – Cubic	Transition at 1747 °C		22
$LaAlO_3$	Rhombohedral – Cubic	Transition at 527 °C		22
$SmAlO_3$	Orthorhombic - Rhombohedral	Transition at 802 °C		22
$La_{0.95}Sr_{0.05}AlO_{3-\delta}$	Cubic		Solid state mixing of oxides and carbonates	25
$Y_{0.95}Sr_{0.05}AlO_{3-\delta}$	Orthorhombic dominant phase with Cubic Garnet		Solid state mixing of oxides and carbonates	25
$La_{0.9}Sr_{0.1}AlO_{3-\delta}$	Hexagonal	*R3-c*	Solid state reaction	26

	(Rhombohedral)			
$La_{0.9}Sr_{0.1}MO_{3-\delta}$ (M=Sc, In, Lu)	Orthorhombic	P*bnm*	Solid state reaction	26

1.4 Raman Spectroscopy

Raman spectroscopy has been used extensively to study the structure of inorganic materials[21], however, very few comprehensive works exist in the literature. The number of bands observed in a spectrum is dependent on the crystal symmetry of the compound being studied. The bands are related to the modes of vibration of the atoms in the structure, and can be calculated as an irreducible representation, in which the number and type of mode and the activity in either Raman, infrared or both can be determined[81]. This forms the basis for characterisation of materials using vibrational spectroscopy. Table 1.9 shows the irreducible representations for various perovskite structures, namely the ideal cubic structure, orthorhombic, rhombohedral and tetragonal. The number of modes active in Raman, infrared and coincident vary depending on the structural type, and phase changes of the perovskite material and can be determined from the number of bands and hence modes observed with changes in dopant concentration and temperature[76]. It can be seen from Table 1.9 that the number of predicted modes increases with decrease in symmetry or space group of the perovskite, in the order of cubic to rhombohedral to tetragonal to orthorhombic.

A further method of characterising the Raman and infrared spectra is the comparison of the spectral profile and relative band positions of a spectrum of a fully characterised material[82]. Tables 1.10, 1.11 and 1.12 show the Raman band positions (cm^{-1}) of $LaGaO_3$, $LaCrO_3$ and $LaFeO_3$ respectively, at various temperatures. All three of these materials are orthorhombic at room temperature. Table 1.13 lists mode assignments of the Raman spectra of the low temperature orthorhombic phase for $SmAlO_3$ (both observed and calculated), $LaGaO_3$, $LaFeO_3$ and $LaCrO_3$. Table 1.14 lists mode assignments to Raman band position (cm^{-1}) of the $LaGaO_3$ high temperature phase to $LaCoO_3$ (RT), $LaCrO_3$ (300 °C), $LaMnO_3$ and doped $LaCoO_3$ (RT).

Table 1.9 Irreducible representations for perovskite structures and base oxides.

Structure ABO_3	**Space Group**	Z	Γ_R	N_R	Γ_{IR}	N_{IR}	N_I	N_C	Γ_{ac}
Rhombohedral A-La_2O_3	P-*3ml* D_{3d}^3(164)	1	$2A_{1g}+2E_g$	4	$2A_{2u}+2E_u$	8	None	None	$2A_u+E_u$
Rhombohedral α-Cr_2O_3	R-*3c* D_{3d}^6(167)	6	$2A_{1g}+5E_g$	7	$2A_{2u}+2E_u$	8	None	None	$2A_u+E_u$
Rhombohedral α-Fe_2O_3	R-*3c* D_{3d}^6(167)	6	$2A_{1g}+5E_g$	7	$2A_{2u}+2E_u$	8	None	None	$2A_u+E_u$
Co_3O_4	O_h^7	14	$A_{1g}+E_g+3F_{2g}$	5	$4F_{tu}$	4	$F_{1g}+2A_{2u}+2E_u+2F_{2u}$	None	F_{1u}
Mn_3O_4	O_h^7	14	$A_{1g}+E_g+3F_{2g}$	5	$4F_{tu}$	4	$F_{1g}+2A_{2u}+2E_u+2F_{2u}$	None	F_{1u}
Ga_2O_3	C_{2h}^3		$10A_g+5B_g$	15	$4A_u+8B_u$	12	?	None	F_{1u}
Cubic (Ideal) e.g. $SrTiO_3$	Pm3m O_h^1(221)	1	4F1u	4	3F1u	3	F2u	3	F1u
Orthorhombic e.g. $GdFeO_3$	P*nma* D_{2h}^{16}(62)	4	$7A_g+7B_{ig}+5B_{2g}+5B_{3g}$	24	$7B_{1u}+9B_{2u}+9B_{3u}$	25	$8A_u$	None	$B_{1u}+B_{2u}+B_{3u}$
Rhombohedral e.g. HT-$LaGaO_3$	R-*3c* D_{3d}^6(167)	6	A_g+4E_g	5	$3A_{2u}+5E_u$	8	$3A_{2g}+2A_{1u}$	None	$A_{2u}+E_u$

Key: Γ_R is the Raman modes, Γ_{IR} is the infrared modes and Γ_{ac} is the acoustic modes, R: Raman active, ir: infrared active, I: inactive, N_R: number of Raman active modes, N_{ir}: number of infrared active modes, N_i: number of inactive modes, N_c: number of coincident modes, Z: number of formula units in the unit cell.

Table 1.10. Raman band positions (cm^{-1}) of $LaGaO_3$ at various temperatures

-196 °C	21 °C	100 °C	140 °C	145 °C	150 °C	250 °C	500 °C
66	55	55	54	54	54	55	55
	92	86	81	80			
108	101	103	102	102	102		
126	117	118	116	116	116		
141	137						
146	147	149	147	146	148		
152							
179	173	171	169	166	166	163	159
245							
264	255	254	254	257	258	251	232
284	277	277	275				
331							
340	335	334	335				
363	357	358	358				
415	404	409	400				
	417						
437	433	435	435	435			
453	451	451	450	450	448	448	444
	584						
	708						

Table 1.11 Raman band positions (cm^{-1}) of $LaCrO_3$ at various temperatures

-196 °C	20 °C	100 °C	200 °C	255 °C	260 °C	265 °C	300 °C
437	441		434	433	433	434	434
282	279	308					
262	252		258	224	238	252	248
180	174	176	168	162	162	162	161
153	150	149	148				
131			140	141	140		
114	103			115	115		
71					58	59	58

Table 1.12 Mode assignment of Raman band positions of orthorhombic $LaFeO_3$ phase

Mode	$SmAlO_3$ Band positions at RT		$LaGaO_3$ Band Positions At 21 °C [6]	$LaFeO_3$ Band Positions at 21 °C [7]	$TbFeO_3$ [9] At RT	$DyFeO_3$ [9] At RT	$HoFeO_3$ [9] At RT	$ErFeO_3$ [9] At RT	$TmFeO_3$ [9] At RT
	Obs. [8]	Calc. [8]							
								9255, 1300 2p	
					521, 641	649	660	645 im	649
B_{3g}	~530	528	451	429	480 A_g	489	495	505	506
A_g	522	527	433	413	479 B_{1g}	494	495	505	506
B_{1g}		528			426 B_{3g}	424	425,475	434	433, 681
B_{2g}	508	512	417		418B_{2g}	425	430	434, 481	429
B_{2g}		507			414 B_{1g}	412			429
B_{1g}		508							
B_{3g}	480	484	404		406 Ag	409	425	424, 434	434
B_{2g}	480	476							
A_g		482							364 B_{2g}
B_{1g}		448			354 B_{3g}			365	364
B_{1g}	408	389	357		329A_g	332	340	345	346
B_{2g}	390	390	331*		329 B_{1g}	339	340	322	346
B_{3g}	392	390	335		273 A_g	270	270	273	273
A_g	345	351	277	289		260 B_{2g}	210		
A_g	286	271	255	261	249 B_{3g}	260		264	263
B_{3g}	198	212	173	227	159 B_{3g}		205		139
A_g	200	191	147	176	157 A_g	160	159	163	160
B_{1g}	170	188	137	150	139 B_{1g}	138		112, 163	139
B_{2g}	143	106	117	Ca. 140 sh	140 $_{Ag}$	140	139	140	140
B_{3g}	136	126	101						
B_{1g}	110	96	92	102	109$_{Ag}$	110	109	112	110
A_g		90				89B_{2g}			
A_g	78	85	55						
B_{1g}		84							

*observed at –196 °C. sh = shoulder, s = strong

Table 1.13 Mode assignment of the Raman spectra of low temperature orthorhombic phase.

Mode	$SmAlO_3$		$LaGaO_3$	$LaFeO_3$	$LaCrO_3$	
	Band Positions at RT		Band Positions	Band Positions	Band positions at	
	Observed	calculated	at 21 °C	at 21 °C	-196 °C	20 °C
B_{3g}	~530	528	451	429		
A_g	522	527	433	413		
B_{1g}		528				
B_{2g}/B_{2g}	508	512/507	417		441	437
B_{1g}		508				
B_{3g}	480	484	404			
B_{2g}	480	476				
A_g		482				
B_{1g}		448				
B_{1g}	408	389	357			
B_{2g}	390	390	331*			
B_{3g}	392	390	335			
A_g	345	351	277	289	279	282
A_g	286	271	255	261	252	262
B_{3g}	198	212	173	227	174	180
A_g	200	191	147	176	150	153
B_{1g}	170	188	137	150	-	131
B_{2g}	143	106	117		103	114
B_{3g}	136	126	101			
B_{1g}	110	96	92			
A_g		90				
A_g	78	85	55	102	-	71
B_{1g}		84				

* observed at –196 °C

Table 1.14 Mode assignment to Raman band positions (cm^{-1}) of $LaGaO_3$ high temperature phase

Mode	$NdAlO_3$	HT-$LaGaO_3$ (500 °C)	HT-$LaCrO_3$ (300 °C)	$LaMnO_3$	$LaCoO_3$ *at RT	$La_{0.8}Sr_{0.2}CoO_3$ at RT	$La_{0.8}Sr_{0.2}Fe_{0.4}Co_{0.4}O_3$ at RT
						910	
				Ca. 610	810	812	810
				Ca. 500	700	630	700
E_g	511	444	434	Ca. 320	570		
E_g	511	444	434	Ca. 220	420	500	405
A_{1g}	243	232	258		305	305	305
E_g	166	159	161		130		
E_g	55	55	58				

* nanocrystalline sample

1.5 Electrical studies of Doped $LaGaO_3$

1.5.1 Introduction

In 1994 Ishihara et al.[1] and Feng and Goodenough[6] published papers reporting a new perovskite oxide ion conductor based on $LaGaO_3$. Both papers reported that doping of the material on the A site with Sr, and the B site with Mg, gave an oxide ion conductor with conductivity (σ) comparable to that of yttria stabilised zirconia (YSZ), if slightly higher [at 800 °C, 9% YSZ has $\sigma = 3.6 \times 10^{-2}$ Scm^{-1} and for LSGM, $\sigma = 10.4 \times 10^{-2}$ Scm^{-1}[6]].

1.5.2 Conductivity

The conductivity of a material is related to, and dependent upon, both intrinsic and extrinsic defects in a material. Intrinsic defects are defects inherent in the material and can occur naturally, and include point and line defects. Extrinsic defects are those introduced into the material by way of doping.

In an oxide ion conductor, oxygen reacts with the vacancies, as shown in equations 1.1 and 1.2, to form oxide ions that can then migrate across the electrolyte by diffusion[83].

$$\frac{1}{2}O_2 + V_i \xleftrightarrow{K1.2} O_i'' + 2h^{\bullet} \qquad (1.1)$$

$$\frac{1}{2}O_2 + 2e' + V_o^{\bullet\bullet} \xleftrightarrow{K1.1} O_o^x \qquad (1.2)$$

The equilibrium reactions for equations 1.1 and 1.2 are shown below, where $K_{1.1}$ is the equilibrium constant for reaction 1.1 and $K_{1.2}$ is the equilibrium constant for reaction 1.2.

$$K_{1.1} = \frac{(P_{O_2})^{-\frac{1}{2}}}{[V_o^{\bullet\bullet}][e']^2} \qquad (1.3)$$

$$K_{1.2} = (P_{O_2})^{-\frac{1}{2}}[h^{\bullet}]^2[O_i''] \qquad (1.4)$$

In order to maintain electroneutrality,

$$2V_o^{\bullet\bullet} + 2O_i'' = 0 \qquad (1.5)$$

and

$$[h^{\bullet}] + [e'] = 0 \qquad (1.6)$$

In a material such as LSGM, doping of both the A and B sites of the material is expected to cause an increase in the number of vacancies, hence increasing the conductivity accordingly.

At intermediate P_{O_2} concentration, it has been shown that $[O_i''] \approx [V_o^{\bullet\bullet}]$ and that conductivity is independent of P_{O_2}. At high P_{O_2} concentrations the concentration of

electrons is greater than the concentration of electron holes and therefore equation 1.7 holds.

$$[e'] \propto P_{O_2}^{-\frac{1}{4}} \qquad (1.7)$$

At low P_{O_2} concentrations the concentration of electron holes is greater than the concentration of electrons and equation 1.8 holds.

$$[h^{\bullet}] \propto P_{O_2}^{\frac{1}{4}} \qquad (1.8)$$

If the conductivity does not change as a function of P_{O_2}, then the majority charge carrier is an oxide ion, and the material is considered to conduct ionically.

Research to date has shown that the electrical conductivity of $LaGaO_3$ depends strongly on the alkaline earth cations added for the La site and increases in the order Sr>Ba>Ca[1] as shown in Figure 1.5.

Ishihara et al.[1] found that the electrical conductivity of $La_{1-x}Sr_xGaO_{3-\delta}$ increased with an increase in the amount of Sr additive and attained a maximum at $x = 0$. Since the number of oxide vacancies increases with an increase in the amount of Sr^{2+} dopant, larger numbers of oxide vacancies are theoretically obtained, and as a result, higher oxide ion conductivity can be achieved. However, impure crystal phases such as $SrGaO_3$ and La_4SrO_7 were detected above $x = 0.1$ in $La_{1-x}Sr_xGaO_3$ by X-ray diffraction analysis[1]. Therefore, they concluded that the limit of solid solution of Sr^{2+} existed at around $x = 0.1$. The formation of secondary impure phases decreased the oxide ionic conductivity of specimens because the ionic conductivity of secondary phases such as $SrGaO_3$ or La_4SrO_7 was low[27]. Therefore, Ishihara et al.[1] concluded that the optimum amount of Sr addition for the La site was at $x = 0.1$ for optimising the oxide ionic conductivity of $LaGaO_3$.

Ishihara et al.[1] also examined the effects of additives on the Ga site for $La_{0.9}Sr_{0.1}GaO_3$ on the electrical conductivity. The results showed that Mg^{2+} had the greatest effect on increasing electrical conductivity among the dopants examined (Mg, Al and In)[1]. The ionic radius of Mg^{2+} is 0.86 Å, which is larger than that of Ga^{3+} (0.76 Å), but smaller than that of La^{3+} (1.36 Å)[36]. Ishihara et al.[1] reported no impure crystal phases detected by X-ray diffraction analysis, and the lattice parameters increased with increasing Mg^{2+} dopant concentration. All of the added Mg^{2+} seemed to have dissolved substitutionally into the Ga^{3+} site of $LaGaO_3$. Although second crystal phases could not be recognised up to x = 0.4, the limit of solid solution of Mg^{2+} for the Ga^{3+} site seemed to show a peak at about x = 0.2, since the lattice parameter was independent of the Mg^{2+} content above x = 0.2. It was therefore concluded that $La_{0.9}Sr_{0.1}Ga_{0.8}Mg_{0.2}O_{2.85}$ was the optimised material for maximum oxide vacancies, and electrical conductivity studies showed agreement with this conclusion, giving conductivity values in the region of 0.3 Scm^{-1} at 950 °C[84].

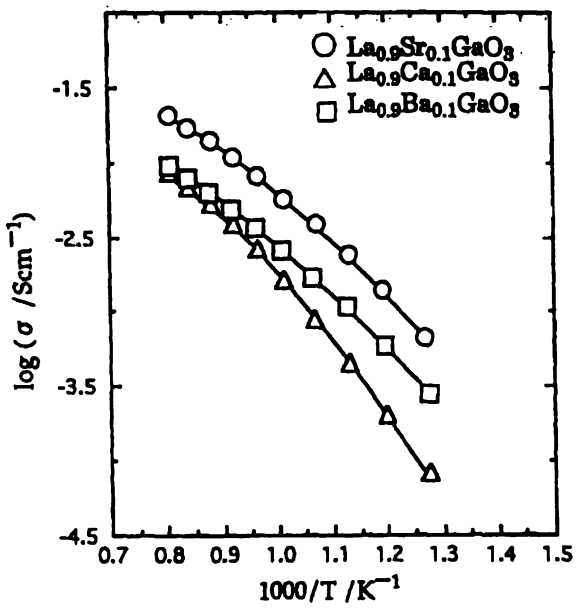

Figure 1.5. Effect of various alkaline earth cations doped for the La sites on the electrical conductivity of $La_{0.9}M_{0.1}GaO_3$ for M = Ca, Sr and Ba, at $P_{O_2} = 10^{-5}$ atm. [Ishihara et al.[1]]

Over the past 5 years considerable research has been undertaken into examining LSGM with varying dopant concentrations of Sr^{2+} and Mg^{2+}, and also in the variation of the A/B ratio in the ABO_3 perovskite structure[8,23,85,86].

It has been anticipated that the LSGM compositions having a deficiency of either A-site or B-site cations (i.e. $A_{1-x}B_{1-y}O_3$) might exhibit higher conductivity that the stoichiometric (i.e., A/B=1) compositions. The introduction of excess cation vacancies into the structure should lead to the formation of additional oxygen vacancies (which are the charge carriers for ionic conduction through the lattice) as the structure adjusts to maintain electrical neutrality. The overall concentration of oxygen vacancies would then be determined by both the acceptor (Sr^{2+} and Mg^{2+}, as in LSGM) concentrations and the cation vacancy concentration (as in $(LS)_{0.95}GM$).

However, from X-ray diffractions studies undertaken by Stevenson et al.[85], it was clear that the LSGM perovskite structure would only tolerate a limited amount of A-site cationic deficiency in its lattice before secondary phases began to form. Therefore, secondary phases were compensating for the cation deficiency, rather than the formation of excess A-site vacancies in the lattice[85].

Huang and Petric[23] investigated the conductivity of LSGM at varying temperatures and reported that $La_{0.8}Sr_{0.2}Ga_{0.9}Mg_{0.1}O_{2.85}$ had the highest conductivity ($\leq 1.3x10^{-1}$ Scm^{-1}) apart from CeO_2-based electrolytes ($\leq 1.3x10^{-1}$ Scm^{-1}) at temperatures of 700 °C and below, while $La_{0.8}Sr_{0.2}Ga_{0.85}Mg_{0.15}O_{2.825}$ had the highest conductivity ($\geq 1.3x10^{-1}$ Scm^{-1}) except for doped-Bi_2O_3 (≤ 1.05 Scm^{-1}) at temperatures above 700 °C[23]. They also concluded that generally, the maximum in conductivity corresponds to the compositions of $La_{1-x}Sr_xGa_{1-y}Mg_yO_{3-(x+y/2)}$ where $x + y = 0.35$.

Huang et al.[86] found that the single phase composition $La_{0.8}Sr_{0.2}Ga_{0.83}Mg_{0.17}O_{2.815}$ exhibited a stable conductivity, σ_{oxide}, of approximately 0.166 and 0.079 Scm^{-1} at 800 °C and 700 °C respectively, and was observed to be an almost pure oxide ion conductor[8] (t_i was very close to 1).

1.5.3 Stability

1.5.3.1 Ionic Transport Number

When the ionic conductivity (σ_i) of a material is quoted, the transport (or transference) number (t_i) is also given. This is described in equation 1.9:

$$t_i = \sigma_i/(\sigma_i + \sigma_e + \sigma_h) \qquad (1.9)$$

where σ_i = the ionic (oxide ion) conductivity, σ_e = *n*-type (electron) conductivity and σ_h = *p*-type (hole) conductivity, as illustrated in Figure 1.6. For an ionic conductor, the value for the transport number is approximately 1. The higher the number, the closer the material is to being a "pure" ionic conductor, i.e. conductivity is predominantly ionic, and the electronic contributions are negligible. The ionic domain describes the range of oxygen partial pressure over which the material retains a t_i of approximately 1. The electrolytic domain boundaries are the oxygen partial pressures at which the ionic conductivity is 100 times the *p*-type conductivity or 100 times the n-type conductivity. The material is said to be exclusively ionic within the electrolytic domain. For LSGM materials, that range is reported to be between the oxygen partial pressures (P_{O_2}) of 0.4 to $1x10^{-20}$ Pa[1].

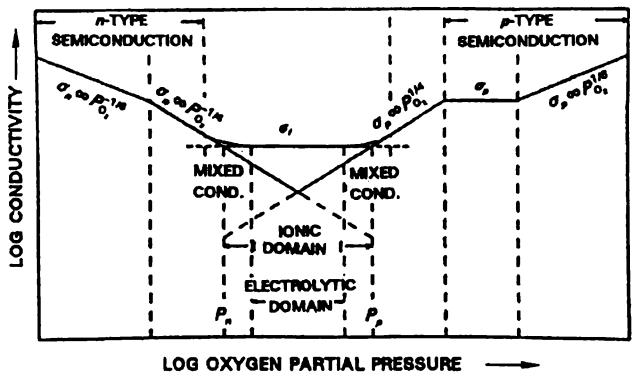

Figure 1.6 The variation of the conductivity as a function of oxygen partial pressure for MO_2 showing the electrolytic and ionic domain boundaries[83] where M = some 4^+ cation.

The lanthanum gallates are predominantly oxygen ion conductors, but not exclusively so. Electrical studies of $La_{0.9}Sr_{0.1}Ga_{1-x}Mg_xO_3$ (where x = 0-0.15) showed that electrical conduction was almost independent of the oxygen partial pressure over the range of $P_{O_2} = 10^{-20}$ to 1 atm. at 950 °C[1]. Feng and Goodenough[6] reported conductivity of approximately 10^{-2} Scm^{-1} at 600 °C with a transport number $t_i = 1$ over the oxygen partial pressure range $1x10^{-20}<P_{O_2}<0.4$ atm. for the material $La_{0.9}Sr_{0.1}Ga_{0.8}Mg_{0.2}O_{2.85}$.

In 1995 Ishihara et al.[10] reported the effects of rare earth cations doped for the La site on the oxide ion conductivity of $LaGaO_3$ based perovskite type oxides. They found that addition of a small amount of rare earth cations for the La site in $LaGaO_3$ was effective in the suppression of hole conduction under high oxygen partial pressure, although the electrical conductivity did decrease slightly. In particular, they found that the perovskite oxide of $(La_{0.9}Nd_{0.1})_{0.8}Sr_{0.2}Ga_{0.8}Mg_{0.2}O_{3-\delta}$ exhibited almost pure oxide ionic conduction over the oxygen partial pressure from 1 to 10^{-21} atm., and the electrical conductivity attained the value of 0.5 Scm^{-1} at 950 °C[10].

Oxygen surface exchange and diffusion studies have also been undertaken on LSGM[87]. Results showed that LSGM exhibited a low activity for the surface exchange of oxygen, however, the mobility of the oxide ion in the bulk of LSGM was extremely high, and oxygen diffusion in LSGM was very rapid. Using an ^{18}O tracer, results showed an oxygen trace diffusion coefficient of $3.74x10^{-7}$ cm^2S^{-1} and conductivity measurements gave an oxygen trace diffusion coefficient of $3.25x10^{-7}$ cm^2S^{-1} therefore, electrical conductivity was confirmed to be ionic over the temperature range from 550 to 970 °C[12].

1.5.4 Non-Electrical Properties

1.5.4.1 Thermal Expansion

The 1994 publication by Feng and Goodenough[6] also included work on the thermal expansion of $La_{0.9}Sr_{0.1}Ga_{0.8}Mg_{0.2}O_{2.85}$. In comparison with 9 mol% YSZ, the authors observed that LSGM (at 950 °C) had a thermal expansion coefficient (TEC) of

α=10.0x10^{-6} K^{-1} versus α=10.5x10^{-6} K^{-1}. A study published in 1998[88] showed that at 950 °C, the same material showed a higher TEC of approximately α = 13.5x10^{-6} K^{-1}; this is much higher than that of 9 mol% YSZ and this is however seen to be an advantage in combination with electrode materials. Stevenson et al.[85] studied $La_{0.9}Sr_{0.1}Ga_{0.8}Mg_{0.2}O_{2.85}$ and measured a TEC of 11.6x10^{-6} K^{-1}.

1.5.4.2 Mechanical Strength

The mechanical properties of the variants of LSGM have also been studied. Drennan et al.[9] studied the flexural strength of $La_{0.9}Sr_{0.1}Ga_{0.8}Mg_{0.2}O_{2.85}$ and found that at room temperature, the average strength was 162±14 MPa, while at T=900 °C the average strength was found to be 55±11 MPa. Studies by Stevenson et al.[85] at room temperature are in relative agreement with Drennan et al.[9], finding the measured strength to be ≈150±25 MPa, however the higher temperature studies showed a strength higher than that found by Drennan et al.[9], being approximately 100±10 MPa over the temperature range 600 to 1000 °C.

Sammes et al.[89] examined the modulus of rupture (MOR) of $La_{0.8}Sr_{0.2}Ga_{1-x}Mg_xO_{3-x/2}$ (x = 0.1-0.2) and found that as the B-site dopant content increased, the MOR decreased. For the sample $La_{0.8}Sr_{0.2}Ga_{0.85}Mg_{0.15}O_{3-x/2}$, considered to have the optimum ionic conductivity, a room temperature MOR value of 139±17 MPa was determined. This is a slightly lower value than that given by Drennan et al.[9], however the system studied by Sammes et. al.[24] had a higher A-site dopant concentration, thus the results were not directly comparable. The fracture toughness of $La_{0.8}Sr_{0.2}Ga_{1-x}Mg_xO_{3-x/2}$ (x = 0.1-0.2) was also examined by Sammes et al.[89] and it was found that the solid state method of fabrication produced a material with relatively low strength as well as low fracture toughness compared to YSZ (MOR ≈ 250 MPa[85] and fracture toughness of 2.0-2.5 MPa$\sqrt{m}$ for YSZ and 150 MPa[85] and fracture toughness of 1.0-1.1 MPa$\sqrt{m}$[85]).

1.6 Applications

There are many applications for solid state electrolyte materials that conduct oxide ions. As research on LSGM based perovskites extends, applications are now being identified for this and many other oxide materials. A summary of the main applications is given, and where applicable, examples will be given.

1.6.1 Oxygen Pumps

An oxygen pump is a device that permits the flow of oxygen (as an oxide ion) across an electrolyte membrane for the purpose of controlling the oxygen partial pressure. A typical arrangement of an oxygen pump is shown in Figure 1.7, in which porous platinum electrodes are attached on both sides of a tubular solid electrolyte of calcia stabilized zirconia (CSZ) or yttria stabilised zirconia (YSZ)[90].

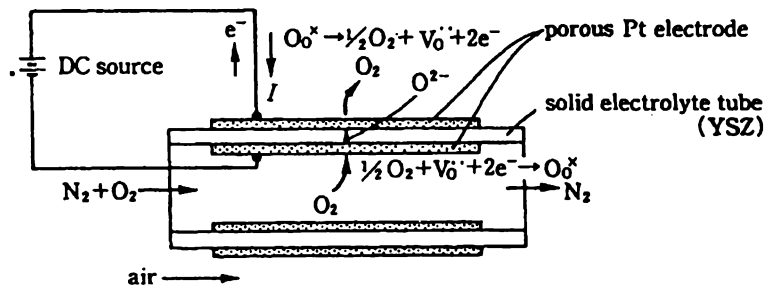

Figure 1.7. Schematic structure of an oxygen pump using YSZ solid electrolyte[91].

The principle of operation is as follows; for an oxygen concentration cell such as

$$O_2\ (P_{O_2}'),\ Pt_a\ |YSZ|\ Pt_c\ O_2\ (P_{O_2}'') \qquad (1.10)$$

there is an electromotive force (EMF) generated

$$E=(RT/4F)\ln(P_{O_2}''/P_{O_2}') \qquad (1.11)$$

where P_{O_2}"> P_{O_2}', and a = anode, c = cathode, P_{O_2}' = oxygen partial pressure at the anode and P_{O_2}" = oxygen partial pressure at the cathode.

When the Pt electrodes are short circuited, ionic current due to the oxide ions is induced in the solid electrolyte (YSZ), and oxygen is consequently transferred from the low-pressure side (Pt_a) to the high-pressure side (Pt_c). If a voltage is then applied which is greater than the cell EMF, current in the external circuit will flow from Pt_a to Pt_c. Hence, oxide transport occurs from Pt_a to Pt_c and oxygen will pass from the low to high oxygen partial-pressure side. At present these devices are mostly used for scientific purposes for the precise control of oxygen pressures.

1.6.2 Oxygen Sensors

Sensor devices measure chemical or physical quantities, and typically output an electrical signal.

Chemical sensors are classified into four types[92];

- electromotive forces (EMF) type – transducing the difference in chemical potential to EMF
- Limiting current type – transducing the concentration of species into limiting current of the electrochemical cell
- Semiconductor type – using the conductivity change of a semiconductor
- Field effect transistor (FET) type – utilising the change of the source drain-current of the FET on absorption of a chemical species onto its gate electrode.

EMF type P_{O_2} sensors use YSZ, CSZ or other oxide-ion electrolyte materials and are used in various applications. For example, the oxygen sensor used in the experimental set-up described in Chapter 4 is used to monitor the P_{O_2} of the gas flow as the gas-mixing ratio is changed. Figure 1.8 shows the basic schematic of this type of sensor, using an oxide ion conductive electrolyte (for example, YSZ). The electrolyte separates two components, the standard known gas at P_{O_2}", being, for

example, air. The gas to be measured is on the opposite side. An EMF is measured to obtain P_{O_2}', the sample gas partial pressure.

In 1997 the use of $LaGaO_3$ based oxides for a low temperature potentiometric oxygen sensor was reported[94]. $(La_{0.9}Nd_{0.1})_{0.8}Sr_{0.2}Ga_{0.8}Mg_{0.2}O_{3-\delta}$ was used as the electrolyte for the sensor and gave a response time of 15 seconds at temperatures as low as 430 °C[94].

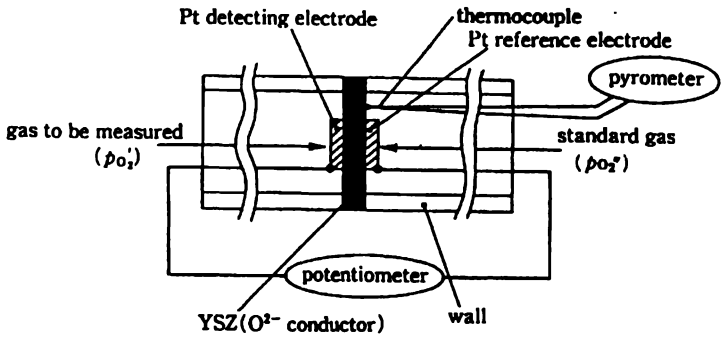

Figure 1.8 Conceptual drawing of an oxygen sensor using a YSZ solid electrolyte[93].

1.6.3 Solid Oxide Fuel Cells (SOFC's)

A solid oxide fuel cell (SOFC) is a solid-state electrochemical device producing both electricity and waste heat directly from the electrochemical conversion of a fuel with an oxidant. Because it produces electricity by electrochemical means, there is no necessity to have any moving parts, and thus the SOFC overcomes the Carnot limitation inherent in all heat engines[83]. Hence, the SOFC has high-energy efficiency, which can be further increased by using waste by-product heat in applications such as co-generation, where electrical efficiencies of greater than 50% are possible, with total efficiencies approaching 75% with co-generation[83].

1.6.3.1 Characteristics of the SOFC.

Primarily, the SOFC is the application of interest in this work. Ceramic fuel cells and in particular SOFC principles of operation are reviewed in the literature[95,96]. A

SOFC is an energy-conversion device comprised of all-solid-state components, i.e., electrolyte, anode, cathode and interconnect. The device produces electricity by electrochemically combining fuel and oxidant gases across an ionically conducting ceramic membrane. In the fuel cell, the electrolyte separates two electrodes, the anode and cathode. Fuel, such as H_2, is fed to the anode, while an oxidant, typically air, is fed to the cathode. The fuel undergoes an oxidation reaction that releases electrons to the external circuit whereas, the oxidant accepts electrons from the external circuit and undergoes reduction to form oxide ions. Oxide ions are conducted by the electrolyte material between the electrodes. The electron flow produces direct-current (dc) electricity. In a proton conducting system, H^+ are the ions conducted through the electrolyte (see Figure 1.9) compared to O^{2-} for an oxygen ion conductor, as illustrated in Figure 1.10.

The electrolyte must be of a high percentage theoretical density so that the two fuels are physically separated and have no opportunity of mixing. The cell (anode/electrolyte/cathode) is operated at a high temperature primarily to allow the ionic conductivity of the electrolyte to be high enough to produce a reasonable current density, although other factors such as reaction kinetics must also be considered.

Doped-$LaGaO_3$ is a relatively new material that shows promise as a SOFC electrolyte[1,6] because, until recently, it appeared to be stable under SOFC operating conditions.

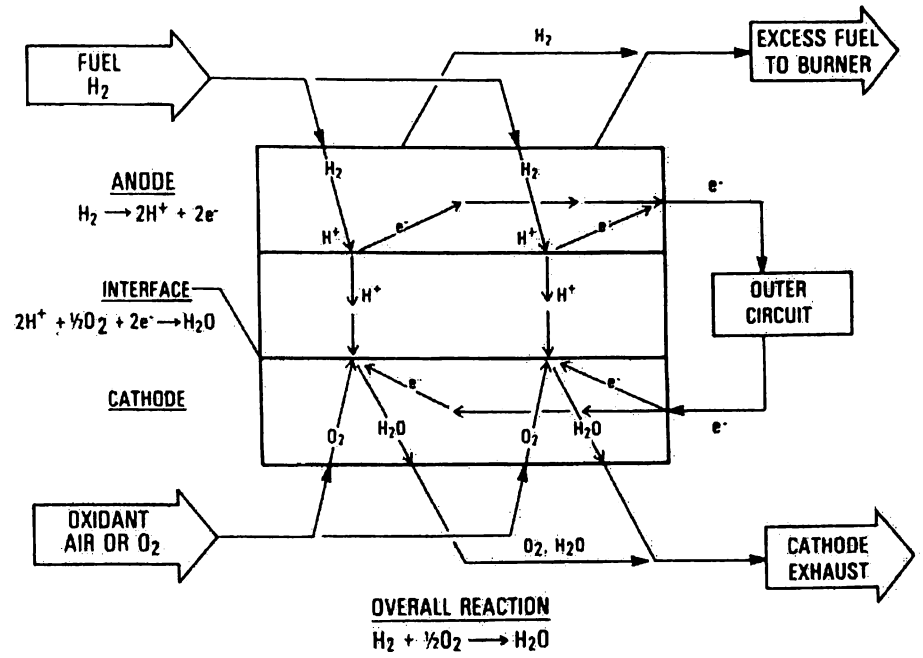

Figure 1.9. Overall summary of reactions for a proton conducting SOFC[95].

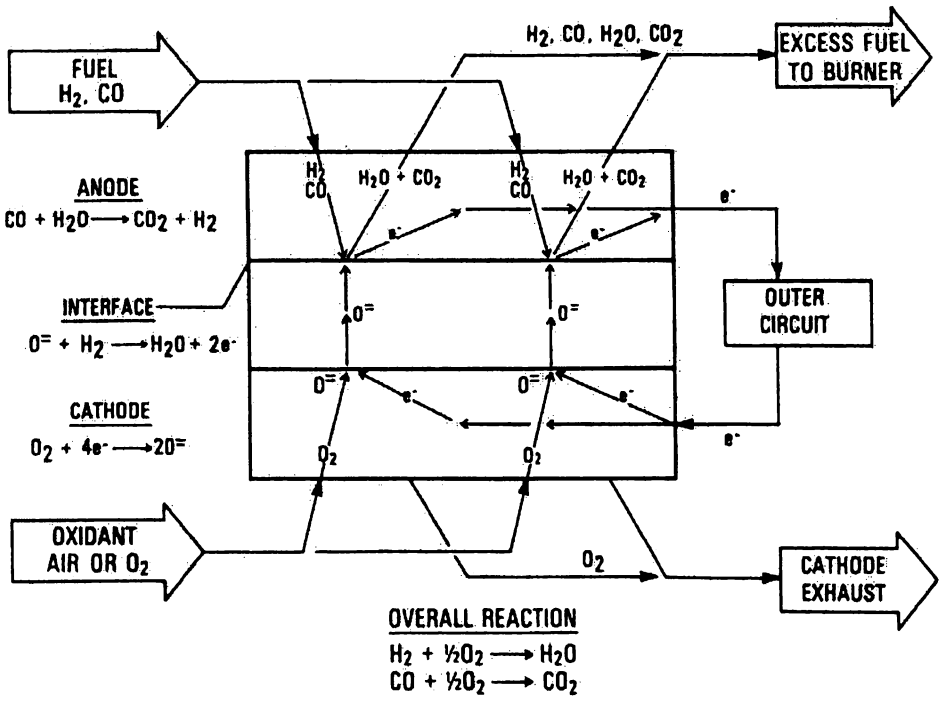

Figure 1.10. Overall summary of reactions for an oxide ion conducting SOFC[95].

1.6.3.2 LSGM as a SOFC Electrolyte

In 1995 the first SOFCs were developed by Ishihara et al.[29] using LSGM variations as the electrolyte and operating at a temperature of 1000 °C. Results showed that a large electrical power output (280.4 $mWcm^{-2}$), as well as high yields of CO and H_2, could be obtained from the fuel cell reactor where $La_{0.9}Sr_{0.1}Ga_{0.8}Mg_{0.2}O_{2.85}$ was employed, alongside a $La_{0.6}Sr_{0.4}CoO_3$ cathode.

In 1996 Ishihara et al.[97] reported the production of an intermediate temperature (800 °C) SOFC with a $LaGaO_3$ based perovskite type electrolyte. $La_{0.9}Sr_{0.1}Ga_{0.8}Mg_{0.2}O_{2.85}$ was used for the electrolyte, $Sm_{0.6}Sr_{0.4}CoO_3$ as the cathode and Ni as the anode. Results showed that the power density achieved, 0.44 W/cm^2 at 800 °C, was approximately 9 times higher than that of other SOFC where YSZ was used as the electrolyte under similar conditions[97]. By 1997, research was being published that promoted the use of LSGM as the electrolyte in a SOFC at temperatures as low as 600 to 800 °C[98]. Single-cell SOFC tests with a 500 μm-thick LSGM electrolyte showed very promising performances compared to YSZ electrolytes or a CeO_2 based electrolyte at operating temperatures (T_{op}) 600 °C ≤ T_{op} ≤ 800 °C. A steady and high maximum power density was obtained with an $La_{1-x}Sr_xCo_3$ cathode and a $SmCeO_2$ + Ni anode, having an electrolyte-anode interlayer of Sm_2O_3-CeO_2[99].

In 1998, Yamaji et al.[100] published work on the compatibility of $La_{0.9}Sr_{0.1}Ga_{0.8}Mg_{0.2}O_{2.85}$ as the electrolyte for SOFCs. Single SOFC tests using Pt as cathode and anode were undertaken and the surface morphologies of the $La_{0.9}Sr_{0.1}Ga_{0.8}Mg_{0.2}O_{2.85}$ were found to have changed, as shown in Figure 1.11.

For the cathode side, second phases were formed along grain boundaries, but there was no significant change to the surface of the grains. At the anode side, two significant compositional changes were found by secondary ion mass spectrometry (SIMS). The first was that $La_{0.9}Sr_{0.1}Ga_{0.8}Mg_{0.2}O_{2.85}$ reacted with the other components, such as alumina tubes or Pyrex glass sealant in the test cell.

Figure 1.11. Surface morphologies of (a) the anode and (b) the cathode side after a long term open circuit voltage measurement, reproduced from Yamaji et al.[100]

The second was a significant depletion of B-site ions, especially the Ga^{3+} ion, from the surface outside the effective electrode area in $La_{0.9}Sr_{0.1}Ga_{0.8}Mg_{0.2}O_{2.85}$, and the surface morphology was changed from dense to porous. Because monovalent gallium compounds, such as Ga_2O, have high vapour pressures in reducing atmospheres around $P_{O_2}=10^{-24}$ atm. and react with Pt, the Ga^{3+} depletion was ascribed to the vaporisation of the gallium component[100].

1.7 Research Direction

The aim of this section of the work presented is to examine perovskite oxide materials where the B cation of the ABO_3 structure has been varied, and to compare these results to existing data. The effect of doping on both the A and B sites of the overall structure and density of the materials was discussed. X-ray diffraction and Raman spectroscopy have been used to determine the crystal structure and purity of these materials.

1.8 References

[1] T. Ishihara, H. Matsuda & Y. Takita, *J. Am. Chem. Soc*, 1994, **116**, 3801

[2] H. U. Anderson, 14th Risø International symposium on High temperature electrochemical behaviour of fast ion mixed conductors, 1993.

[3] T. C. Mak, Gong-Du Zhou, *Crystallography in Modern Chemistry*, 1992, J. Wiley & Sons, New York.

[4] F. A. Cotton & G. Wilkinson, *Advanced inorganic chemistry*, 5th edition, 1988, J. Wiley & Sons, USA

[5] S. Geller, Acta Cryst., 1957, **10**, 243-249

[6] M. Feng & J. B. Goodenough, *Eur. J. Solid State Inorg. Chem*, 1994, **31**, 663

[7] I. Utke, C. Klemenz, H. J. Scheel & P. Näesch, *J. Crystal Growth*, 1997, **174**, 813

[8] K. Huang, R. S. Tichy & J. B. Goodenough, J. Am. Ceram. Soc, 1998, **81**, [10], 2565

[9] J. Drennan, V.Zelizko, D. Hay, F. Ciacchi, S. Rajendran & S. P. S. Badwal, *J. Mater. Chem*, 1997, **7**, [1], 79

[10] T. Ishihara, H. Matsuda & Y. Takita, *Solid State Ionics*, 1995, **79**, 147

[11] R. T. Baker, B. Gharbage & F. M. B. Marques, *J. Electrochem. Soc.*, 1997, **144**, [9], 3130

[12] T. Ishihara, T. Akbay, H. Furutani & Y. Takita in 11th International Conference on Solid State Ionics, Extended Abstracts, (Honolulu, Haaii, USA, 1997) 362

[13] J. Van herle, T. Horita, T. Kawada, N. Sakai, H. Yokokawa & M. Dokiya. In Solid Oxide Fuel Cells IV, Edited by M. Dokiya, O. Yamamoto, H. Tagawa & S. C. Singhal, *J. Electrochem. Soc.* 1995, 1082.

[14] A. Roose & A. Hausner, *Adv. Ceram. Mater*, 1988, **3**, 131

[15] A. L. Gragoo & L. P. Domingues, *J. Am. Ceram. Soc.*, 1982, **65**, 253

[16] K. Huang, M. Feng & J. B. Goodenough, *J. Am. Ceram. Soc*, 1996, **79**, [4], 1100

[17] T. Inagaki, K. Miura, H. Yoshida, J. Fujita & M. Nishimura, Solid State Ionics, 1998, **118**, 265

[18] J. Koetke, G. Huber & K. Petermann, J. of Luminescence, 1991, **48 & 49**, 564

[19] N. M. Sammes, G. A. Tompsett, R. J. Phillips, A. M. Cartner, Solid State Ionics, 1998, **111**, 1

[20] M. C. Saine, E. Husson & H. Brusset, Spectrochimica Acta, 1982, **38A**, [1], 19

[21] W. Marti, P. Fischer, J. Schefer & F. Kubel, *Zeitschrift för Kristallographie* 1996, **211**, 891

[22] S. Geller & P. M. Raccah, Physical Review B, 1970, **2**, [4], 1167

[23] P. Huang & A. Petric, *J. Electrochem. Soc*, 1996, **143**, [5], 1644

[24] R. T. Baker, B. Gharbage & F. M. B. Marques, *J. European Ceram. Soc*, 1998, **18**, 105

[25] P. S. Anderson, F. M. B. Marques, D. C. Sinclair & A. R. West, Solid State Ionics, 1999, **118**, 229

[26] K. Nomura & S. Tanase, Solid State Ionics, 1997, **98**, 229

[27] K. Huang, R. S. Tichy & J. B. Goodenough, J. Am. Ceram. Soc, 1998, **81**, [10], 2576
[28] K. Huang, M. Feng, J. B. Goodenough & M. Schmerling, J. Electrochem. Soc, 1996, **143**, [11], 3630
[29] T. Ishihara, Y. Hiei & Y. Takita, *Solid State Ionics*, 1995, **79**, 371.
[30] N. Trofimenko & H. Ullmann, Solid State Ionics, 1999, **118**, 215
[31] M. Mizuno & T. Yamada, Yogyo-Kyokai-shi, 1985, **93**, [11], 686
[32] A. Petric & P. Huang, Solid State Ionics, 1996, **92**, 113
[33] O. Yamamoto, Y. Takeda, R. Kanno & M. Noda, Solid State Ionics, 1987, **22**, 241
[34] L.-W. Tai,N. M. Nasrallah & H. U. Anderson, in; Solid Oxide Fuel Cells, eds. S. C. Singhal & H. Iwahara, PV 93-4 (The Electrochemical Society Softbound Proceedings Series, Pennington, NJ, 1993), p 241.
[35] S. Geller & E. A. Wood, *Acta Cryst.*, 1956, **9**, 563
[36] R. D. Shannon, *Acta Crystallogr.* 1976, **A32**, 751
[37] D. Waller, J. A. Lane, J. A. Kilner & B. C. H. Steele, *Materials Letters*, 1996, **27**, 225
[38] G. V. Subba Rao, C. N. R. Rao & J. R. Ferraro, Applied Spectroscopy, 1970, **24**, [4], 436
[39] X. Li, Z. Peng, W. Fan, J. Gu, M. Zhao & J. Meng, Materials Chemistry & Physics, 1996, **46**, 50
[40] E. Traversa, M. Sakamoto & Y. Sadaoka, J. Am. Ceram. Soc, 1996, **79**, [5], 1401
[41] M. Hrovat, S. Brnik, J. Holc, D. Kuscer & D. Kolar, J. Mterials Science Letters, 1997, **16**, 143
[42] Y. Wu, Z. Yu & S. Liu, J. Solid State Chemistry, 1994, **112**, 157
[43] L. Kindermann, D. Das, H. Nickel & K. Hilpert, Solid State Ionics, 1996, **89**, 215
[44] A. Pathak, S. D. Kulkarni, S. K. Date & P. Pramanik, Nanostructural Materials, 1997, **8**, [1], 101
[45] S. Venugopalan, M. Dutta, A. K. Ramdas & J. P. Remeika, Physical Review B, 1985, **31**, [3], 1490
[46] S. Music, V. Ilakovac, M. Ristic & S. Popovic, J. Materials Science, 1992, **27**, 1011.
[47] J. D. Carter, H. U. Anderson & M. G. Shumsky, J. Materials Science, 1996, **31**, 551.
[48] Y. Yasuda & T. Hikita, in Proceedings of the Second International Symposium on Solid Oxide Fuel Cells, Athens, Greece, 1991, edited by F. Gross, P. Zegers, S. C. Singhal & O. Yamamoto, 1991, 645
[49] N. Sakai, T. Kawada, H. Yokokawa, M. Kokiya & T. Iwata, Solid State Ionics 1990, **40/41**, 394
[50] B. Gilbu, H. Fjelvag & A. Kjekshus, Acta Chemica Scandinavica, 1994, **48**, 37
[51] M. Vallet-Regi, C. V. Ragel, J. Ramirez & J. M. Gonzalez-Calbet, Solid State Ionics 1993, **63-65**, 60
[52] H. E. Hofer & W. F. Kock, J. Electrochem. Soc, 1993, **140**, [10], 2889
[53] K. Zupan & D. Kolar, *in Proceedings for the 2nd European Solid Oxide Fuel Cell Conference*, (Ed. B. Thorstensen), Ulf Bossell, Uberrohrdorf, Switzerland, 1996, 289

[54] T. Kikkawa, M. Yoshinaka, K. Hirota & O. Yamaguchi, J. Materials Science Letters, 1995, **14**, 1071

[55] S. A. Howard, J. Yau & H. U Anderson, J. Am. Ceram. Soc, 1991, **75**, [6], 1685

[56] R. W. Berg, M. M. Andersen & N. J. Bjerrum, *in Proceedings for the 2nd European Solid Oxide Fuel Cell Conference*, (Ed. B. Thorstensen), Ulf Bossell, Uberrohrdorf, Switzerland, 1996, 413

[57] A. Asamitsu, Y. Moritomo, R. Kumai, Y. Tomioka & Y. Tokura, Physical Review B, 1996, **54**, [3], 1716

[58] V. B. Podobedov, A. Weber, D. B. Romero, J. P. Rice & H. D. Drew, Solid State Communications, 1998, **105**, [9], 589

[59] R. Gupta, A. K. Sood, R. Mahesh & C. N. R. Rao, Physical Review B, 1996, **54**, [21], 14899

[60] K. H. K. Kim, J. Y. Gu, H. S. Choi, G. W. Park & T. W. Noh, Physical Review Letters, 1996, **77**, [9], 1877

[61] M. A. Gilleo, Acta. Crysta. 1957, **10**, 161

[62] M. N. Iliev, M. V. Abrashev, H.-G. Lee, V. N. Popov, Y. Y. Sun, C. Thomsen, R. L. Meng & C. W. Chu. Physical Review B, 1998, **57**, [5], 2872

[63] G. Xiong, Z. Zhi, X. Yang, L. Lu and X. Wang, J. Materials Science Letters, 1997, **16**, 1068

[64] H. Druidhof, H. J. M. Bouwmeester, R. H. E. v. Doorn & A. J. Burggraaf, Solid State Ionics, 1993, **63-65**, 816

[65] S. U. Wenhui, W. U. Daiming, L. I. Xiaoyuan, M. A. Xianfeng, Z. Jianshi, Q. Zhenganan, W. Yifeng, L. Weina & G. E. Zhongjiu, *Physica B*, 1986, **139 & 140B**, 658

[66] E. M. Levin, C. R.Robbins & H.. F. McMurdie, '*Phase Diagrams for Ceramists*', (Ed. M. K. Reser), The American Ceramic Society, Ohio, U.S.A., 1964, p134

[67] W. Su, D. Wu, X. Li, X. Ma, J. Zhou, Z Qian, Y. Wang, W. Liu & Z. Ge, Physica 1986, **139 & 140B**, 658

[68] Y. Wang, Z. Quin, X. Li, X. Ma, J. Zhou, D. Wu & W. Wenhui, Jilin Dauzue Ziran Kezue Zuebao, 1987, **3**, 63

[69] U. Brendt, D. Maier & C. Keller, J. Solid State Chem., 1975, **13**, 131

[70] D. J. Durban & G. H. Wolf, American Mineralogist, 1992, **77**, 890

[71] M. Iliev, C. Thomsen, V. Hadjiev & M. Cardona, Physical Review B, 1993, **47**, [18], 12341

[72] I. G. Siny & T. A. Smirnova, Ferroelectrics, 1989, **90**, 191

[73] N. V. Porotnikov, O. I. Dondratov, K. I. Petrov & I. I. Olikov, Russian J. Inorg. Chem., 1980, **25**, [3], 383

[74] N. V. Porotnikov, S. S. Plotkin & K. I. Petrov, Russian J. Inorg. Chem., 1976, **21**, [5], 777

[75] S. Loridant, L. Abello & G. Lucazeau, J. Raman Spectroscopy. 1997, **28**, 283

[76] F. Genet, S. Loridant & G. Lucazeau, J. Raman Spectroscopy. 1997, **28**, 255

[77] C. H. Perry, B. N. Huanna & G. Rupprecht, Physical Review, 1964, **135**, [2A], A408

[78] C. H. Perry, D. J. McCarthy & G. Rupprecht, Physical Review, 1965, **138**, [5A], A1537

[79] M. C. Saine, E. Husson & H. Brusset, Spectrochimica Acta, 1981, **37A**, [11], 985

[80] S. Geller & V. B. Bala, Acta Cryst. 1956, **9**, 1019

[81] D. J. Gardiner & P. R. Graves (Eds.), *Practical Raman Spectroscopy*, Springer-Verlig, Berlin, Heideberg, (1989).

[82] G. A. Tompsett, R. J. Phillips, N. M. Sammes & A. M. Cartner, Solid State Communications, 1988, **108**, [9], 655

[83] W. Gao & N. M. Sammes, *An introduction to electronic and ionic materials*, World Scientific Publishers, Singapore, (1999)

[84] K. R. Kendall, C. Navas, J. K. Thomas & H-C zur Loye, *Solid State Ionics*, 1995, **82**, 215

[85] J. W. Stevenson, T. R. Armstrong, L. R. Pederson, J. Li, C. A. Lewinsohn & S. Baskaran, in publication, Solid State Ionics 1999

[86] K. Huang, R. S. Tichy & J. B. Goodenough, J. Am. Ceram. Soc, 1998, **81**, [10], 2581

[87] T. Ishihara, J. A. Kilner, M. Honda & Y. Takita, *J. Am. Chem. Soc*, 1997, **119**, 2747

[88] F. Tietz, Presented at the 9th International Conference on Modern Materials & Technologies (CIMTEC '98), 1998, Florence, Italy

[89] N. M. Sammes, F. M. Keppeler, H. Näfe & F. Aldinger, *J. Am. Ceram. Soc*, 1998, **81**, [12], 3104

[90] T. Kudo & K. Fueki, Solid State Ionics, 1990, VCH Publishers, New York, U.S.A., Chpt6, P67

[91] W. J. Quadakkers, H. Grainer & W. Kock, in *1st European Solid Oxide Fuel Cell Forum*, 1994 (Ed. U. Bossel), Lucerne, Switzerland, **Vol 2.** 525

[92] T. Kudo & K. Fueki, Solid State Ionics, 1990, VCH Publishers, New York, U.S.A., Chpt6, P218

[93] T. Kudo & K. Fueki, Solid State Ionics, 1990, VCH Publishers, New York, U.S.A., Chpt6, 198

[94] T. Ishihara, M. Higuchi, H. Furutani, T. Fukushima, H. Nishiguchi & Y. Takita, *J. Electrochem. Soc*, 1997, **144**, [5], L122

[95] N. Q. Minh & T. Takahashi, *Science and Technology of Ceramic Fuel Cells*, Elsevier, Amsterdam, 1995

[96] N. Q. Minh, J. *Am. Ceram. Soc*, 1993, **76**, 563

[97] T. Ishihara, H. Minami, H. Matsuda H. Nishiguchi & Y. Takita, *Denki Kagaku*, 1996, **64**, [6], 642

[98] K. Huang, M. Feng & J. B. Goodenough, *J. Am. Ceram. Soc*, 1997, **144**, [10], 3620

[99] K. Huang, R. S. Tichy & J. B. Goodenough, J. Am. Ceram. Soc, 1998, **81**, [10], 2581

[100] K. Yamaji, T. Horita, M. Ishikawa, N. Sakai & H. Yokokawa, *Solid State Ionics*, 1998, **108**, 415

Chapter Two

Introduction to ABO_3 Perovskite Protonic Conductors

2.1 Introduction

Chapter two examines the principles and conduction mechanisms observed in proton conductors. It outlines properties including the structure and conductivity of protonic perovskite solid state electrolyte materials, and gives a brief outline of their applications. It then reviews the research on $SrCeO_3$ based ceramics with particular reference to structure and conductivity.

2.2 Proton Conductivity

The proton, or hydrogen ion (H^+), is the only ion that has no electron shell of its own. Consequently, it interacts strongly with the electron density of its environment, which then takes on some of the protons' character. These ions are not subject to the usual ion-repulsion effects that make other ions spatially separate.

As a result of the small radius of the proton, the isolated H^+ ion is not present in solids under equilibrium conditions. Due to its strong polarising power, H^+ is covalently bonded to one or two electronegative ions or atoms in the surrounding system. There are at least three different bonding mechanisms for the proton[1]:

(1) The acceptor site for the proton may be an ion of the immobile lattice; for example the formation of a hydroxogroup.

(2) The proton may be attached to a mobile ion; for example an oxygen ion as illustrated in Figure 2.1, forming an hydroxyl ion, OH^- (or written $OH_o^\bullet$ using Kröger-Vink Notation).

(3) The proton may be attached to a mobile molecule, such as water or ammonia.

Since perovskite-based high temperature proton conductors (HTPC's) are host to a variety of point defects, they support several transport mechanisms, both ionic and electronic. There are a number of mechanisms that describe the motion of the proton. The mechanism of 'hopping' can be described by the Grotthuss mechanism. This mechanism has often been used to describe the reasons why protons in ice have a higher mobility than in water. In this mechanism, the proton can be considered to be attached to a polyatomic ion (the vehicle) in the lattice, such as PO_4^{3-}. Here the vehicles show pronounced local dynamics, but reside on their sites; the protons are transferred from one vehicle to another over very long distances, as illustrated in Figure 2.1, or more traditionally, as shown in Figure 2.2

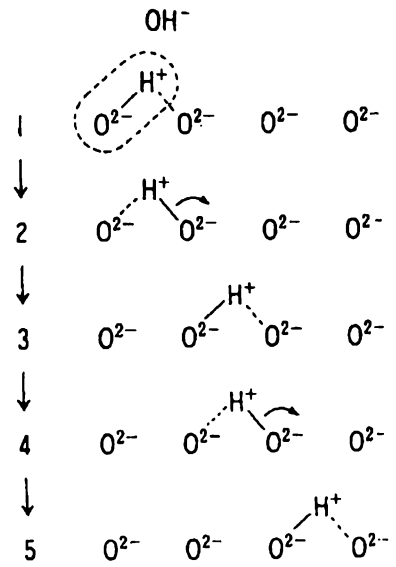

Figure 2.1 Estimated illustration of migration of protons in a perovskite-type oxide. (The figures indicate the sequence of migration)[9].

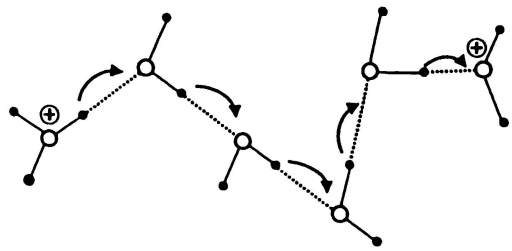

Figure 2.2 Proton conductivity according to the Grotthuss mechanism as represented by most textbooks of physical chemistry[17].

Protonic 'hopping', as illustrated by Figures 2.1 and 2.2, between oxide ions is the dominant mechanism at low temperature[2-8], while oxide ion migration is now known to occur at high temperatures[6-8].

The coexistence of these two mechanisms has resulted in speculation about hydroxyl migration[10-12]. *p*-type electronic conduction has been noted by most investigators, but only rarely[13-16] has *n*-type conduction been observed in HTPCs.

Another mechanism often applied to proton diffusion is the 'vehicle' mechanism. Here the proton diffuses with a so-called "vehicle", such as H_3O^+. The counter diffusion of the unprotonated species, in this case H_2O, allows for the net flow of protons in the opposite direction. Such a mechanism is not possible where the vehicle and vehicle+proton have charges of the same sign, as is the case of OH^-/O^{2-} system[1].

2.3 Protonic Carrier Generation

The oxide first shown to have predominantly proton conductivity was acceptor doped ThO_2 at low oxygen partial pressure (high hydrogen partial pressure) and temperatures above 1200 °C[17].

Protonic carriers in oxides arise from the dissolution of water vapour and are therefore influenced by reactions with the gaseous environment. The generation of protons depends, in the first instance, on the creation of oxide ion vacancies through doping, for example, $M=Y^{3+}$ in $SrCe_{1-x}M_xO_{3-\delta}$. Oxygen vacancies are formed to

maintain electroneutrality. Water can then be incorporated into the lattice via equation (2.1),

$$\frac{1}{2}H_2O(g)+\frac{1}{2}V_o^{\bullet\bullet}\rightarrow H_i^{\bullet}+\frac{1}{2}O_o^{x} \qquad (2.1)$$

where $V_o^{\bullet\bullet}$ denotes an oxygen vacancy, $H_i^{\bullet}$ a proton and O_o^{x} an oxide ion occupying a normal oxygen site. The equilibrium equation for this reaction gives:

$$H_i^{\bullet}=K_{2.1}[V_o^{\bullet\bullet}]^{\frac{1}{2}}(P_{H_2O})^{\frac{1}{2}} \qquad (2.2)$$

where $K_{2.1}$ is the equilibrium reaction constant for the reaction described in equation 2.1. The dissolution of oxygen causes the generation of electron holes ($h^{\bullet}$) as described below,

$$\frac{1}{4}O_2(g)+\frac{1}{2}V_o^{\bullet\bullet}\rightarrow\frac{1}{2}O_o^{x}+h^{\bullet} \qquad (2.3)$$

and from the equilibrium equation of this reaction one obtains:

$$p=K_{2.3}[V_o^{\bullet\bullet}]^{\frac{1}{2}}(P_{O_2})^{\frac{1}{4}} \qquad (2.4)$$

where $K_{2.3}$ is the equilibrium reaction constant for the reaction described in equation 2.3, and where p denotes the electron hole. Other reactions that may occur in the lattice include

$$H_2O+V_o^{\bullet\bullet}\rightarrow 2H^{+}+O_o^{x} \qquad (2.5)$$

and

$$H_2O+O_o^{x}+V_o^{\bullet\bullet}\rightarrow 2(OH)_o^{\bullet} \qquad (2.6)$$

Once created, the protonic defects (and any remaining oxygen vacancies) can migrate via mechanisms suggested earlier, see Section 2.2. From the equilibrium equations

2.2 and 2.4, it is apparent that protonic and *p*-type electronic conductivity are dependent on the water vapour pressure and oxygen partial pressure respectively[13,18]. Loss of oxygen, at low oxygen partial pressure, proceeds by the generation of electrons:

$$O_o^x \rightarrow V_o^{\bullet\bullet} + 2e' + \frac{1}{2}O_2 \qquad (2.7)$$

and the equilibrium equation for the reaction yields:

$$n = K_{2.7}[V_o^{\bullet\bullet}]^{-\frac{1}{2}}(P_{O_2})^{-\frac{1}{4}} \qquad (2.8)$$

where $K_{2.7}$ is the equilibrium reaction constant for the reaction described in equation 2.7, and where n denotes the electron concentration. From equation 2.8, it is apparent that *n*-type electronic conductivity increases with decreasing oxygen partial pressure. The protons produced in the cases described above are considered to be interstitial in nature, although the hydroxide ions are considered to migrate via a vacancy mechanism, or between sites adjacent to the oxygen ions. As discussed by Norby[19], the proton in perovskite proton conductors, because of its small size, does not occupy a true interstitial site but attaches to an oxide ion, thus forming an hydroxyl ion $OH_o^{\bullet}$ as described in equation 2.6. It should be noted that protons present as interstitials, and hydroxyls substituting for oxide ions, both have the same effective charge of 1^+.

The variation of conductivity with oxygen partial pressure for perovskite proton conductors has been described in earlier papers by the following expression[4,14,20]:

$$\sigma_{tot} = \sigma_i + \sigma_n^{\circ} Po_2^{-1/4} + \sigma_p^{\circ} Po_2^{1/4} \qquad (2.9)$$

where σ_{tot} represents the total conductivity of the system, σ_i the P_{O_2}-invariant ionic component and σ_n° and σ_p°, represent the *n*- and *p*-type electronic components respectively, extrapolated to an oxygen partial pressure of 1 atm., as illustrated in Figure 2.3. For doped strontium cerate in the presence of water vapour, the majority charge carrier is the proton at intermediate oxygen partial pressure, but at $P_{O_2} > 0.01$ atm., depending on the temperature, the conductivity becomes mixed

ionic/electronic. Although the holes remain minority carriers, their relatively high mobility means that the material shows *p*-type electronic conductivity.

With ABO_3 perovskite type systems, when the A-site is substituted with an appropriate lower valency cation, oxygen vacancies are formed to maintain electroneutrality. The defect concentrations must satisfy the electroneutrality condition (see Appendix 1 for Kröger Vink Notation):

$$[V_o^{\bullet\bullet}] + p - n - 2[M_B^{'}] = 0 \qquad (2.10)$$

and the conservation of the number of anion sites.

$$[V_o^{\bullet\bullet}] + [O_o^{x}] = 3 \qquad (2.11)$$

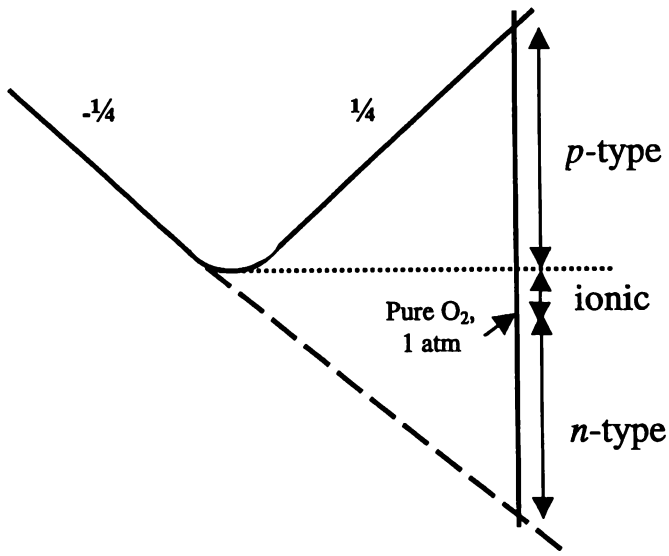

Figure 2.3 Schematic where σ_i represents the P_{O_2}-invariant ionic component and σ_n° and σ_p° represent the *n*- and *p*-type electronic components respectively, extrapolated to an oxygen partial pressure of 1 atm.

Doping of the B-site in an ABO_3 perovskite with acceptor dopants is expected to increase the conductivity due to increased oxygen vacancies, protons and holes, but the full relevance and effects of this influence are unknown.

2.4 Perovskite Proton Conductor Development

The systematic investigation of proton conducting perovskite type oxides (ABO_3) started with the work of Takahashi and Iwahara in 1980[21]. Several oxides of the ABO_3 perovskite (see Chapter 1, Section 1.3) type structure have been shown to be good conductors, the most well known of these are the acceptor doped Sr and Ba cerates, and the Sr, Ba and Ca zirconates. These oxides have been investigated for possible use in solid oxide fuel cells (SOFC), hydrogen separation membranes or hydrogen sensors[2-4,22-24]. A typical example of a proton conducting oxide of this class is the substituted solid solution material based on the perovskite oxide $SrCeO_3$, $SrCe_{0.95}Yb_{0.05}O_{2.975}$, which exhibits protonic conduction in water and hydrogen-containing atmospheres at elevated temperatures[2]. This material is a substituted solid solution based on the perovskite-type oxide $SrCeO_3$, in which 5% of Ce is replaced by Yb. Other perovskite–type oxides based on $SrCeO_3$ and $BaCeO_3$, in which trivalent cations are partially substituted for cerium are also protonic conductors under the same conditions described above[2,25-27]. The general formula is written as $SrCe_{1-x}M_xO_{3-\delta}$ or $BaCe_{1-x}M_xO_{3-\delta}$ where M is a rare earth element, x is less than its upper limit of solid solution formation range (usually less than 0.2) and δ is the oxygen deficiency per unit formula, normally x/2. Their protonic conductivities in a hydrogen atmosphere are of the order of 10^{-3}~10^{-2} Scm^{-1} at 600 ~ 1000 °C, as shown in Figure 2.4. The protonic conduction in these oxides was verified by electrochemical hydrogen- or water-vapour- containing atmospheres at elevated temperatures. As illustrated in Figure 2.7, the occurrence of either H_2O or O_2 in the out-gas stream identifies the conducting nature of the electrolyte used.

After the discovery of $SrCeO_3$-based protonic conductors, $KTaO_3$-based oxides[28,29] were reported to have protonic conduction at high temperatures [$3.5x10^{-3}$ Scm^{-1}], although the conductivities were not as high as those of the cerate-based perovskite-

type oxide ceramics. Some doped zirconates based on $CaZrO_3$, $SrZrO_3$ or $BaZrO_3$[9,30] were also confirmed to exhibit the same behaviour as the cerates although their conductivities were rather low, as shown in Figure 2.4.

Among the oxides described above, $BaCeO_3$-based ceramics show the highest conductivity, approximately $5.5x10^{-1}$ Scm^{-1} at 1000 °C for $BaCe_{0.9}Nd_{0.1}O_{3-\delta}$[31]. However, the contribution of oxygen ions to the total conduction increases markedly as the temperature is raised[26,32-34]. Although the conductivity of $SrCeO_3$-based ceramics is rather low (approximately $9.5x10^{-1}$ Scm^{-1} at 1000 °C[31]), the transport number of protons is higher than that of $BaCeO_3$-based ceramics. The conductivities of zirconate-based ceramics are lower than those of the cerates, being approximately $6.5x10^{-2}$ Scm^{-1} at 1000 °C[31], however they are superior to the cerates with respect to their chemical and mechanical strength, making them easier to utilise for fuel cell applications.

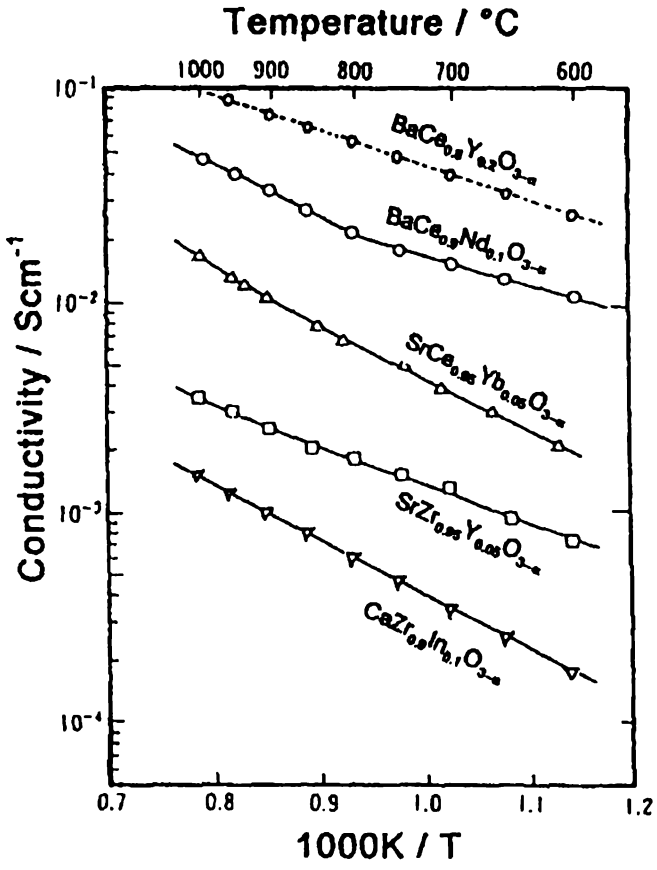

Figure 2.4. Conductivities of typical proton conducting perovskite-type oxide ceramics under hydrogen gas atmosphere, reproduced from Iwahara[31].

In the past four years, Nowick et al.[35] have reported a series of new protonic conductors of the types $A_2(B'B'')O_3$ and $A_3(B'B'')O_9$ in which the A ions are always charged 2^+, and the B' and B" ions have 3^+ and 5^+ in the former system and 2^+ and 5^+ in the latter system.

In all these systems, domains of different conductivity (ionic, electron or hole conduction) can be observed, depending on the partial pressures of oxygen (P_{O_2}), water vapour (P_{H_2O}) and temperature. Thus, the conductivity of cerates and other perovskite oxides[22-23] can be dominated by mobile protons, oxygen vacancies, or by *p*- or *n*-type electronic defects depending on the experimental conditions, as shown in Figure 2.5.

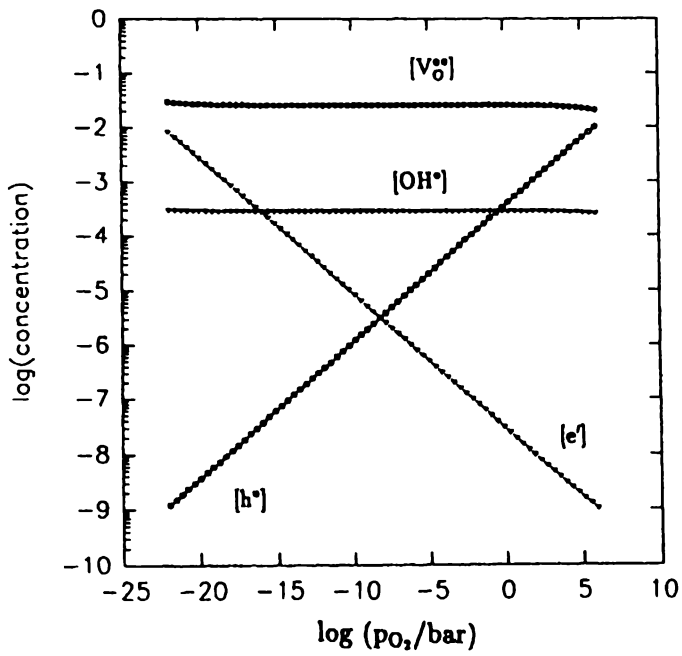

Figure 2.5 Simulated Kröger-Vink diagram at T=700 °C for $SrCe_{0.95}Yb_{0.05}O_{3-\delta}$, $P_{H_2O} = 10^{-6}$ bar. The dependence of the four most prominent defect types on P_{O_2} is shown[36].

2.5 Possible Applications

Various kinds of applications can be devised using proton-conducting ceramics. Since this class of conductor works at temperatures of several hundred degrees Celsius, they can be used as materials for high temperature devices. Such devices are based on electrochemical principles using the proton conductor as a solid electrolyte membrane. Such devices consist of:

*electrode/**proton conducting Electrolyte**/electrode*

in which the electrochemical reactions, such as ionisation of hydrogen and the discharge of proton at the electrodes, takes place.

In regard to possible applications, proton-conducting ceramics, usable at elevated temperatures, have important advantages in comparison with low temperature type systems. They can be used in-situ at high temperature, for example, as a hydrogen sensor for high temperature industrial processes. High temperature protonic conductors are applicable not only for sensors but also for high electrolytic current applications. In these devices, high temperature is more advantageous since electrode reactions take place more readily than at low temperature and, therefore, polarisation is lower, which results in higher efficiency operation.

2.5.1 Hydrogen Sensors

The principle of a hydrogen concentration cell is well known and illustrated in Figure 2.6(a). A gas cell, constructed from a proton-conducting solid as an electrolyte, gives rise to an electromotive force (EMF), due to the difference in hydrogen partial pressure between two electrode compartments. In this case, the electrode with higher hydrogen partial pressure is the negative terminal (anode). The theoretical EMF of the cell (assuming a transport number of 1) is thus given by:

$$E_o = \frac{RT}{2F} \ln \frac{P_{H_2}(I)}{P_{H_2}(II)} \qquad (2.12)$$

Where P_{H_2}(I) and P_{H_2}(II) are the partial pressures of hydrogen in compartments (I) and (II) respectively, and R, F and T have their usual meanings.

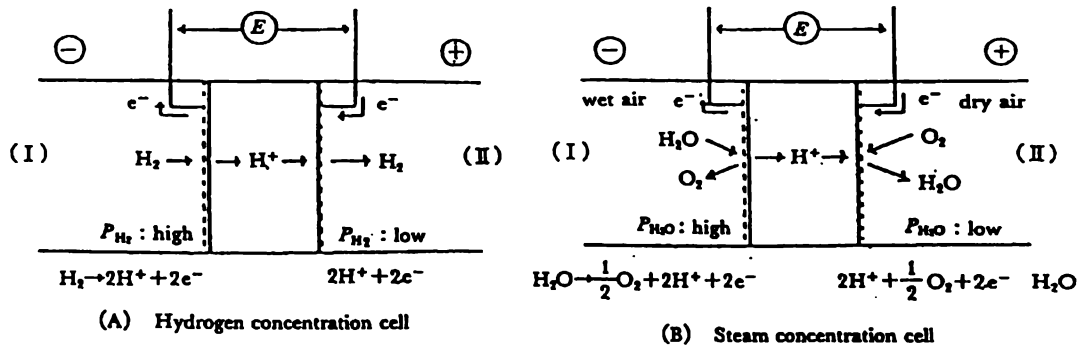

Figure 2.6. Concept of hydrogen (a) and steam (b) concentration cells

In equation 2.12, if P_{H_2}(I) is known and constant, the partial pressure in compartment (II) may be estimated from the EMF of the cell, and thus may function as a hydrogen sensor. In this case, E_o is proportional to the logarithm of P_{H_2}(II). Galvanic cell-type hydrogen sensors, steam sensors and hydrocarbon sensors usable at high temperature, can be fabricated[37]. They are essentially based on the principle of the hydrogen concentration cell using a proton conducting solid electrolyte. For the measurement of hydrogen activity in fused aluminium in the casting process, this type of hydrogen sensor has been commercialised by a Japanese company using a $CaZr_{0.9}In_{0.1}O_{3-\delta}$ ceramic[24]. This sensor may also be applied to other fused metals such as zinc or copper[24].

2.5.2 Steam Sensors

The concept of the steam concentration cell is schematically illustrated in Figure 2.6(b). When air, with a different humidity, is introduced into each electrode compartment, the cell generates an EMF depending on the difference in the partial pressure of water vapour; that is, the cell acts as the steam concentration cell. The electrode, with higher humidity, is the anode in this cell. Electrode reactions of this cell are as follows:

$$\text{cathode: } 2H^+ + \frac{1}{2}O_2 + 2e^- \rightarrow H_2O$$

$$\text{anode: } H_2O \rightarrow 2H^+ + \frac{1}{2}O_2 + 2e^-$$

The theoretical EMF of the cell is given by:

$$E^\circ = \frac{RT}{2F}\ln\left(\frac{P_{H_2O}(I)}{P_{H_2O}(II)}\right)\left(\frac{P_{O_2}(II)}{P_{O_2}(I)}\right)^{\frac{1}{2}} \qquad (2.13)$$

Where P_{H_2O} and P_{O_2} are the partial pressures of water vapour and oxygen, respectively. When $P_{O_2}(I)$ is close to $P_{O_2}(II)$, as in ambient atmospheres with different humidities, E° can be simplified as:

$$E^\circ = \frac{RT}{2F}\ln\left(\frac{P_{H_2O}(I)}{P_{H_2O}(II)}\right) \qquad (2.14)$$

In equation 2.14, if $P_{H_2O}(II)$ is known and is constant, the partial pressure of compartment (I) may be estimated from the EMF of the cell.

Iwahara and Hibino[38] have published work relating to ethanol, hydrocarbon and CO_2 sensors which have been demonstrated to operate, by way of experiments, using high temperature proton conductors. There are many other variations and possible applications for proton conductors and future research looks promising. Perhaps the most important application of proton conductors at the moment, in regard to environmental applications, is that of the fuel cell.

2.5.3 High temperature Fuel Cells

The use of a protonic conductor as a solid electrolyte for fuel cells has distinctive features compared with that of the oxide ion conductor. As illustrated in Figure 2.7, when a protonic conductor is used instead of an oxide ion conductor, fuel circulation is unnecessary in the case of hydrogen fuel cells, as no water molecules are generated

at the fuel electrode. Furthermore, in the case of hydrocarbon fuel cells, only thermally produced hydrogen is consumed as a fuel, and residual parts can be brought out as the useful reformed products (e.g. ethylene from ethane).

A laboratory-scale hydrogen fuel cell using a $SrCe_{0.95}Yb_{0.05}O_{3-\delta}$ ceramic as an electrolyte membrane has been shown to work at 800~1000 °C[39]. When this cell was discharged, it generated water vapour at the cathode at the theoretical rate calculated from Faraday's law, indicating that the conduction in the electrolyte was predominantly protonic.

The fuel cells using $BaCeO_3$-based electrolytes generated much higher power than those using $SrCeO_3$-based electrolytes[25,33,40]. However, they generated water vapour at both electrodes suggesting that the conduction in the electrolyte was both protonic and oxide ion.

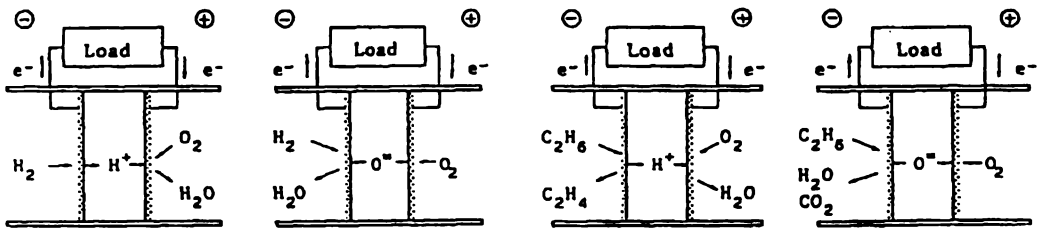

(a) Hydrogen fuel cells (b) Ethane fuel cells

Figure 2.7. Comparison of protonic conductor with oxide ionic conductor in the case of hydrogen–fuelled and ethane-fuelled cells[3].

2.6 $SrCeO_3$-based material review

2.6.1 Introduction

Among the oxides described above, $BaCeO_3$-based ceramics show the highest conductivity, as described in Figure 2.4. However, the contribution of oxygen ions to the conduction grows markedly as the temperature is raised[26,32-34], as shown in Figure 2.8, where the oxide transference numbers of two $BaCeO_3$ based materials approach 1.0 at higher temperatures[7,26].

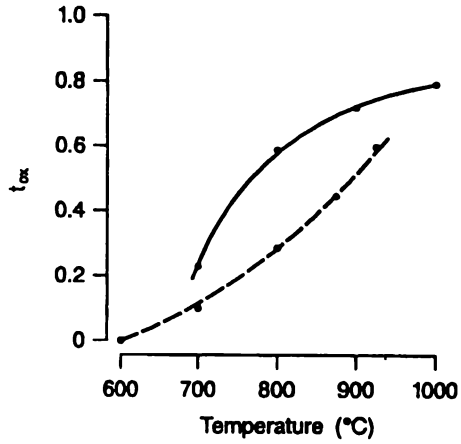

Figure 2.8. Oxide ion transference numbers for two perovskite proton conductors: — $BaCe_{0.9}Nd_{0.1}O_{2.95}$ and ---- $BaCe_{0.9}Gd_{0.1}O_{2.95}$[41]

Although the conductivity of $SrCeO_3$-based ceramics is lower (~$9x10^{-1}$ Scm^{-1} for $SrCe_{0.95}Yb_{0.05}O_{2.975}$ at 1000 °C versus ~$1x10^{-1}$ Scm^{-1} for $BaC_{0.8}Y_{0.2}O_{2.9}$ at 1000 °C[31]), the transport number of protons is higher than that of the $BaCeO_3$-based ones (t_{prot} = 0.96)[41]. As explained in Chapter 1, section 1.5.3.1, when the ionic conductivity (σ_i) of a material is quoted, the transport (or transference) number (t_i) is also given. This is described in equation 2.15

$$t_i = \sigma_i/(\sigma_i + \sigma_e + \sigma_h) \qquad (2.15)$$

where, σ_e = *n*-type (electron) conductivity and σ_h = *p*-type (hole) conductivity.

For an ionic conductor, the value for the transport number is approximately 1. The electronic (t_n) or electron hole (t_p) transport number can also be examined. In this case, the higher the transport number, the higher the electronic conductivity.

There are a number of different methods for determining the transport number of a material. However, the most commonly used technique is known as the EMF method. In order to measure the proton transport number, a steam cell is constructed using a specimen disc as the solid electrolyte:

Gas I, Pt/specimen disc/Pt, gas II

(P_{H_2O}(I)) (P_{H_2O} (II))

The partial pressure of water vapour, P_{H_2O}, in the gas is controlled by saturating the water vapour at a given temperature, and P_{O_2} at both electrodes is kept the same. The theoretical electromotive force, E^o, of a steam concentration cell is given by equation 2.14. When the specimen electrolyte exhibits some electronic conduction, the measured EMF, *E*, is lowered from E^o to some extent. If the electrode reactions take place reversibly, then the ionic transport number t_i can be determined by equation 2.16

$$t_i = E/E^o \qquad (2.16)$$

and the proton transport number, $t_h\bullet$ can be determined as the ratio of measured EMF, *E*, to theoretical EMF, E^o.

Unlike Y_2O_3-doped $BaCeO_3$, which undergoes a structural transition at approximately 800 °C[42], $SrCeO_3$ based materials remain isostructural with $GdFeO_3$, as an orthorhombic P*nma* structure, up to 1000 °C[43]. This feature makes $SrCeO_3$ based perovskite materials ideal to study in regards to structure and electronic properties as complications due to phase changes are eliminated over the temperature regime studied (600 to 800 °C in this work).

Much of the research conducted on structural properties and electrical conductivity has been directed towards $SrCe_{0.95}Yb_{0.05}O_{2.975}$, due to its high temperature proton conduction. However, $SrCe_{1-x}Y_xO_{3-\delta}$ is an acceptable substitute, giving only a small drop in conductivity, with the added benefit of yttrium being cheaper than ytterbium. The effective ionic radius, r, of Y^{3+} is 0.89 Å according to the tabulation of Shannon[44], only slightly greater than that of Yb^{3+}, 0.86 Å[44], and therefore causes only a very small change in distortion of the lattice and size of the vacancy produced.

2.6.2 Structure

The crystal structure of the perovskite-like high temperature protonic conductor $SrCeO_3$ has been studied with single crystal[43] and powder X-ray diffraction[43], and neutron diffraction[45,46]. $SrCeO_3$ crystallises in the orthorhombic space group P*bnm* (No 62), Z=4 with the unit cell parameters a = 6.0117 Å, b = 6.1538 Å and c = 8.5886 Å[43]. However, P*bnm* is not standardised in the International Tables[47], therefore, structural work has been based on the standardised space group P*nma*. The crystal structure of $SrCeO_3$ is illustrated in Figure 2.9.

The crystal structure of $SrCe_{0.85}Y_{0.15}O_{3-\delta}$ has also been studied[45], and is isostructural with the standardised $SrCeO_3$ (P*nma*) and crystallises in the distorted perovskite-like structure, also refined to the space group P*nma*, (No 62).

Part of the research undertaken in this thesis is directed towards studying the effect of the Y_2O_3 dopant concentration on the structure of the $SrCe_{1-x}Y_xO_{3-\delta}$ (where x=0.025, 0.05, 0.075, 0.1, 0.15 and 0.2) and $Sr_{0.995}Ce_{0.95}Y_{0.05}O_{2.975}$, and to look at the effect on relative and calculated density of each material.

2.6.3 Conductivity

Extensive research has been undertaken to study the electrical properties of doped $SrCeO_3$ in order to increase the understanding of effects of oxygen and water partial pressure changes on conductivity, and to study the mechanism of proton conduction.

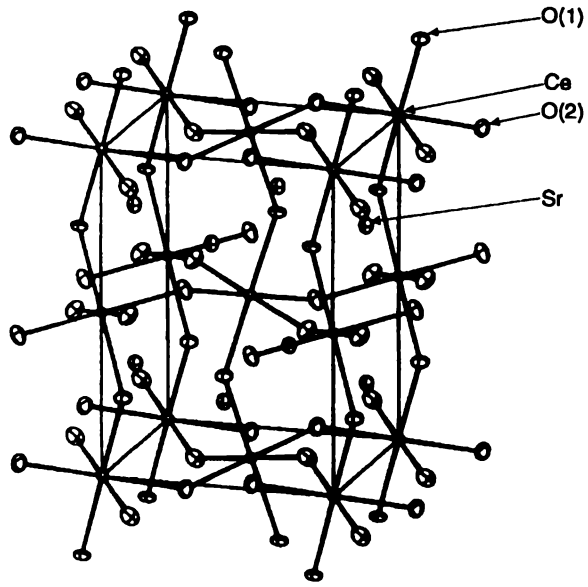

Figure 2.9. Unit cell viewed along the *b* axis (*c* axis is vertical) of orthorhombic $SrCeO_3$ in the P*bnm* setting with cerium atoms positioned at (0,0,0). Ce-O bonds are indicated to illustrate the corner-sharing octahedral framework while strontium atoms are 'free'. The O(1) position (apical oxygen) links the octahedra along the *c* axis while the O(2) position (equatorial oxygen) links the octahedra in the basal plane perpendicular to the *c* axis[45].

These oxides are unique host conductors in respect that they have no host constituents that liberate the conduction of ions (protons). Experimental studies have shown that these oxides can dissolve hydrogen or water vapour to form protons, which act as charge carriers. The solubility of hydrogen (or water) in $SrCeO_3$-based oxides was determined to be considerably larger than in any other oxides[48,49].

Previous studies on the electrical properties of $SrCeO_3$ based materials can be summarised as follows:

(1) These sintered oxides have only *p*-type conduction (hole conduction) in an atmosphere free from hydrogen or water vapour[5,50].

(2) When water vapour or hydrogen is introduced to the atmosphere, electronic conductivity decreases and proton conduction soon appears. It has now been postulated that proton conduction occurs in the oxides at the expense of electron holes initially present in the crystals[51,52].

(3) A steam concentration cell using a sintered specimen as an electrolyte membrane showed a stable electromotive force, and that a steady current can be drawn from the cell[53,54].

(4) A hydrogen concentration cell constructed with the same electrolyte also has stable characteristics[53,55].

(5) Pure $SrCeO_3$ has low electronic conductivity in an oxygen atmosphere and does not behave as a proton conductor in a hydrogen-containing atmosphere[5].

(6) Partial substitution by aliovalent cations such as Yb^{3+}, Sc^{3+} and Y^{3+} for the Ce^{4+} site in the perovskite-type crystal $SrCeO_3$ seem to play an important role in the appearance of proton conduction, however increasing the dopant cation concentration does not automatically cause an increase in total conductivity. Research has been undertaken to determine which types of defects (dopant cations themselves or oxygen vacancies resulting from doping) are essential for the formation of protonic charge carriers. This was undertaken experimentally by controlling the stoichiometric amount of oxygen deficiency in $SrCeO_3$ with an appropriate amount of trivalent yttrium, tetravalent zirconium or pentavalent niobium substituents for cerium[52]. Increasing stoichiometric oxygen non-stoichiometry (α in Figure 2.10) increases conductivity, but increasing dopant concentration does not have the same effect[31], as illustrated in Figure 2.10.

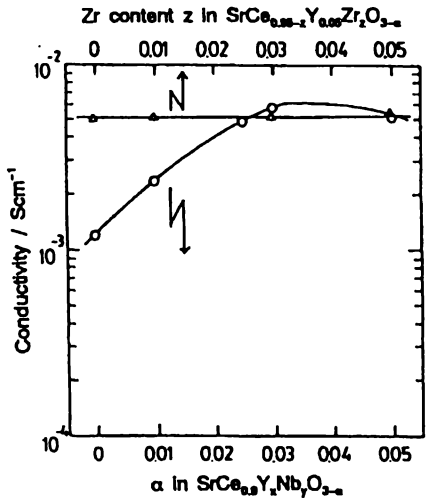

Figure 2.10. Proton conductivities of $SrCe_{0.9}Y_xNb_yO_{3-\delta}$ (O) and $SrCe_{0.95-z}Y_{0.05}Zr_zO_{3-\delta}$ (Δ) at 800 °C in hydrogen atmosphere[31,52].

(7) Proton conductivity increases in proportion to $P_{H_2O}^{1/2}$ and is independent of P_{O_2} suggesting interstitial-type protons, and not hydride-type ions, are thus provided from H_2O. Hole conductivity follows a $P_{O_2}^{1/4}$ dependency in the P_{O_2} region examined (from 1 to 10^{-3} atm. P_{O_2}) by Uchida et al.[5]. Figure 2.11 shows a three dimensional representation of total conductivity σ_{total} and the proton conductivity $\sigma_{H^\bullet}$ as a function of P_{O_2} and P_{H_2O}, where P_{O_2} is restricted to the region where electronic conduction is exclusively due to holes.

(8) Total conductivity decreases with increasing P_{H_2O} and increases with increasing P_{O_2} at a given temperature. Such experimental results can be explained if the protons were provided from the water at the expense of the electron holes[5].

These results indicate that oxide ion vacancy relates directly to proton formation and conduction in $SrCeO_3$-based conductors. Thus, hydrogen from water molecules dissolve in the oxide and behave as charge carriers to form a proton conductor.

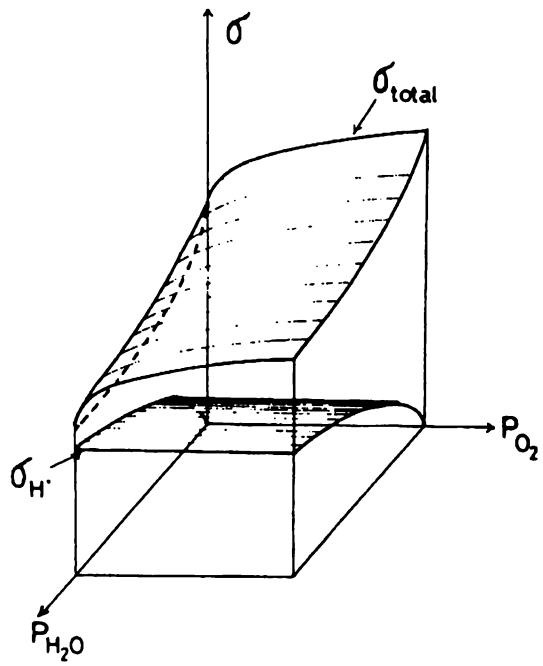

Figure 2.11. Schematic illustration of a three dimensional representation of total conductivity σ_{total} and the proton conductivity $\sigma_{H^\bullet}$ as a function of P_{O_2} and P_{H_2O}, where P_{O_2} is restricted to the region where electronic conduction is exclusively due to holes[52].

2.7 Research Direction

$SrCeO_3$-based ceramic electrolytes have been extensively investigated both electrically and structurally, due to the interest in their proton conducting properties[2-4]. However, little information exists on the effect of dopant concentration each separate constituent of the total conductivity. The objective of this work was to study a $SrCeO_3$ based system, and resolve the total conductivity into its *n*- (electron) and *p*- (hole) type electronic components, and the ionic component. This was undertaken for a number of samples with increasing Y_2O_3 dopant concentration, and for $Sr_{0.995}Ce_{0.95}Y_{0.05}O_{2.975}$. Once the total conductivity had been separated into its separate responses, each constituent was studied with regard to changing yttrium concentration and changing partial pressure of water. A systematic study of yttrium doped $SrCeO_3$ of this scope has not been undertaken before.

Structural investigations were also undertaken to ascertain the effect of increasing Y_2O_3 dopant concentration on the structure and density of $SrCe_{1-x}Y_xO_{3-\delta}$.

2.8 References

[1] W. Gao & N. M. Sammes, *An introduction to electronic and ionic materials*, World Scientific Publishers, Singapore, (1999).

[2] H. Iwahara, T. Esaka, H. Uchida & N. Maeda, *Solid State Ionics*, 1981, **3/4**, 359.

[3] H. Iwahara, *Solid State Ionics*, 1988, **28-30**, 573.

[4] I. Kosacki & H. L. Tuller, *Solid State Ionics*, 1995, **80**, 223.

[5] H. Uchida, N. Maeda & H. Iwahara, *Solid State Ionics*, 1983, **11**, 117

[6] H. Iwahara, T. Uchida & K. Morimoto, *J. Electrochem. Soc*, 1990, **137** [2], 462

[7] H. Iwahara, T. Yajima, H. Uchida & K. Morimoto, in: Proc. 2nd Inter. Symp. on Solid Oxide Fuel Cells (Athens, 1991). Eds. P. Gros, P. Zegers, S. C. Singhal & O. Yamamoto (IC Commission, Luxembourg, 1991), 229

[8] T. Yajima, H. Iwahara & H. Uchida, *Solid State Ionics*, 1991, **47**, 117

[9] H. Iwahara, T. Yajima, T. Hiabino, K. Ozaki & H. Suzuki, *Solid State Ionics*, 1993, **61**, 65

[10] N. Bonanos, B. Ellis, K. S. Knight & M. N. Mahmood, *Solid State Ionics*, 1989, **35**, 179

[11] R. L. Cook & A. F. Sammells, *Solid State Ionics*, 1991, **45**, 311

[12] A. F. Sammels, R. L. Cook, J. H. White, J. J. Osborne & R. C. Macduff, Proc. Conf. On Ceramic Electrolytes (Snowbird, Utah, 1991)
[13] N. Bonanos, *Solid State Ionics*, 1992, **53-56**, 967
[14] E. O. Ahlgren, J. R. Hansen, N. Bonanos, F. W. Poulsen & M. Mogensen, Proc. 17th Risø International Symposium on Materials Science. Editors, F. W. Poulsen, N. Bonanos, S. Linderoth, M. Mogensen and B. Zachau-Christiansen 1996.
[15] N. Bonanos & M. N. Mahmood, presented at Royal Society of Chemistry Polar Solids Discussion group meeting (Heriot-watt University, Edinburgh, 1989)
[16] U. Reichel, R. R. Arons & W. Schilling, *Solid State Ionics*, 1996, **86-88**, 639
[17] K. D. Kreuer, *Solid State Ionics*, 1997, **94**, 55
[18] Y. Larring & T. Norby, *Solid State Ionics*, 1997, **97**, 523
[19] T. Norby, *Solid State Ionics*, 1990, **40-41**, 849
[20] N. Bonanos, *J. Phys. Chem. Solids*, 1993, **54**, 867
[21] T. Takahashi & H. Iwahara, Revue de Chimie Minerale, 1980, **17**, 243
[22] H. Iwahara, H. Uchida & N. Maeda, *J. Power Sources*, 1982, **7**, 193.
[23] H. Iwahara, H. Uchida & I. Yamasaki, *Int. J. Hydrogen Energy*, 1987, **12**, 73.
[24] T. Scherban & A. S. Nowick, *Solid State Ionics*, 1989, **35**, 189.
[25] H. Iwahara, H. Uchida, K. Ono & K Ogaki, *J. Electrochem. Soc*, 1988, **135**, 529
[26] N. Bonanos, B. Ellis & M. N. Mahmood, *Solid State Ionics*, 1991, **44**, 305
[27] R. C. T. Slade & N. Shigh, *Solid State Ionics*, 1993, **61**, 111
[28] W. Lee, A. S. Nowick & L. A. Boaturner, *Solid State Ionics*, 1986, **18/19**, 989
[29] T. Norby & P. Kofstad, *J. Am. Ceram. Soc.* 1984, **67**, 786
[30] T. Yajima, H. Kazeoka, T. Yogo & H. Iwahara, *Solid State Ionics*, 1991, **47**, 271
[31] H. Iwahara, *Solid State Ionics*, 1996, **86-88**, 9
[32] N. Tanigichi, K. Hatoh, J. Niikura, T. Gamo & H. Iwahara, *Solid State Ionics*, 1992, **53-57**, 998
[33] H. Iwahara, T. Yajima, T. Hibino & H. Ushida, *J. Electrochem. Soc.* 1993, **140**, 1687
[34] K. D. Kreuer, E. Schonherr & J. Maier, *Solid State Ionics*, 1994, **70/71**, 278
[35] A. S. Nowick & Yang Du, *Solid State Ionics*, 1995, **77**, 137
[36] T. Schober, W. Schilling & H. Wenzl, *Solid State Ionics*, 1996, **86-88**, 653
[37] H. Iwahara, in Solid State Ionics Materials, eds. V. B. R. Chowdari et al. (World Scientific, Singapore 1994) 79.
[38] H. Iwahara & T. Hibino, Proceedings on Symposium on Chemical Sensors II, edited by M. Butler, 1993, **7**, 464
[39] H. Iwahara, H. Uchida & S. Tanaka, *Solid State Ionics*, 1983, **9/10**, 1021
[40] N. Bonanos, K. S. Knight & B. Ellis, *Solid State Ionics*, 1995, **79**, 161
[41] N. Bonanos, Proceedings on Symposium on Materials Science, edited by F. W. Poulsen et al., Risø, Denmark, 1993, 19
[42] T. Scherban, R. Villeneuve, L. Abello & G. Lucazeau, Solid State Comms. 1992, **84** [3], 341
[43] J. Ranlov & K. Nielsen, *J. Mater. Chem*, 1994, **4** (6), 867
[44] R. D. Shannon, *Acta Crystallogr.*, 1976, **A32**, 751
[45] J. Ranlov, B. Lebech & K. Nielsen, *J. Mater. Chem*, 1995, **5** (5), 743

[46] K. S. Knight & N. Bonanos, *Mat. Res. Bull.*, 1995, **30** [3], 347
[47] H. Arnold, *International Tables for Crystallography*, ed. T. Hahn, Vol. A, Space Group Symmetry, Kluwer, Dordrecht, 1992
[48] T. Ishigaki, S. Yamauchi, K. Fueki & H. Iwahara, *Solid State Ionics*, 1986, **21**, 239
[49] H. Uchida, H. Yoshikawa & H. Iwahara, *Solid State Ionics*, 1989, **35**, 229
[50] H. Iwahara, *Solid State Ionics*, 1992, **52**, 99
[51] T. Schober, F. Krug & W. Schilling, *Solid State Ionics*, 1997, **97**, 369
[52] T. Yajima, H. Iwahara, H. Uchida & K. Koide, *Solid State Ionics*, 1990, **40/41**, 914
[53] H. Iwahara, H. Uchida, K. Ogaki & H. Nagato, *J. Electrochem. Soc.* 1991, **138**, 295
[54] H. Iwahara & H. Uchida, Proc. Int. Conf. On Chemical Sensors, Fukuoka, 1983, 227
[55] T. Scherban, W. K. Lee & A. S. Nowick, *Solid State Ionics*, 1985, **14**, 295

Chapter Three

Experimental Methods for ABO_3 Perovskite Oxide Ion Conductors

3.1 Introduction

Outlined in this chapter are the chemicals used, the method of preparation of the perovskite-based materials studied, and the spectroscopic techniques used to analyse materials with oxide ion conduction properties.

3.2 Preparation Techniques and Apparatus for Oxide Ion Perovskites

3.2.1 Materials

The chemicals used as starting materials, their manufacturers, and their purities are summarised in Table 3.1.

All other reagents and solvents used were analytical grade, unless otherwise stated.

3.2.2 Furnaces

Unsintered, 'green' ceramics were calcined and fired using a Ceramic Engineering HT05/18 furnace with 4 super Kanthal 1900 molybdenum disilicide resistance heating elements and Eurotherm 902 programmable controller with a Pt 20 %Rh vs Pt 40 %Rh thermocouple. All samples were calcined to a maximum temperature of 1450 °C.

Table 3.1 Chemicals used for powder synthesis, their manufacturers and purities.

Chemical	Manufacturer	Purity
Ga_2O_3	Aldrich	99.99+ %
Cr_2O_3	BDH	99 %
La_2O_3	Aldrich	99.9 %
MgO	Analar	99.6 %
$La(NO_3)_3.6H_2O$	Rectapur	99. 9%
$Cr(NO_3)_3.9H_2O$	Unilab	99 % (min)
$Fe(NO_3)_3.9H_2O$	Riedel-dettaën	99.5 % (min)
$Sr(NO_3)_2$	Riedel-dettaën	99 %
$Mg(NO_3)_2.6H_2O$	Riedel-dettaën	99.5 %
$Gd(NO_3)_3.6H_2O$	Aldrich	99.9 %

Temperature calibration of the furnaces, and determination of the temperature near the samples, was obtained using an exterior thermocouple linked to a HP 34410A multimeter.

3.2.3 Mixing and Milling

Mixing of the perovskite materials, prior to compaction and firing, was performed in a ball mill using 10 mm diameter yttria partially stabilised zirconia (PSZ) balls as the milling media, within polyethylene containers. The solvents used for wet milling were 95% ethanol for solid state powders, and isopropyl alcohol for powders prepared using a reverse strike co-precipitation technique, see Table 3.2. A milling duration of 8 hours was chosen to ensure thorough mixing.

3.2.4 Sample Preparation

Ga_2O_3 is only slightly soluble in hot nitric acid[1], therefore, the $LaGaO_3$-based materials were prepared by the solid state synthesis route as described in Section 3.2.4(a). The $LaFeO_3$ and $LaGdO_3$ based materials were prepared by reverse strike

co-precipitation, as described in Section 3.2.4(b). Table 3.2 shows all materials prepared, and their preparation routes; in all cases, x and y = 0.05, 0.1, 0.15 and 0.2.

Table 3.2 List of all oxide ion perovskite materials prepared; base materials used and synthesis technique employed.

Sample	Code	Materials used	Preparation Method
$LaGaO_3$	LGO	La_2O_3, Ga_2O_3	Solid State route
$LaGa_{1-x}Mg_xO_3$	LGM_x	La_2O_3, Ga_2O_3, MgO	Solid State route
$LaGa_{1-x}Cr_xO_3$	LGC_x	La_2O_3, Ga_2O_3, Cr_2O_3	Solid State route
$La_{1-x}Sr_xGaO_3$	LS_xG	La_2O_3, Ga_2O_3, $Sr(NO_3)_2$	Solid State route
$LaGdO_3$	LGDO	$Gd(NO_3)_3.6H_2O$, $La(NO_3)_3.6H_2O$	Reverse Strike
$LaGd_{1-x}Cr_xO_3$	$LGDC_x$	$La(NO_3)_3.6H_2O$, $Gd(NO_3)_3.6H_2O$, $Cr(NO_3)_3.9H_2O$	Reverse Strike co-precipitation
$LaFeO_3$	LFO	$La(NO_3)_3.6H_2O$, $Fe(NO_3)_3.9H_2O$	Reverse Strike co-precipitation
$LaFe_{1-x}Mg_xO_3$	LFM_x	$La(NO_3)_3.6H_2O$, $Fe(NO_3)_3.9H_2O$, $Mg(NO_3)_2.6H_2O$	Reverse Strike co-precipitation

3.2.4.1 Solid State Preparation Method

This method is the most common synthesis route for producing ceramics[2]. In order to prepare the ceramics listed in Table 3.2 using the solid state route, stoichiometric proportions of lanthanum oxide and gallium oxide (and A and B site dopants, oxides of Mg and Sr, as listed in Table 3.2) were weighed out, followed by thorough wet-mixing for 8 hours, using PSZ balls and 95 % ethanol in a ball mill. The powder was then dried at 50 °C for 8 hours and pressed into pellets of 15 mm diameter using an uniaxial press at 25 MPa. The pellets were then placed in a Pt foil lined alumina boat, covered and sintered as described in Section 3.2.5 for 6 hours. The resulting samples were then tested for phase composition using X-ray diffraction and Raman spectroscopy, as described in Section 3.3.

3.2.4.2 Reverse strike coprecipitation

In order to achieve the requirements of a fully dense ceramic, the ceramic powder should usually have the following characteristics[3]:

1) a precisely controlled, reproducible chemical composition including dopants;
2) chemical homogeneity on an atomic scale; and
3) a precisely controlled and consistent submicron particle size and shape.

To achieve these goals, a number of techniques are available[2,4-8], but research has shown that coprecipitation techniques have been widely used for preparing submicron-size high-purity oxide powders[9]. 'Reverse strike' coprecipitation involves a solution of cations being dripped into a precipitant (oxalic acid), which produces an intimately mixed oxalate precursor which is then decomposed into the oxide. Because of the formation of the oxalate precursor, the 'reverse strike' method produces an oxide powder with fine particle size, soft agglomerates and homogeneity of the dopant and matrix oxide mixture[10,11].

In order to prepare the ceramics listed in Table 3.2 by 'reverse strike' coprecipitation, the correct stoichiometric proportions of the materials, as listed in Table 3.2, were weighed and dissolved together in singly distilled water and stirred for 20 minutes, to form an aqueous solution with a concentration in excess of approximately 1 M. The precipitation procedure is similar to that of Van herle, et al.[8]. An aqueous oxalic acid solution, with a concentration of 0.05 M, was used as the standard precipitant. The precipitation solution was adjusted to a pH range of 6.7-6.9 and kept constant during the precipitation process by the addition of dilute ammonia solution. The precipitation was carried out by adding the mixture of the nitrates, drop-wise, into the precipitant, which was stirred at 750 rpm. The precipitate gel was then filtered and washed using distilled water (x5), followed by ethanol washing (x5). After being dried overnight at 50 °C, the precipitate was then calcined at 700 °C for 1 hour with a heating rate of 0.5 °C /min. The calcined precipitate was then reground using PSZ balls and 95% ethanol in a ballmill, dried at 50 °C for 8 hours and then checked for complete calcination of the starting material

using powder X-ray diffraction. The powder was then pressed into pellets of 15 mm diameter using an uniaxial press at 25 MPa. The pellets were then placed in a Pt foil lined alumina boat, covered and sintered as described in Section 3.2.5 for 6 hours. The resulting samples were then tested for phase composition using X-ray diffraction and Raman spectroscopy.

3.2.5 Sintering

A range of sintering temperatures of 1350, 1400, and 1450 °C was chosen to examine the effect of sintering temperature on the overall structure and composition of the material. Heating rates of 1.5 °C/min were employed on both heating and cooling to reduce thermal stress. All samples were held at the sinter temperature for 6 hours.

3.2.6 Surface Preparation

The surfaces of all the $LaGdO_3$ and $LaGaO_3$ (as shown in Table 3.2) based samples were hand-ground to a dull polished surface using SiC grinding papers with a grid order of 500#, 1000# and 4000# in order to prepare them for Raman Spectroscopy.

3.3 Spectroscopic Analysis

3.3.1 Powder X-ray Diffraction

Powder diffraction (XRD) was performed using a Philips X'Pert System with Cu Kα-radiation using a scanning rate of 0.02 °/s, averaging 2 seconds per increment. X-ray pattern analysis, α_2 elimination, smoothing and background subtraction were performed using the Philips X'Pert software package run on an IBM compatible computer. Samples were scanned as finely ground powders pressed into glass holders with dimensions of ca. 1x10x15 mm.

3.3.2 Raman Spectroscopy

Raman spectroscopy was performed on the $LaGaO_3$ and $LaGdO_3$ based samples listed in Table 3.2 to determine phase structure and purity, using a Spex 1403 0.84 m double beam pass spectrometer equipped with a Spectra physic model 164 argon-ion laser, a Spectra Physics HeNe laser model 207B, and a water cooled Hammamatsu R943-02 photomultiplier tube (PMT). Unless otherwise stated, the spectra were recorded at 5 cm^{-1} resolution, using the 514.5 nm laser line and output power of 100-200 mW, with incident power at approximately 50 mW. The scanning rate used to collect the spectra was kept at 0.5 $cm^{-1}s^{-1}$. The spectrometer was interfaced to a DM1B computer to provide for spectrometer control as well as multiple scanning and data manipulation.

Low temperature Raman spectroscopy of the $LaFeO_3$ sample was undertaken using a double beam pass Jobin Yvon U-1000 Raman spectrometer, equipped with a microscope stage for analysing small samples with 180° incident geometry. A Spectra Physics argon-ion laser was employed to excite laser Raman spectra using the 514.5 nm laser line and 25-50 mW power, along with 500 μm slits width. A LINKAM TMS-91 temperature stage attached to the microscope coupled with a CS196 cooling system and thermal monitor, was used to cool samples to -195 °C, using liquid nitrogen. Spectra were obtained using an uncoated Olympus x20 objective lens and a scanning rate of 0.5 $cm^{-1}s^{-1}$ over a range of 25-1000 cm^{-1}.

3.4 References

[1] The Merck Index, 12th Edition, 1996, Merck & Co. Inc, Rahway, N. J. U.S.A

[2] Y. I. Chen, M. Qi, D. Z. Yang & K. H. Wu. *Mater. Sci. Tech.*, 1994, **9**, 183.

[3] R. W. Davidge, *Mechanical Behaviour of Ceramics*, Cambridge University Press, 1979.

[4] C. C. Chen, M. M. Narsrallah and H. U Anderson, *J. Electrochem. Soc.*, 1993, **140**, [12], 3555.

[5] Y. Zhou, R. J. Phillips and J. A. Switzer, *J. Am. Ceram. Soc.*, 1995, **78**, [4], 981

[6] C. W. Tanner, A. V. Virkar, J. Am. Ceram. Soc., 1994, **77**, 8, 2209

[7] M. R. De Guire, M. J. Shingler and E. Dincer, *Solid State Ionics*, 1992, **52**, 155

[8] J. Van herle, T. Horita, T. Kawada, N. Sakai, H. Yokokawa & M. Dokiya. In Solid Oxide Fuel Cells IV, Edited by M. Dokiya, O. Yamamoto, H. Tagawa & S. C. Singhal, *J. Electrochem. Soc.* 1995, 1082.

[9] J. S. Reeds, *Introduction to the principles of Ceramic Processing*, John Wiley & Sons, New York, 1987.

[10] I. Riess, D. Braunshtein & J. Tannhauser, *J. Am. Ceram. Soc.*, 1982, **64**, 479

[11] P. Duran, C. Moure & J. R. Jurade, *J. Mat. Sci.*, 1994, **29**, 1940

Chapter Four

Experimental Methods for ABO_3 Perovskite Protonic Conductors

4.1 Introduction

Outlined in this chapter are the samples studied and the electrical and spectroscopic techniques used to analyse materials with proton conducting properties.

4.2 Apparatus

4.2.1 Materials

The materials studied were $SrCeO_3$ based proton conductor perovskites[1,2] and consisted of $SrCe_{1-x}Y_xO_{3-\delta}$ where x = 0.025, 0.05, 0.075, 0.1, 0.15 and 0.2 and the sub-stoichiometric material $Sr_{0.995}Ce_{0.95}Y_{0.05}O_{3-\delta}$. The values of x were chosen to represent the range over which doping has the most effect on increasing the defect concentration (being 0-20% dopant) without adversely affecting the overall stoichiometry, i.e., causing any second phase development by exceeding the upper limit of solid solution formation[3]. Increasing defect concentration may cause increased conductivity, as explained in Chapters 1 (Section 1.5.2) and 2 (Section 2.6.3), a desired outcome for this work. All samples were processed using a solid state reaction. The reagents, $SrCO_3$, CeO_2 and Y_2O_3 were dried for 20 h. at 150 °C and mixed in an agate ball mill. The calcination reaction was carried out in two steps, 1000 °C and 1300 °C with agate ball milling of 30 minutes and 1 hour respectively between each calcination step. Dispersant (0.5g PVP dissolved in 1 g ethanol per 100g powder) was mixed into the powder, followed by ten minutes high

speed ball milling and the samples were then formed into pellets of 10 mm diameter and approximately 2 mm thickness. Samples were then sintered as described in Table 4.1.

The surfaces of all the pellets were ground to a dull polished surface using SiC grinding papers with a grid order of 1000# and 4000# by hand. Pellets were then coated with platinum paste (Demetron Einbrennplatin 308A) and heated at 3 °C/min to 1125 °C for 2 hours

Table 4.1. Sinter temperatures (°C) and sinter times (h) of $SrCeO_3$ based samples studied

Sample	Sinter Temperature (°C)	Sinter Time (h)
$SrCe_{0.975}Y_{0.025}O_{3-\delta}$	1450	12
$SrCe_{0.95}Y_{0.05}O_{3-\delta}$	1450	12
$Sr_{0.995}Ce_{0.95}Y_{0.05}O_{3-\delta}$	1550	11
$SrCe_{0.925}Y_{0.075}O_{3-\delta}$	1500	11
$SrCe_{0.9}Y_{0.1}O_{3-\delta}$	1500	10
$SrCe_{0.85}Y_{0.15}O_{3-\delta}$	1500	10
$SrCe_{0.8}Y_{0.2}O_{3-\delta}$	1500	10

4.2.2 X-Ray Diffraction

X-ray powder diffraction was performed at room temperature on a STOE theta-theta reflection diffractometer equipped with a Peltier cooled Kevex energy dispersive detector; Cu K_α - radiation was used. The powdered samples were mixed with Si-standard. Unit cell dimensions were determined by the least squares method included in the Visual-X^{Pow} Stoe software, which also allowed for adjustment of a zero-shift in 2 theta (typically below 0.02 degrees). X-ray diffraction was used to confirm that the materials were single phase and also used to calculate the lattice constants of the materials.

4.2.3 Experimental Apparatus for P_{H_2O}/P_{O_2} Dependence Studies

Electrical conductivity was determined as a function of P_{O_2} at 600 and 800 °C in two different atmospheres (0.01 and 0.001 atm P_{H_2O}) for each of the samples shown in Table 4.1. A P_{O_2} range of 1 atm. (pure O_2) to approximately $1x10^{-25}$ atm. (N_2/H_2 mix) allowed for the separation of *n*-(electron), *p*-(hole) and *i*-(ionic) type conductivities. Figure 4.2 shows a schematic of the specific apparatus used in the P_{H_2O}/P_{O_2} dependence studies. The entire testing system could be controlled from a single computer and this allowed for the semi-automation of the testing regime.

Computer control of the partial pressure of oxygen (P_{O_2}), partial pressure of water (P_{H_2O}), temperature and gas flow were all monitored and controlled by an IBM compatible 386 computer. P_{O_2} levels were adjusted by changing the ratio of gases. The gases utilised in the experiment were mixes of O_2/N_2, Air/N_2 and forming gas ($8\%H_2$ in N_2)/N_2. P_{H_2O} levels were set by passing the pre-mixed gas through a bubbler contained in a 30 L-refrigerator set at a constant 11 °C. As illustrated in Figure 4.1, passing 100% of the pre-mixed gas through the bubbler gave a P_{H_2O} value of 0.01 atm. Passing only 10% of the total pre-mixed gas through the bubbler gave a P_{H_2O} value of 0.001 atm.

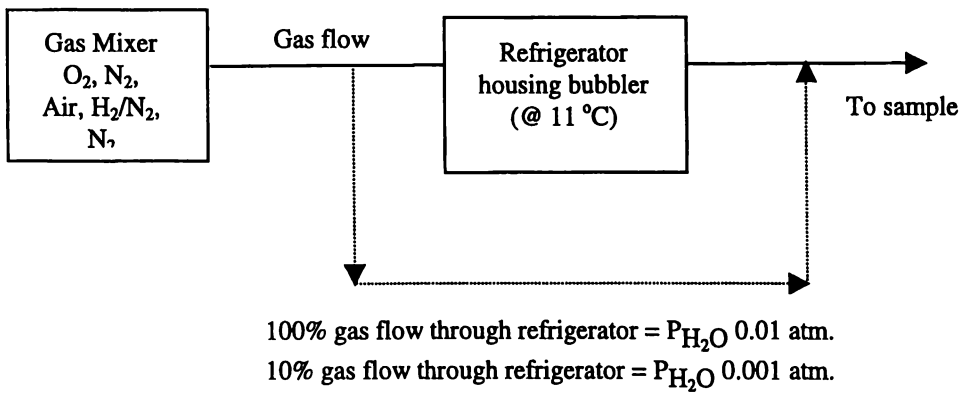

Figure 4.1. Diagram of mixing of total gas flow in order to create two different partial pressures of water. 10% of the gas directed through the refrigerator and 90% of the gas kept at room temperature gives a P_{H_2O} of 0.001 atm. 100% of the gas flowing through the refrigerator gives a P_{H_2O} of 0.01 atm.

Temperature settings were automatically set by the computer, and measurements were taken automatically by the computer at specified times. Impedence measurements were then performed at each new P_{O_2} level after equilibration time, and the results stored as a separate file in the computer. Each sample took approximately 4-5 days to complete the range of variables, as set out in Table 4.2.

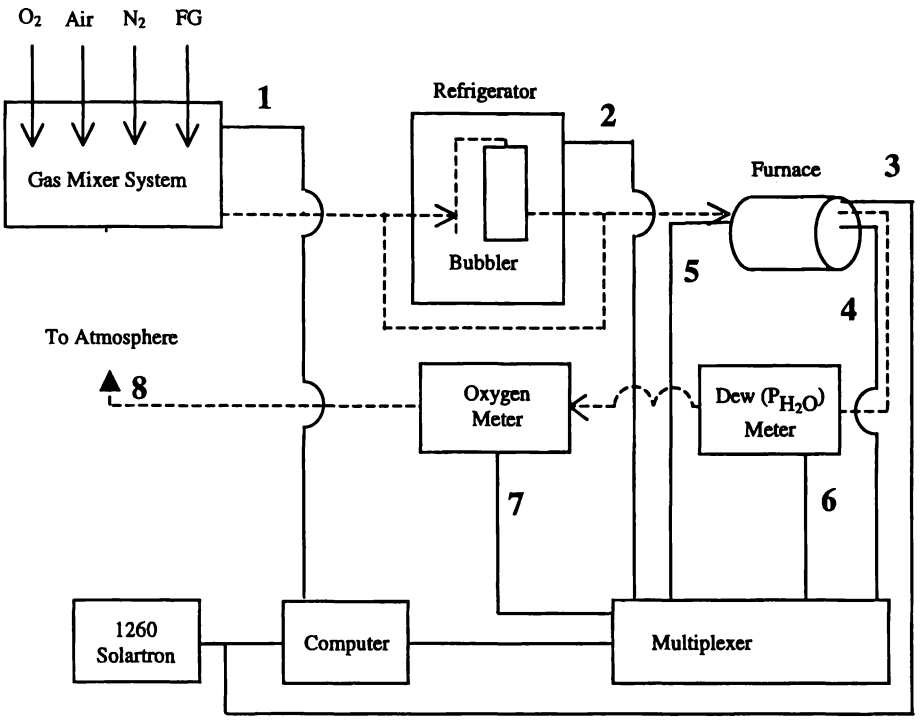

Figure 4.2. Schematic of overall P_{H_2O}/P_{O_2} testing apparatus where:

1 Computer control of Mass flow controllers for automated gas mixing
2 Temperature thermocouple to refrigerator (constant 11 °C)
3 AC Impedance cables connected to sample in furnace
4 Temperature thermocouple situated at sample in testing rig
5 Temperature thermocouple situated in furnace outside testing rig
6 P_{H_2O} 'Dew' meter readings in % atmospheres
7 P_{O_2} readings recorded in mV.
8 Gas flow (Total 100 mL/min.) exhaust to extractor,

and the gas mixer system contains mass flow controllers to mix O_2/N_2, Air/N_2 and forming gas/N_2. The refrigerator contains a 200 mL bubbler at constant temperature of 11 °C. The furnace contains sample holder and gas tight system connected to AC impedance analyser and temperature controller. The dashed line represents the flow of gas through from the gas mixer to the sample and then out to the extraction system after testing.

Table 4.2. Testing parameters for each $SrCeO_3$ based sample (as shown in Table 4.1).

Samples (as per Table 4.1)	Temp (°C)	P_{H_2O} (atm)	mL O_2/100 mL total flow	mL Forming Gas (8%H_2 in N_2)/100 mL total flow	Total no. of files/sample
7	600, 800	0.01, 0.001	100, 65, 35, 10, 5, 1.05, 0.42 & 0.21	100, 80, 50, 20, 5, 2, 1 & <1	64

4.2.3.1 Computer Control

The computer program, FCL[4], was used to control the overall experimental setup, as shown in Figure 4.2. The computer accessed a multiplexer (3421A Data acquisition/control unit by Hewlett Packard) containing a number of channels which could access each piece of equipment separately. The system automated measurement readings from the P_{H_2O} meter, P_{O_2} meter and controls gas flow and overall control of the *Solartron 1260* AC Impedence/Gain Phase analyser.

4.2.3.2 Gas Control

Brooks mass flow controllers (5850TR series) with the range of 100, 50 and 10 mL/min were used. These were computer controlled by the FCL program and flow rates could be automatically monitored and changed throughout the experiment. Table 4.3 shows the mixing ratio of gases to achieve each P_{O_2} level. As P_{O_2} is temperature dependent (see equation 2.12) the gas mixing ratio was maintained for each sample at both temperatures, but the range of achievable P_{O_2} is less for the lower temperatures.

Table 4.3. Gas Mixing ratios, mixing O_2/N_2, Air/N_2 and 8%H_2 in N_2/N_2.

mL O_2/100 mL total	mL air/100 mL total	mL N_2/100 mL total	mL (H_2/N_2)/100 mL total
100			
65		35	
35		65	
10		90	
5		95	
	5	95	
	2	98	
	1	99	
		100	
		99	1
		98	2
		95	5
		80	20
		50	50
		20	80
			100

4.2.3.3 Conductivity Apparatus

The conductivity rig design used, utilised a pseudo 4-point terminal system (a 4-wire, 2-electrode measurement system) to minimise the resistance due to wires, and could be run up to 1000 °C. The data presented, therefore, excludes the lead resistance, but includes the electrode contact resistance. Figure 4.3 shows the conductivity rig setup. The AC impedence analyser was a *Solartron 1260* AC Impedence/Gain Phase analyser. Conductivity measurements were undertaken in the frequency range of 0.1 Hz to 1 MHz and all analyser settings are listed in Appendix 2.

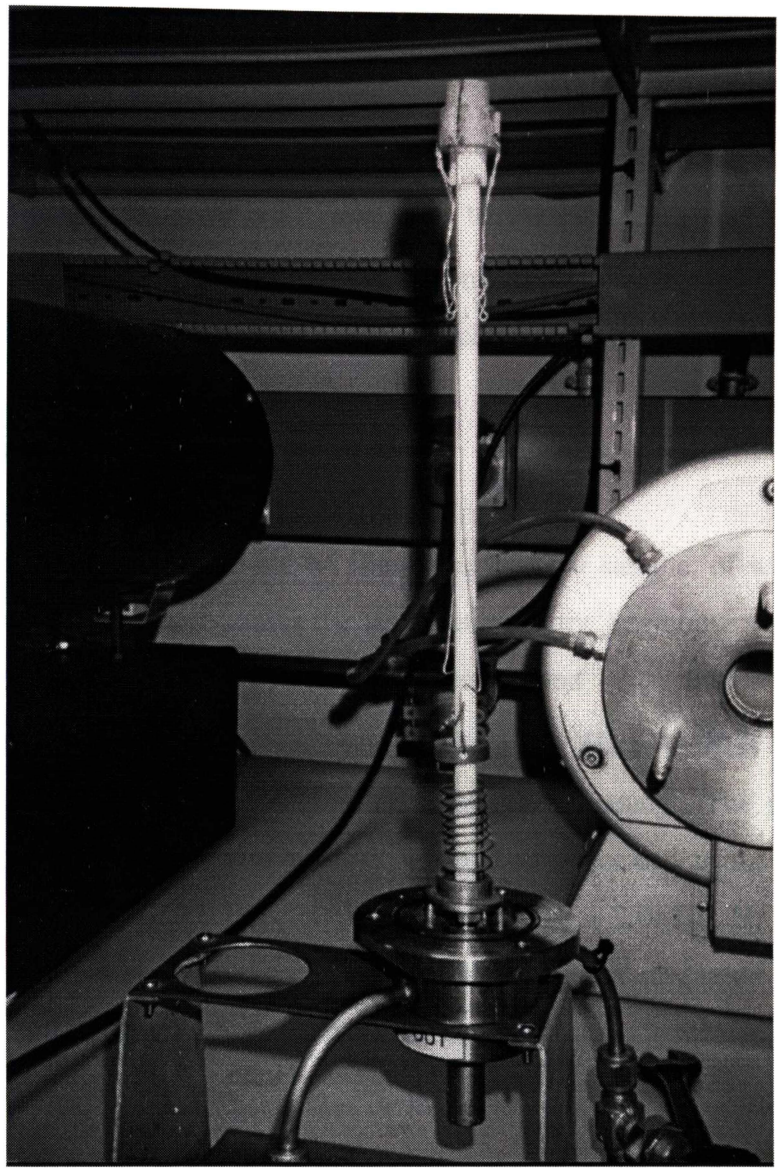

Figure 4.3. Photograph showing sample holder and electrodes of the conductivity rig.

4.2.3.4 P_{H_2O} Meter

The P_{H_2O} meter was a *MCM Dewluxe* Moisture Control – Measurement unit measuring –40 to +20 dewpoints (1 to $1x10^{-6}$ atm. P_{H_2O}). FCL recorded these values in percent P_{H_2O}. The level of moisture carried in the gas was controlled by directing the pre-mixed gas through a bubbler kept in a refrigerator (30 L) at a constant temperature of 11 °C. As two levels of P_{H_2O} were required (0.01 and 0.001 atm. P_{H_2O}) either 100% of the pre-mixed gas, or 10% of the pre-mixed gas was passed through the bubbler, as explained in Section 4.2.2.

4.2.3.5 P_{O_2} Meter

A potentiometric oxygen gauge[5] was used to measure P_{O_2}, which operated at 1000 °C using a 8 mol% fully stabilised zirconia (FSZ) electrolyte. The output, in mV, was recorded by the FCL program onto each conductivity measurement file.

4.2.4 Impedence Measurements

As shown in Table 4.2, there are 64 files generated per sample, of which there are seven samples. Each file contains the temperature at the beginning and end of each AC impedence sweep, a P_{H_2O} value (in percent) and P_{O_2} value (in mV). Also contained in the file are 40 frequency values from 0.1 Hz to 1 MHz with a real (x coordinate) and imaginary value (y coordinate) per frequency. The plot generated from this information is called a bode plot and is generated using the computer program, Equivcrt[6]. By subtracting the inductance ($L = 2.0 \times 10^{-7}$ H) caused by the apparatus, the resultant curves could be fitted to an equivalent circuit (for example, an R(RQ) fit) (see Chapter 5, Section 5.5.1), and each curve generated would have a set of values.

When an AC impedence sweep is generated at lower temperatures, it is possible to resolve a number of curves, which represent bulk, grain boundary and electrode impedance as shown in Figure 4.4.

At higher temperatures these curves are less easily resolved, but bulk resistance can still be recorded. It is that value which is recorded in order to analyse the effect of changing P_{O_2} and P_{H_2O} on total conductivity.

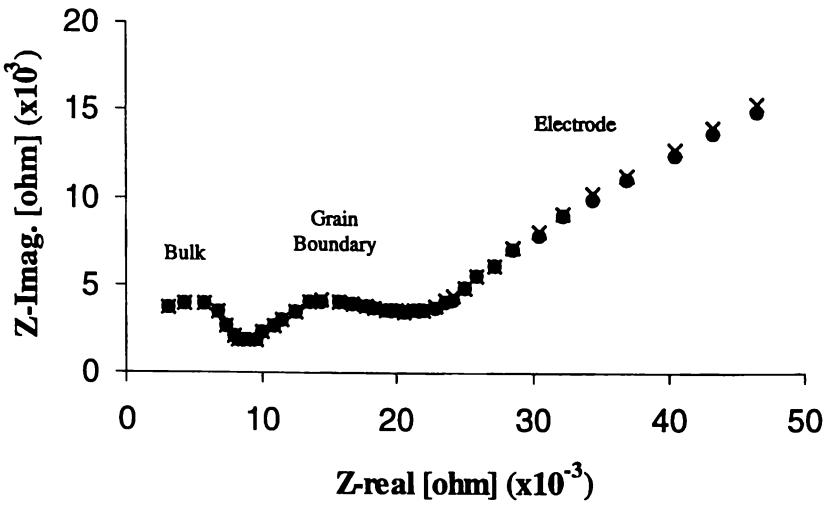

Figure 4.4. Nyquist diagram showing real and fitted data for a $SrCeO_3$ based sample at 200 °C. (x = fitted data, ♦ = actual data points, ie, fit very close to actual)

4.2.4.1 Analysis

Once all curves have been fitted and resolved to give the bulk resistance, analysis of these results was undertaken using SigmaPlot computer program. Each AC impedance sweep generated one resistance point and three variables (Temperature, P_{O_2} and P_{H_2O}). Each resistance value was converted to conductivity using the dimensions of the pellet, as explained in Chapter 5, using equation 5.7. The conductivity was then corrected (σ_r) for the relative density of each sample according to the linear relationship 4.1, as established in previous work[1].

$$\sigma_r = \sigma_1\{1-3(1-d)\} \qquad (4.1)$$

Where σ_1 is the conductivity of a 100% dense pellet and d is the ratio of measured to theoretical density. The latter was calculated from the formula weight, the number of formulae in a unit cell and the unit cell volume as measured by X-ray diffraction, see Chapter 5, equation 5.5. The conductivity at 100% density was determined by solving equation 4.1 for σ_1.

Temperature was converted to Kelvin, P_{O_2} to Log of P_{O_2} atm. (see Appendix 3, P_{O_2} transform) and P_{H_2O} to atm. Plots of Log P_{O_2} versus conductivity were generated

for each sample at each temperature and P_{H_2O} setting, therefore giving 4 graphs per sample. From that graph, a curve fit was generated (see Appendix 3, curve fit transform) that allowed for the resolution of *p*, *n*, and *i* values. Using equation 2.7, dependencies were kept constant at +¼ and –¼. Resolution of the total conductivity down to its constituent elements meant that the effect on conductivity with changing dopant concentration could be studied.

4.3 References

[1] E. O. Ahlgren, J. R. Hansen, N. Bonanos, F. W. Poulsen & M. Mogensen, Proc. *17th Risø International Symposium on Materials Science*. Editors, F. W. Poulsen, N. Bonanos, S. Lindertoth, M. Mogensen & B. Zachau-Christiansen. 1996.

[2] H. Iwahara, T. Esaka, H. Uchida & N. Maeda, *Solid State Ionics*, 1981, **3/4**, 359

[3] H. Iwahara, *Solid State Ionics*, 1996, **86-88**, 9

[4] FCL Electrochemical Control Program, V 3.1, 1990-1992 by B. Malmgren-Hansen at Risø National Laboratory, Denmark.

[5] Designed at Risø National Laboratory, Denmark.

[6] Equivalent Circuit, Version 4.55, July 1996, by B. A. Boukamp, Copyright UT 85-96.

Chapter Five

Theory of Techniques

5.1 Introduction

Outlined in this chapter is the theory relating to the electrical and spectroscopic techniques used to analyse the perovskite materials prepared, both oxide ion and proton conductors, as outlined in Chapters 3 and 4. Also outlined in this chapter is the theory related to calculations made in order to study the density and unit cell volumes of the materials studies, for both oxide ion and protonic conductors.

5.2 Laser Raman Spectroscopy

5.2.1.1 The Raman Effect

The theory of the Raman effect and practical use of the technique has been discussed by various workers including Long[1], Nakamoto[2], and Gardiner and Graves[3]. Normal light scattering (or non-Raman scattering) involves an elastic process, whereby there is no loss or gain in energy of photons scattered by the matter of the sample it is incident on. This type of scattering is called Rayleigh scattering. In contrast, the Raman effect is associated with inelastic scattering of light by matter. Figure 5.1 shows a schematic of Raman Stokes, anti-Stokes and Rayleigh transitions from quantum Raman theory. There are three states involved in the process: (1) When an incident photon of frequency ν_0 collides with a molecule in an initial vibrational state (with energy E_m), the molecule is instantly excited into state (2), an unstable, short lived intermediate level, which then returns to state (3) a final, stable vibrational state (with energy E_n) by emitting a scattered photon of a characteristic

frequency ($\nu_o \pm \nu$). Both the initial (1) and final (2) vibrational levels are associated with the electronic ground state. The scattered frequencies ($\nu_o - \nu$) and ($\nu_o + \nu$) correspond to the Raman Stokes and anti-Stokes transitions respectively. Typically, the Raman band frequencies are stated in units of wavenumber (cm^{-1}) for convenience. The Stokes transitions derive from the ground vibrational state, whereas the anti-Stokes transitions are excited from the higher vibrational level of the vibration concerned. Stokes lines have a greater intensity when compared to anti-Stokes lines. This is due to the higher vibrational energy levels having lower populations at any given temperature, according to Boltzmann statistics. Therefore, Stokes lines are typically preferred transitions studied in Raman spectroscopy due to the greater signal-to-noise ratio.

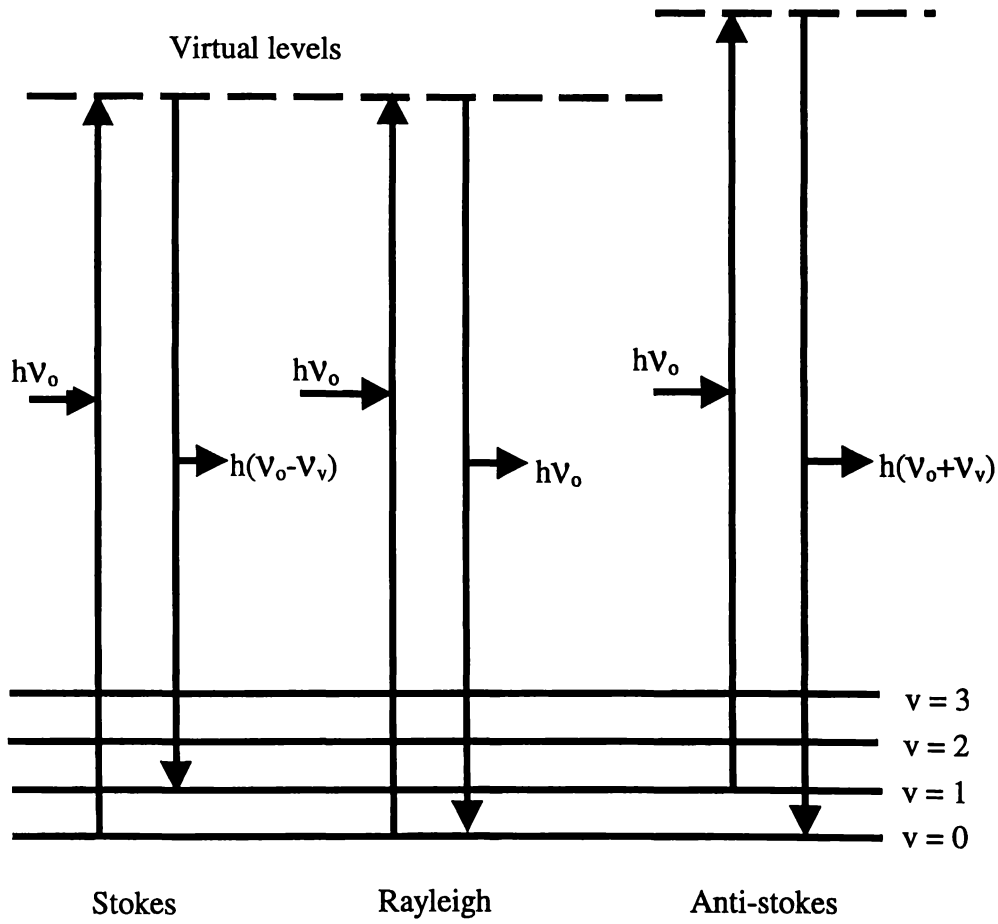

Figure 5.1 Raman Stokes, anti-Stokes and Rayleigh line. [Reproduced from Gardiner and Graves[3]].

Elastic Rayleigh scattering always accompanies Raman scattering. It should be noted that for normal Raman scattering to occur, the incident photon of energy ($h\nu_o$) must not match that required to excite an electronic transition, so that no absorption of the incident photon can occur.

5.2.1.2 Raman Selection Rules

The mathematical selection rules for Raman spectroscopy and expressions for the intensity of scattered radiation have been described in the literature[1-3], and are given below.

A molecular vibration will only be Raman active if it is associated with a change in the induced dipole moment (P), resulting from a change in the polarisability of the molecule[3]. Moreover, a vibrational transition of the molecule is allowed only if the induced dipole moment is non-zero, since the intensity of the transition is proportional to P^2. The Raman effect can be best understood in terms of the bond polarisation theory, which predicts that the total Raman intensity of a Stokes band scattered over the solid angle 4π, by one randomly orientated molecule, undergoing a transition from an initial ground state **m** to the final state **n,** is given by equation 5.1

$$I_{mn} = \frac{2^7 \pi^5}{3^2 c^4} I_o (\nu_o \pm \nu_{mn})^4 \sum_{ij} \left| (\alpha_{ij})_{mn} \right|^2 \qquad (5.1)$$

where, I_o = the intensity of the incident light,

ν_o = the exciting line frequency,

$(\nu_o \pm \nu_{mn})$ = the frequency of the scattered light,

$\pm$ = associated with the Stokes and anti-Stokes lines respectively,

c = the velocity of light,

i, j = x,y and z components in the space-fixed co-ordinate system,

(α_{ij}) = the ij-th element of the scattering tensor and has the general expression (taken as a summation over all vibronic states of the molecule) as shown in Equation 5.2

$$(\alpha_{ij})_{mn} = \sum_r \frac{1}{h}\left[\frac{(M_i)_{mr}(M_j)_{rn}}{(\nu_{rm} - \nu_o + i\Gamma_r)} + \frac{(M_j)_{mr}(M_i)_{rn}}{(\nu_{rm} + \nu_o + i\Gamma_r)}\right] \qquad (5.2)$$

where, **r** = the intermediate virtual state,

h = Planck's constant,

Γ_r = a damping constant which prevents the denominator becoming zero at resonance and related to the lifetime of the intermediate state,

ν_{rm} and ν_m = the frequencies corresponding to the differences between the states denoted by the subscripts and

$(M_i)_{mr}$, $(M_i)_{rn}$ = the direction i,j from the ground state, **m,n**, to the intermediate state **r**.

The band polarisability is almost independent of ν_o (the frequency of the excited line) where the excited photon frequency is very different from the first excited state of the molecule. The summation of equation 5.2 can be considered a constant, since small changes in ν_o will not greatly affect any other term. Under these circumstances, and at constant incident radiance, the Raman line intensity becomes proportional to $(\nu_o \pm \nu_i)^4$, the so-called ν^4 law of the Raman effect.

5.2.2 Raman Spectroscopy of Solid State Materials

Several texts describe the theory of Raman spectroscopy of crystalline solids[1,4].

The theory of Raman spectroscopy of solid crystalline samples can be related to that of a molecular crystal. Such a crystal can be viewed using the oriented gas model, in which the molecular entity has a relatively fixed orientation with respect to the crystal axis. The molecule retains its internal vibrations. However, the rotation and translation degrees of freedom of the free molecule are replaced by external vibrations, torsional motion of the molecule about its axes on the lattice (librations or rotational lattice modes), and restricted translational displacements within the lattice (translational lattice modes).

This relation is only an estimation, and Raman spectra of molecular crystals show distinct differences to those of the gas phase. Spectra of crystalline samples thus contain:

(i) many low-wavenumber bands due to external vibrations,
(ii) large changes in the shape and intensity of internal modes and
(iii) gas phase fundamental modes that can be split into additional bands.

This splitting of fundamental modes can be due to the symmetry of the site, which if lower than that of the molecule, may remove some or all of the degeneracy of the internal vibrations. Additionally, the spectra exhibit bands due to:

(i) interactions with internal vibrations of other molecules in the same unit cell,
(ii) coupling between internal and external modes and
(iii) in some cases, effects due to long-range electrostatic forces in the crystal.

This model holds for many systems, however cases exist where it does not, such as systems with no internal modes, for example network covalent crystals. In this case the dynamics of the lattice must be accounted for.

5.3 X-ray Diffraction

X-ray diffraction (XRD) is typically used to identify the crystalline phase and structure of the crystalline solid materials, including powders. The principle of XRD is based on the Bragg Law, where reflections will be obtained when equation 5.3 is satisfied[5].

$$n\lambda = 2d\sin\theta \qquad (5.3)$$

Where, θ = diffraction angle

d = the lattice spacing

n = an integer, the order of Bragg reflection

λ = x-radiation wavelength

In practice, varying one of the four quantities θ, d, n or λ will satisfy the Bragg law. Typically, the sample angle is varied and the diffraction intensity measured at the varied angle.

There are several steps to the identification of a phase and parameter calculation:

(i) record the diffraction pattern,

(ii) if results appear to show a mixed phase, then Kα- strip the results (using the feature in the Philips X'Pert software in the case of work undertaken in this thesis). Calculate the Miller indices (hkl) relating to the reflections, by relating the relative intensity of each peak to that of a structurally similar sample, in the case of $LaGdO_3$, which is a monoclinic material, B-Gd_2O_3 (JCPDS #42-1465) can be used.

(iii) enter *h*, *k*, and *l* values and d-spacing in Angstroms into the 'Unit Cell[8], computer program for refining unit cell parameters and gain parameters, error values and unit cell volume.

For crystallographic work it is desirable to use monochromatic X-rays. However, the output of an X-ray tube consists of white radiation plus a number of characteristic lines. Figure 5.2 shows the output of a copper tube, with the absorption curve of nickel superimposed on it. Note that the absorption edge of nickel (1.487 Å) is just longer than that of Cu Kβ_1 (1.392 Å). If Cu X-rays are passed through a thin foil of Ni, then the foil absorbs the radiation below dotted curve. Thus the foil removes the Kβ_1 peak plus a lot of white radiation, but transmits Kα_1 and Kα_2. The two Kα radiations are sufficiently close together to be effectively a single wavelength, and this is acceptable for many crystallographic applications[7], but when the a second phase is apparent, Kα –stripping must be carried out to ensure only relevant true peaks are indexed.

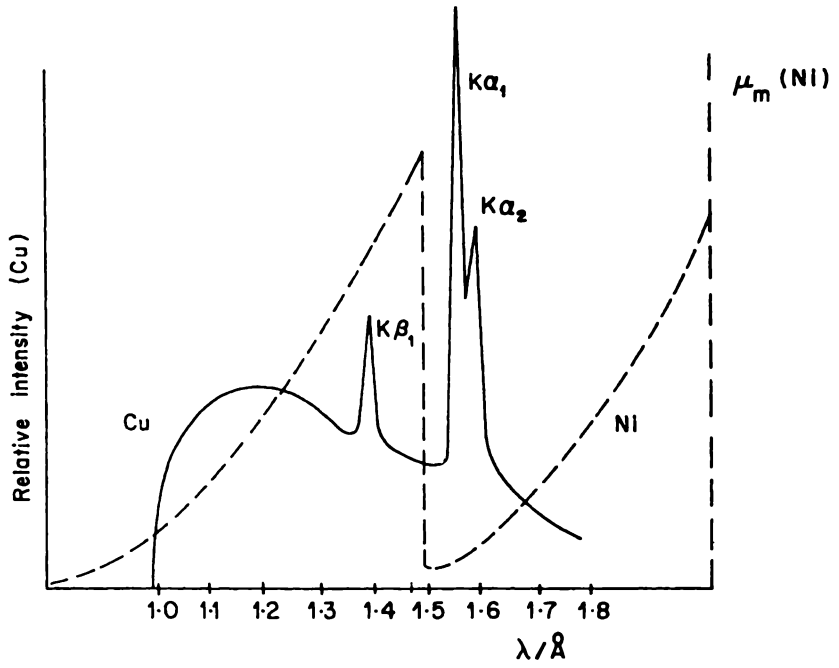

Figure 5.2. Output of Cu tube and absorption curve for Ni, reproduced from 'X-Ray methods, Analytical Chemistry by open learning[7]'.

If diffraction lines of different phases are clearly distinguished, semi-qualitative phase analysis to ca. 1% is possible[6].

5.4. Density Measurements

Density measurements of the sintered samples were obtained using the standard Achimedes technique[9]. In this method, the dry weight of a pelletised specimen is first recorded. The sample is then boiled in distilled water for ca. 15 min., followed by blot drying and weighing again; the open porosity of the sample having been filled with water. The pellet is then suspended in water and re-weighed. The bulk density (B) can then be calculated using equation 5.4:

$$B = \frac{W_d}{W_w - W_s} \qquad (5.4)$$

Where, W_d = dry weight of sample

W_w = wet weight of sample

W_s = weight of sample suspended in water

The theoretical (X-ray) density T_d can be calculated from equation 5.5.

$$T_d = \frac{\text{Cell - mass}}{\text{Cell - volume}} = \frac{ZM_c}{V_c N_A} \qquad (5.5)$$

Where, Z = number of chemical species in the unit cell

M_c = relative molar mass of the formula in the unit cell ($gmol^{-1}$)

V_c = unit cell volume ($Å^3$)

N_A = Avogadro's number (6.0221×10^{23} mol^{-1})

The cell parameters for both the oxide ion and protonic conductors were calculated using orthorhombic symmetry and Z = 4 for $GdFeO_3$ (JCPDS #15-0196) and a sample formula $AB_{1-x}N_xO_{3-x/2}$ was used, where N = dopant, ie, Y, Mg or Cr.

Theoretical densities (T_d) were calculated from XRD patterns using the d-spacings and a parameter calculation UNITCELL program[8] on a PC computer for the oxide ion based ceramics listed in Chapter 3, Table 3.2. Unit cell dimensions of the protonic conductors listed in Chapter 4, Table 4.1 were determined by the least squares method included in the Visual-X^{pow} Stoe software, which allowed for adjustment of a zero-shift in 2 theta (typically below 0.02 degrees).

With the theoretical (x-ray) density (T_d) (see Appendix 3, theoretical density calculations) and the density from Achimedes method (B), the percentage theoretical density ($\%\rho$) may be calculated using equation 5.6:

$$\%\rho = \frac{B}{T_d} \times 100\% \qquad (5.6)$$

5.5 Electrical Theory

Impedance spectroscopy (IS) is a relatively new and powerful method of characterising many of the electrical properties of materials and their interfaces with electronically conducting electrodes. It may be used to investigate the kinetics and mechanisms of many materials, both liquid and solid: ionic, semi-conducting, mixed ionic/electronic and dielectrics.

Electrical measurements to evaluate the electrochemical behaviour of electrode and/or electrolyte materials are usually made with cells having two identical electrodes applied to the faces of a sample in the form of a circular cylinder or rectangular parallelepiped.

One of the basic purposes of IS is to determine the properties of electrode/materials systems, their interrelations, and their dependencies on such controllable variables as temperature, oxygen partial pressure, applied hydrostatic pressure, and applied static voltage or current bias[10].

A multitude of fundamental processes take place throughout the cell when it is electrically stimulated and, in total, lead to the overall electrical response. They include the transport of electrons through the electronic conductors, the transfer of electrons at the electrode-electrolyte interfaces to or from charged or uncharged atomic species, which originate from the cell materials and its atmospheric environment (oxidation or reduction reactions). Also, the flow of charged atoms or atom agglomerates via defects in the electrolyte. The flow rate of charged particles (current) depends on the ohmic resistance of the electrodes and the electrolyte, and on the reaction rates at the electrode-electrolyte interfaces. The flow may be further impeded by band structure anomalies at any grain boundaries present (particularly if second phases are present in these regions) and by point defects in the bulk of all materials.

There are various methods to measure the conductivity of ceramics[11]. They include an ohmmeter or bridge, 3 or 4 probe DC (direct current), condenser discharge, pulse,

and AC impedence spectroscopy (AC Impedence). All of these are based on the principle of Ohm's Law. Modifying Ohms Law in terms of the reciprocal of the electrical resistance being resistivity (ρ), conductivity (σ) is defined as[11]:

$$\sigma = \frac{IL}{VA} \quad \text{or} \quad \sigma = \frac{\rho * L}{A} \tag{5.7}$$

Where A is the cross-sectional area in cm^2 (A = a.b), L is the length of the sample in cm, I is the current (in amperes) through the sample, and V is the voltage drop (in volts) across the sample, as illustrated in Figure 5.3.

The electrode, when run at the operating temperature in the cell environment, has a high degree of electrode polarisation and resistance compared to that of the sample and cannot be ignored. Using IS, the electrode resistance can easily be separated from the sample's resistance[12].

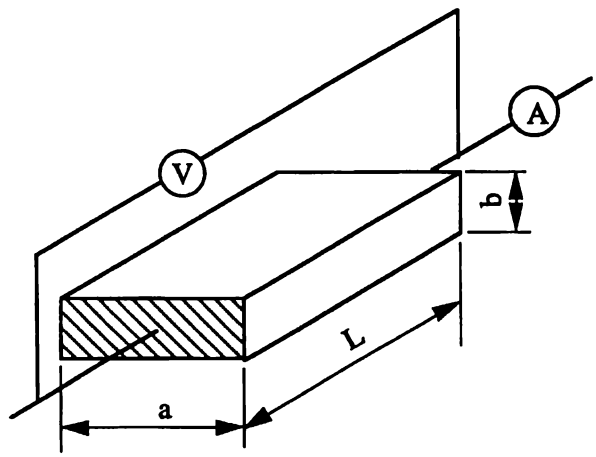

Figure 5.3. The schematic diagram of a conductivity measurement in relation to equation 5.7

Compared to other methods, IS does not necessarily require either the use of reversible electrodes or a more complicated cell, which eliminates the masking effect of electrode polarisation, such as with the 4-probe DC method. This advantage makes IS widely used in the electrical measurement of ceramics.

5.5.1 Impedance Spectroscopy (IS)

This technique involves the application of an alternating current (AC) of varying frequencies across the material, and comparing the input and output signals to get information about the phase shift observed, and the impedance modulus.

Assume that an electric signal, U, is applied across the sample. If the sample is a solid electrolyte, then two electrodes (usually, but not always, Pt) are placed on either side (the sample is usually in the form of a pellet of known dimensions) to form a cell, as illustrated in the photograph in Figure 4.3. The electric signal is given by:

$$U = U_o e^{i\omega t} \qquad (5.8)$$

where ω is the angular frequency, and t is the time constant; the resultant current passing through the cell is, thus,

$$I = I_o e^{i(\omega t + \phi)} \qquad (5.9)$$

where ϕ is the phase angle. The impedance of the cell (Z) is thus measured from

$$Z = \frac{U}{I} = \frac{U_o e^{-i\phi}}{I_o} = Z_o e^{-i\phi} \qquad (5.10)$$

Where Z_0, as shown in Figure 5.4, is the modulus of the impedance of the sample. This can then be plotted onto a Nyquist diagram (as shown in Figure 4.4), with the opposite of the imaginary component, $Z = -Z_o \sin\phi$, on the y-axis.

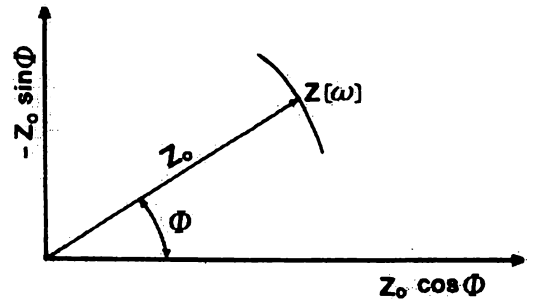

Figure 5.4 The general principles of impedance spectroscopy[13]

Now, each electrode or electrolyte process has a different time constant and therefore relaxes over a different frequency range. If the applied frequency range is large enough, then the contribution of each of the processes can be separated. In general, however, the time constant of each process decreases with increasing temperature and thus the response of the cell shifts to higher frequencies.

An impedance spectrum may consist of up to four semicircles, (or more, depending on the system) as shown in Figure 5.5, due to differences between impedance and the dielectric constant in the grain, grain boundary, electrode and the interface between the sample and electrode.

In Figure 5.5, R_b is the resistance of the grain (intragrain resistance), R_{gb} is the resistance of the grain boundary (including the blocking effect), R_t the total resistance of the pellet, R_{eh} the high-frequency component of the electrode resistance and R_{el} the low-frequency component of the electrode resistance.

The response in Figure 5.5 can be represented by a circuit as shown in Figure 5.6, and is similar in nature to that observed for a solid electrolyte material. The semicircle in Figure 5.5 is observed when a complex impedance plane is plotted, with the real impedance plotted on the x-axis, and the imaginary impedance plotted on the y-axis.

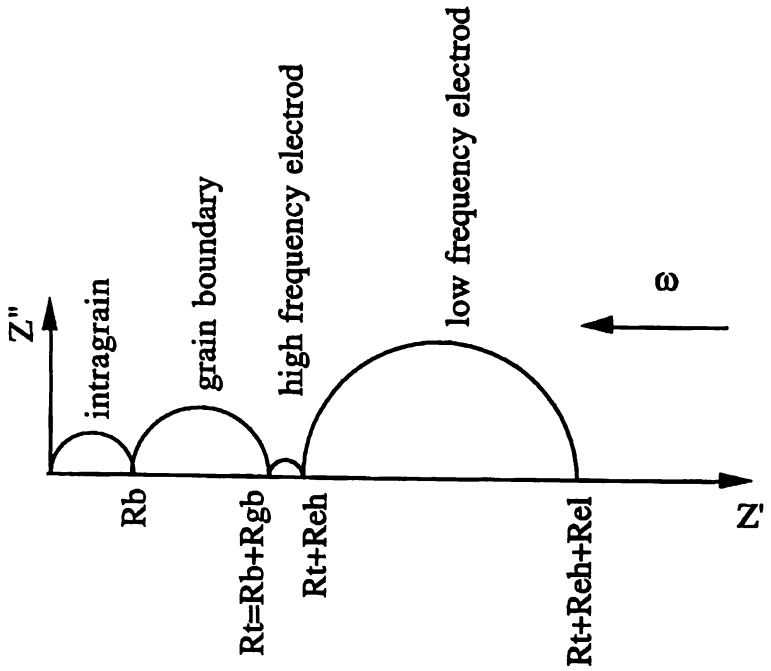

Figure 5.5. Complete Impedence Diagram of a symmetrical Cell formed on a sintered pellet

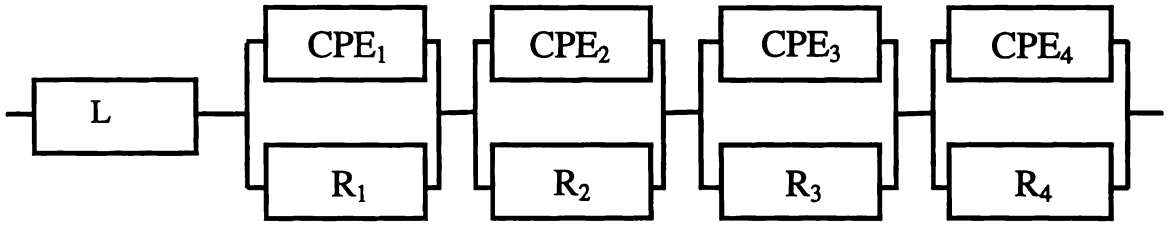

Figure 5.6. The simplest possible equivalent circuit for impedance spectra with 4 semicircles. L is an inductance originating from the testing equipment and R_1Q_1, R_2Q_2, R_3Q_3 and R_4Q_4 describe the electrode response (where CPE = capacitance, or Q*n, the constant phase element multiplied by n, the height of the curve).

From AC theory, the resistance of each of the components can be given by the intercepts on the x-axis. The value of the capacitor can be obtained from the apex frequency. Thus, in a real polycrystalline material, it is possible to separate out the bulk (intergrain) resistance from the grain boundary and electrode resistances, as shown in Figure 5.5. An impedance spectrum may consist of four semicircles (or more depending on the system), as shown if Figure 5.5, due to differences between impedence and the dielectrical constant in the grain, grain boundary, electrode and the interface between the sample and electrode.

The standard way of treating impedance data is to fit the impedance spectra to the simplest equivalent circuit. Fitting the impedance spectra to equivalent circuits is performed using a type of non-linear least squares analysis software package such as those developed by Boukamp[14] or Macdonald[15]. The process of finding a useful equivalent circuit is determined by the experimental data obtained and the proposed reaction taking place in the system. Usually, the equivalent circuit is modified to accommodate new experimental data as the mechanism is elucidated. Ultimately, the equivalent circuit chosen to represent the experimental data must reflect the physical and chemical information contained in the measured impedance spectra.

Using the 4 semicircles represented in Figure 5.5, the simplest possible equivalent circuit is shown in Figure 5.6. The inductance, L, originates from the leads of the experimental apparatus. The four parallel RQs in series describe the electrode impedance, which are the rate limiting processes. R is the resistance and Q is a constant phase element (CPE) with the admittance:

$$Q = Y_o(j\omega)^n \qquad (5.11)$$

The CPE has two constants Q and n. If n = -1, the CPE is an inductance with $L = Q^{-1}$; if n = 0, then the CPE is a resistance with $R = Q^{-1}$; if n = 0.5, the CPE is a Warburg diffusion, and if n = 1, the CPE is a capacitance with C = Q. The units of the CPE are variable, depending on the value of n:

$$Q = Fs^{-n} \qquad (5.12)$$

Most semi-circle are not, however, so well defined, and overlapping or depressed semicircles can occur, making full interpretation difficult.

After identifying the semicircles, bulk resistance can be ascertained and P_{O_2} dependency plots can be generated showing Log P_{O_2} versus conductivity as explained in Chapter 2 and shown in Chapter 7, Figure 7.4.

5.6 References

[1] D. A. Long, in *Raman Spectroscopy*, McGraw-Hill, United Kingdom 1977

[2] K. Nakamoto, in *Infrared and Raman Spectra of Inorganic Co-ordination Compounds 4th Edition*, Part I, Wiley Interscience, New York, 1986

[3] D. J. Gardiner & P. R. Graves (Eds.), *Practical Raman Spectroscopy*, Springer-Verlig, Berlin, Heideberg, 1989

[4] F. H. Pollak, in *Chemical Analysis: Analytical Raman Spectroscopy*, (Eds. J. G. Graselli, & B. J. Bulkin), John Wiley & Sons, New York, 1991, **114**, 137

[5] H. Lipson & H. Steeple, *Interpretation of X-ray Powder Diffraction Patterns*, Macmillan Co., London 1970

[6] J. S. Reeds, *Introduction to the Principles of Ceramic Processing*, John Wiley & Sons, New York 1987

[7] C. Whiston, *X-Ray methods, Analytical Chemistry by open learning*, John Wiley & Sons, New York 1987

[8] UNITCELL programme, T. J. B. Holland & S. A. T. Redfern, 1995

[9] R. W. Grimshaw, *The Chemistry and Physics of Clays*, John Wiley & Sons, Inc., New York, 1971

[10] J. R. MacDonald(Ed.), in *Impedance Spectroscopy*, John Wiley & Sons, New York, 1987

[11] K. Lark-Horovitz, V. A. Johnson, *Solid State Physics, Methods of Experimental Physics*, Vol 6. Academic Press, 1989

[12] M. Keitz, H. Bernard, E. Fernandes & E Schouler. Sci. Tech. Zirconia I, Adv. in Ceramics, 3. (Eds.) A. H. Heyer, L. W. Hobbles, Am. Ceram. Soc., 1981

[13] W. Gao & N. M. Sammes, *An introduction to electronic and ionic materials*, World Scientific Publishers, Singapore, 1999

[14] B. A. Boukamp. *Solid State Ionics*, 1986, **20**, 31

[15] J. R. Macdonald. Complex Non-linear Least Squares Immitance Fitting Program, Version 8/16/90. University of North Carolina, Chapel Hill 1990

Chapter Six

Results and Discussion for ABO_3 Perovskite Oxide ion conductors

6.1 Introduction

Outlined in this chapter are the experimental results and discussion relating to the structural examination of the ABO_3 perovskite oxides described in Chapter 3, where A = La and B = Ga, Fe and Gd.

In 1957 Geller reported the structure of $LaGaO_3$ as being orthorhombic at room temperature, having the space group P*bnm*[5]. He also reported the high temperature (above 900 °C) phase to be rhombohedral. Later, Ishihara et al.[1] reported the structure of both $LaGaO_3$ and doped $LaGaO_3$ ($La_{1-x}Sr_xGa_{1-y}Mg_yO_{3-\delta}$, known as LSGM where x=0-0.2 and y=0-0.2 and δ is the oxygen deficiency per unit formula, normally x/2) to be orthorhombic at room temperature. Feng and Goodenough[6] also reported $LaGaO_3$ to be an orthorhombic perovskite (a=5.20 Å, b=7.752 Å, and c=5.487 Å), iso-structural with $GdFeO_3$, but found that the structure of $La_{0.9}Sr_{0.1}Ga_{0.8}Mg_{0.2}O_{2.85}$ was a cubic perovskite, where a=3.911±0.003 Å. Studies since 1994 have predominantly reported all LSGM variations to be an orthorhombic perovskite at room temperature, refined to the space group of P*nma* (No. 62), with lattice parameters a=5.494 Å, b=5.525 Å and c=7.776 Å[7]. a=3.925 Å[6].

While much research has gone into studying LSGM, not so much data is available on the single substitution of either the A or B site of $LaGaO_3$ by Sr, Mg or other alternative cations. In addition to this, the effect of changing the B site cation from Ga to some other similar sized 3^+ cation has not been extensively studied. A better understanding of the effect of ionic radius of the A and B cations on the resulting

structure of an ABO_3 perovskite materials could possibly allow for the prediction of new materials for applications outlined in Chapter 1, Section 1.6.

$LaGaO_3$ has been doped with Sr on the A-site and Mg and Cr on the B-site. XRD and Raman studies have been undertaken to determine the structure and to detect any phase changes with increasing dopant concentration. $LaFeO_3$ has been doped with Mg on the B-site and powder X-ray diffraction has been used to determine the structure and identify any impurities or phase changes. Due to the dark colour of materials containing iron, a Raman spectrum was obtained only for $LaFeO_3$. $LaGdO_3$ was also studied and both Raman and powder X-ray analysis were undertaken.

6.2 $LaGaO_3$ based materials

Samples of A- and B-site doped $LaGaO_3$ were investigated using X-ray diffraction and Raman spectroscopy to provide structural information on the effect of specific dopants (Sr, Cr and Mg) and dopant concentrations on the perovskite structure.

6.2.1 Sr Doped $LaGaO_3$

Figure 6.1(a-e) show the XRD patterns of $La_{1-x}Sr_xGaO_{3-\delta}$ at x = 0, 0.05, 0.1, 0.15 and 0.2 respectively. The XRD pattern of $LaGaO_3$ (x = 0) shows a typical orthorhombic pattern. With increase in Sr dopant concentration, several structural changes can be observed from the X-ray diffraction data, namely several weak peaks due to secondary phase $SrLaGa_3O_7$ [JCPDS #45-0637]. Ishihara et al.[1] showed, for similar doped systems, $(La_{0.9}Ln_{0.1})_{0.8}Sr_{0.2}Ga_{0.8}Mg_{0.2}O_{3-\delta}$ where Ln = Nd, Sm, Gd, Y and Yb, that a different secondary phase, that of La_4SrO_7 formed.

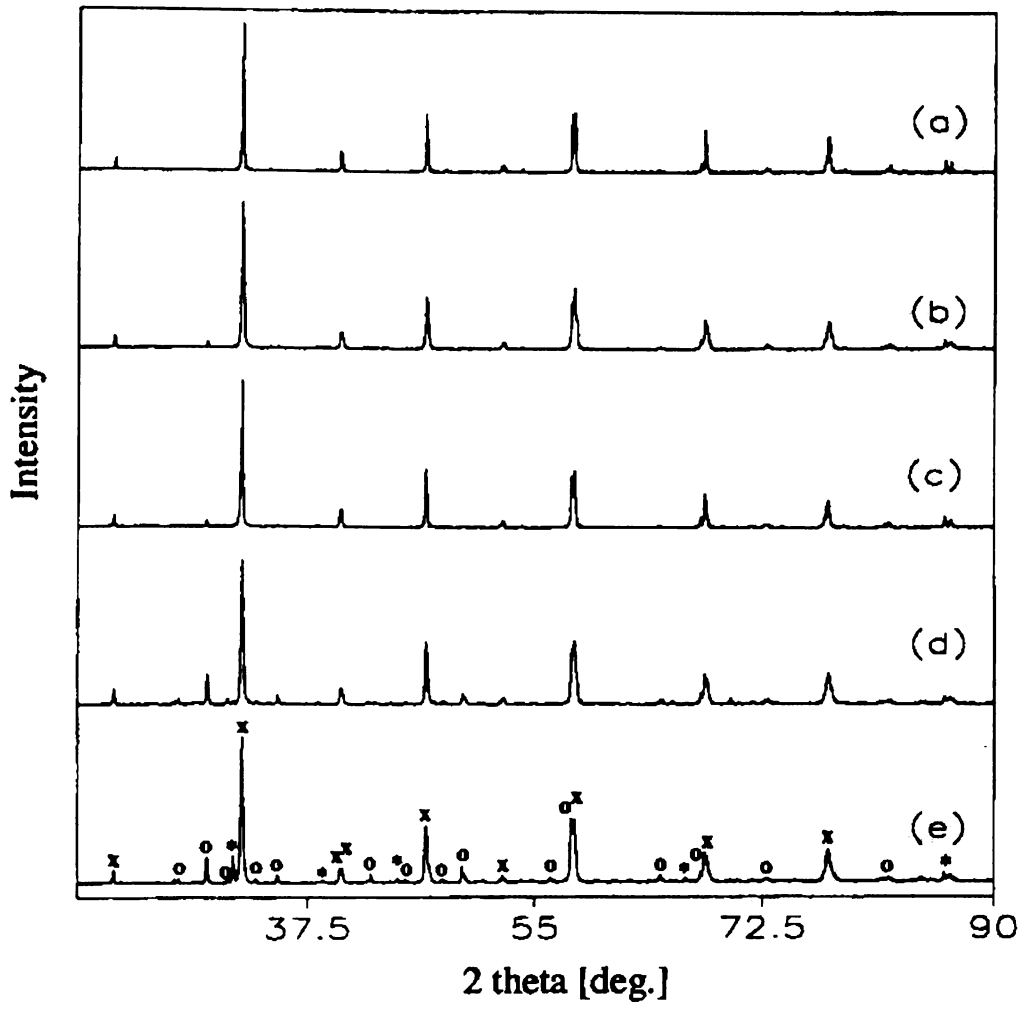

Figure 6.1 Powder X-ray diffraction patterns of $La_{1-x}Sr_xGaO_{3-\delta}$: (a)x = 0; (b) x = 0.5; (c) x = 0.1; (d) x = 0.15; (e) x = 0.2 [(X) orthorhombic $LaGaO_3$ perovskite pattern, (O) $SrLaGa_3O_7$, (∗) unidentified peaks].

Figure 6.2 shows a plot of unit cell volume as a function of Sr dopant concentration. It can be seen that by increasing from 0 to 15 mol% Sr (x = 0-0.15) A-site doping, the orthorhombic structure distorts, with a decrease in the unit cell volume. Between 15 and 20 mol% Sr (x = 0.15-0.2), however, an increase in the cell volume is observed. The reason for this is possibly a result of the increased second phase, $SrGa_3O_7$, present at this dopant concentration, causing distortion in the lattice. Ishihara et al.[2] also found impure crystal phases such as $SrGaO_3$ and La_4SrO_7 above x = 0.1 for $La_{1-x}Sr_xGaO_3$ by X-ray analysis using the same fabrication technique.

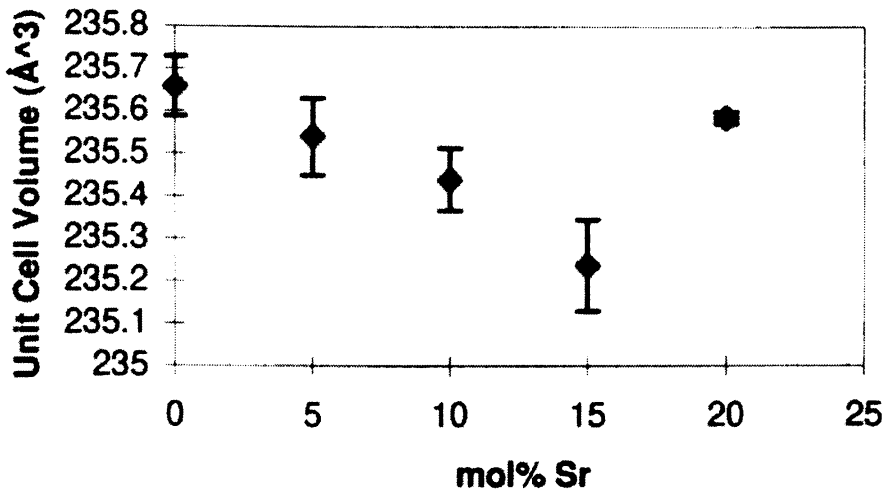

Figure 6.2. Change in the unit cell volume with increase in Sr A-site dopant in $La_{1-x}Sr_xGaO_{3-\delta}$.

6.2.2 Cr Doped $LaGaO_3$

$LaGaO_3$ doped on the B-site with Cr was investigated using powder XRD. Figure 6.3 shows the powder XRD patterns for $LaGa_{1-y}Cr_yO_{3-\delta}$ at y = 0-0.2. With increasing Cr dopant concentration there is little change observed in the pattern and it remains as an orthorhombic structure up to y = 0.2.

The peak at ca. 32° in Figure 6.4, and expanded in Figure 6.5, for $LaGa_{1-y}Cr_yO_{3-\delta}$ shows a second peak at 32.37°, which is coincident with that of the orthorhombic phase $LaCrO_3$ [JCPDS #33-0701], although there is a large degree of overlap between these two patterns and this peak remains at relatively constant intensity with increase in dopant concentration, at x > 0. Thus, it is, therefore, likely to be a splitting of the pattern due to a change in the phase with Cr on the B-site of $LaGaO_3$. It should be noted that the peak at 32.37° was also present for the non-doped $LaGaO_3$, although much lower in intensity. This could be postulated as being due to the presence of an orthorhombic $GdFeO_3$-type system[3]. However, at x = 0.05, the peak increases in intensity and at between x = 0.05 and 0.2, it remains at a relatively constant intensity, as described above.

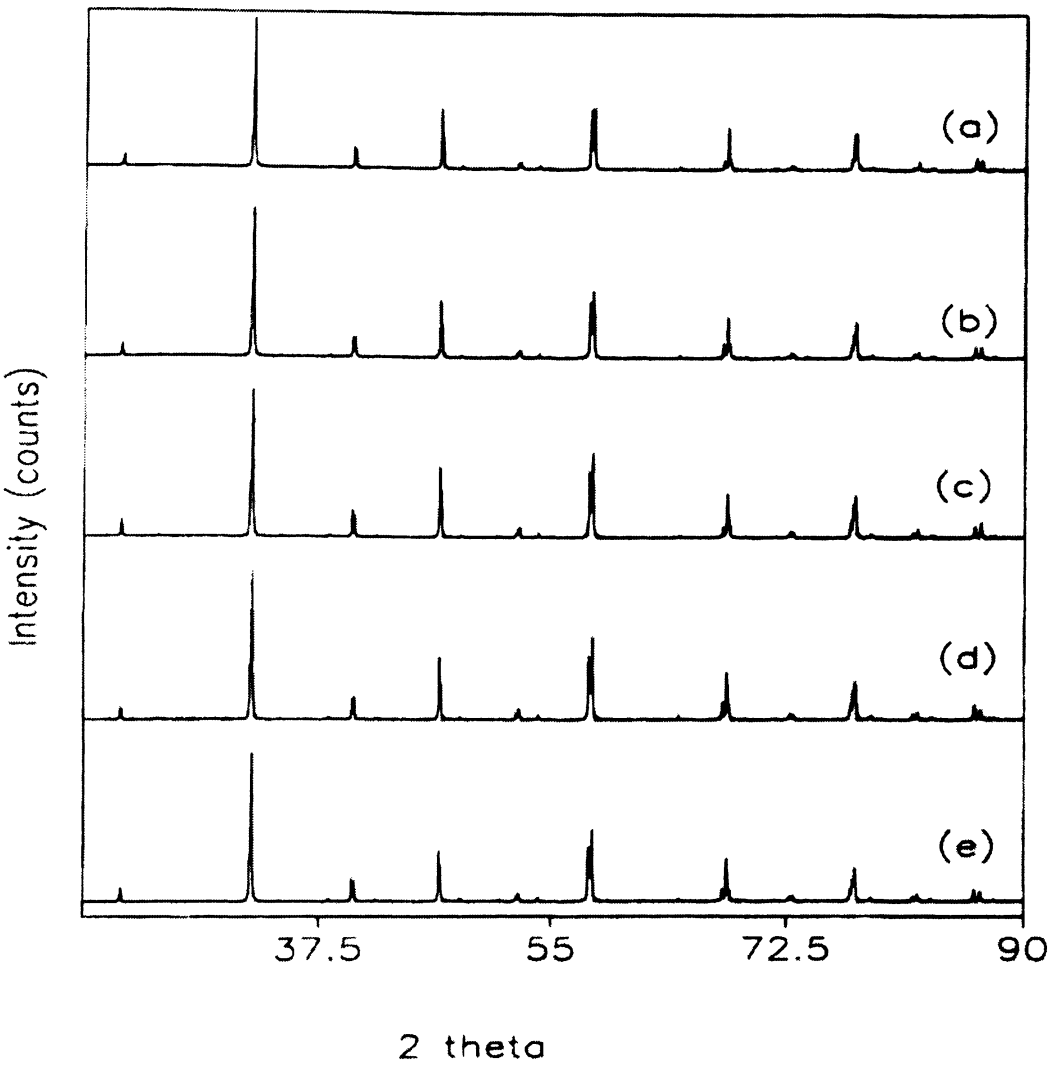

Figure 6.3. Powder X-ray diffraction of $LaGa_{1-y}Cr_yO_{3-\delta}$: (a) y = 0; (b) y = 0.5; (c) y = 0.1; (d) y = 0.15; (e) y = 0.2

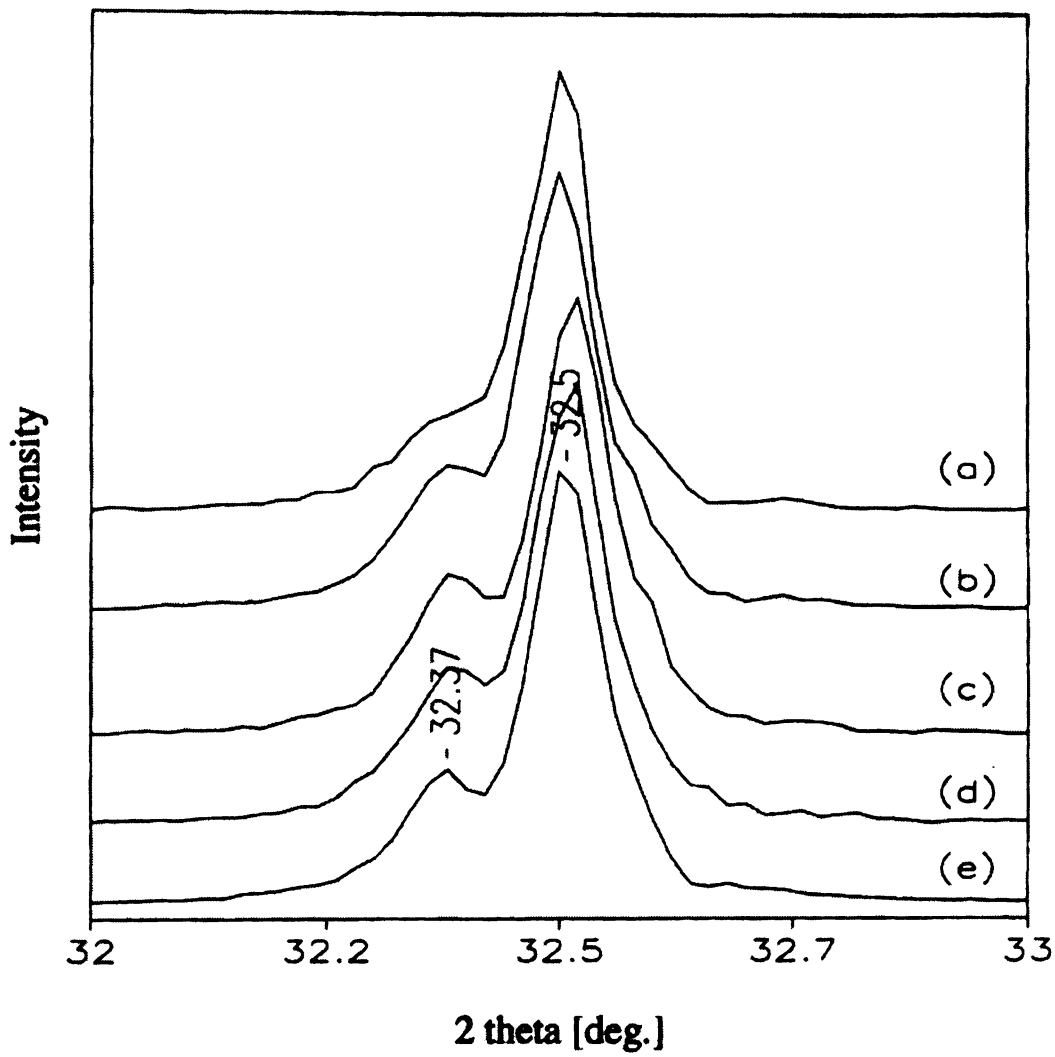

Figure 6.4. Powder x-ray diffraction patterns of $LaGa_{1-y}Cr_yO_{3-\delta}$: (a) y = 0; (b) y = 0.5; (c) y = 0.1; (d) y = 0.15; (e) y = 0.2 in the range 31-34 °C [2θ].

Figure 6.5 shows a plot of unit cell volume as a function of Cr dopant concentration in $LaGa_{1-y}Cr_yO_{3-\delta}$ between y = 0 and 0.2 (0 and 20 mol% Cr). It can be seen that by increasing from 0 to 10 mol% Cr (y = 0-0.10) B-site doping, the orthorhombic structure distorts, with a decrease in the unit cell volume. Between 10 and 20 mol% Cr, there is a slight increase in the unit cell volume. The reason for this phenomenon cannot be fully explained, although the increase in dopant concentration has caused a large distortion in the lattice.

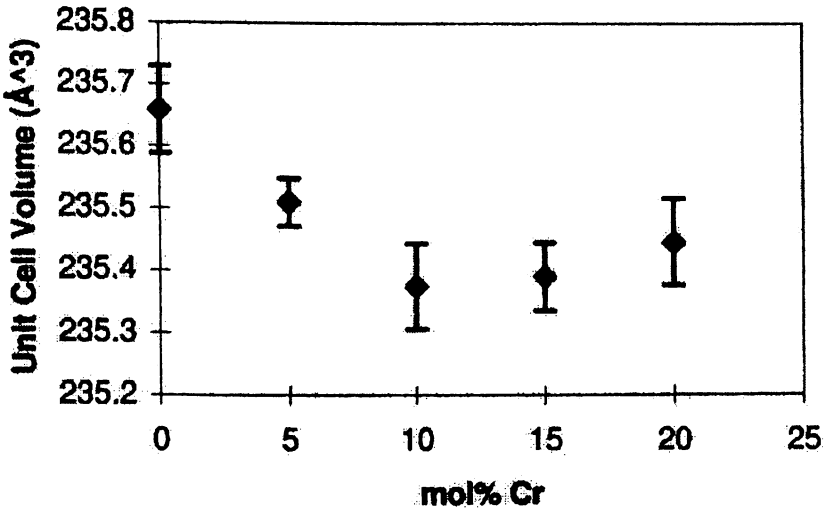

Figure 6.5. Change in the unit cell volume with increase in Cr B-site dopant in $LaGa_{1-y}Cr_yO_{3-\delta}$.

6.2.3 Mg Doped $LaGaO_3$

$LaGaO_3$ doped on the B-site with Mg was investigated using XRD. Figure 6.6 shows the powder XRD patterns for $LaGa_{1-y}Mg_yO_{3-\delta}$ at y = 0-0.2. With increasing Mg dopant concentration there is shift in the orthorhombic $LaGaO_3$ pattern observed. Weak peaks are also observed due to the formation of secondary phases, which increase with increase in Mg dopant concentration. A secondary phase has been identified by XRD as $La_4Ga_2O_9$ [JCPDS #37-1433] and a third phase indicated by a peak at 28.935° (*d*=3.08321Å) at y = 0.2 has not been identified. Ishihara et al.[3] found no sign of secondary phases attributable to Mg dopant concentration, detectable by X-ray diffraction until above x = 0.4. The overall pattern remains as the orthorhombic up to 20 mol% Mg. Figure 6.7 shows a plot of unit cell volume as a function of Mg dopant concentration in $LaGa_{1-y}Mg_yO_{3-\delta}$ between y = 0 and 0.2 (0 and 20 mol% Mg). It can be seen that by increasing from 0 to 15 mol% Mg (y = 0-0.15) B-site doping, the orthorhombic structure distorts, with a decrease in the unit cell volume. Between 15 and 20 mol% Mg, there is a slight increase in the unit cell volume, similar to that observed for the Cr-doped sample, possibly due to the

formation of a second phase (observed in Raman spectroscopy, see Figure 6.9), $La_4Ga_2O_9$, causing a distortion of the lattice.

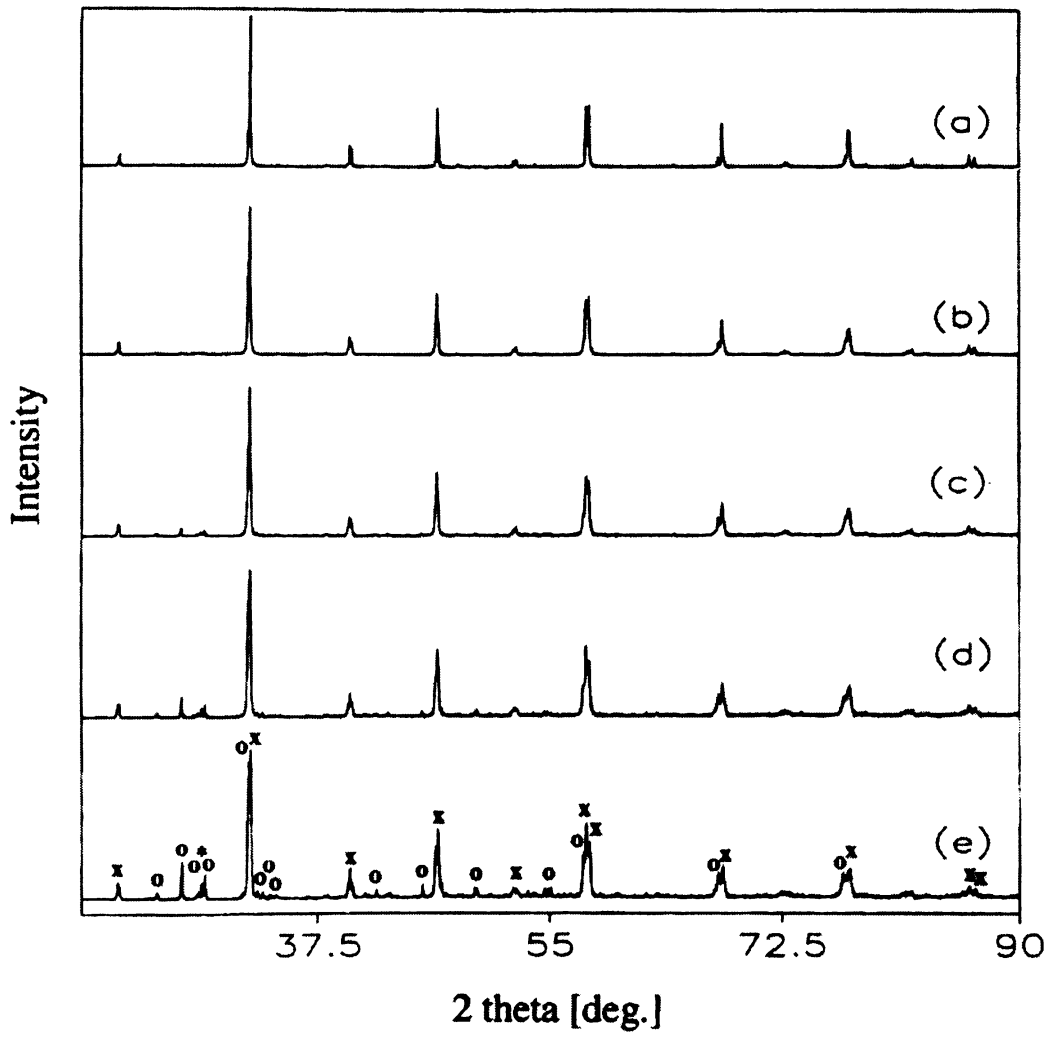

Figure 6.6. Powder X-ray diffraction of $LaGa_{1-y}Mg_yO_{3-\delta}$: (a) y = 0; (b) y = 0.5; (c) y = 0.1; (d) y = 0.15; (e) y = 0.2 [(X) orthorhombic $LaGaO_3$ perovskite pattern, (O) $La_4Ga_2O_9$, (∗) unidentified peaks].

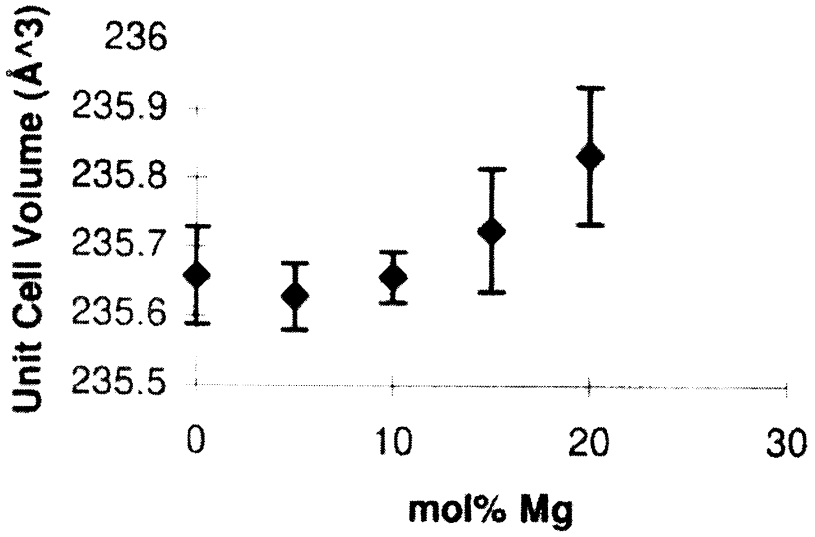

Figure 6.7. Change in the unit cell volume with increase in Mg B-site dopant concentration in $LaGa_{1-y}Mg_yO_{3-\delta}$.

6.2.4 Discussion of $LaGaO_3$ doped Material

As shown in sections 6.2.1 to 6.2.3, powder X-ray diffraction studies show a similar pattern of results for both the A- and B-site dopants. The addition of Sr, Cr or Mg appears to cause a decrease in the unit cell volume (UCV), and given that the dopant materials have a lower valence charge (2^+), their increase in concentration appears to cause a contraction of the structure. Sr, Cr and Mg dopant concentrations all appear to show a slight increase in UCV after 15 mol%. Powder X-ray studies have revealed the presence of a second phase or impurity in each material (less in the Cr doped $LaGaO_3$ however), and the presence of a second phase is particularly noticeable in the Mg doped material. While Ishihara et al.[1] undertook a similar fabrication route, they did not report the presence of any impurities until greater than 40 mol% Mg. However, both this study and that of Ishihara et al.[1] confirm the presence of impurities in the Sr doped material, with $SrLaGa_3O_7$ and La_4SrO_7 being reported.

6.2.5 Raman spectroscopy, $LaGaO_3$ and Mg doped $LaGaO_3$

Raman spectroscopy of these doped lanthanum gallate materials was carried out to verify the structural information determined from X-ray diffraction results. Initially, the base material $LaGaO_3$ was studied to obtain spectra of the system.

$LaGaO_3$ has an orthorhombic structure of the $GdFeO_3$–type, with the space group *Pnma*[4]. From factor group analysis using the Bhagavantum-Venkaryudu method, the irreducible representation of the optical vibration (Γ_{op}) and acoustic modes (Γ_{ac}) are given as follows:

$$\Gamma_{op} = 7A_g + 7B_{1g} + 5B_{2g} + 5B_{3g} + 8A_u + 7B_{1u} + 9B_{2u} + 9B_{3u}$$
$$\quad (R) \quad (R) \quad (R) \quad (R) \quad (i) \quad (ir) \quad (ir) \quad (ir)$$

$$\Gamma_{ac} = B_{1u} + B_{2u} + B_{3u}$$

The irreducible representation here shows there are 24 Raman active modes ($7A_g$ + $7B_{1g} + 5B_{2g} + 5B_{3g}$) and 25 infrared active modes ($7B_{1u} + 9B_{2u} + 9B_{3u}$), while the 8_{Au} modes are inactive in both Raman and infrared as reported by Saine et al.[5] for lanthanum gallates. The room temperature Raman spectrum of $LaGaO_3$ prepared from solid state methods shows 18 bands at 55, 92, 101, 117, 137, 147, 173, 255, 277, 295, 335, 357, 403, 415, 433, 451, 584 and 708 cm^{-1} as shown in Figure 6.8 and the band positions (intensities) are shown in Table 6.1.

The low-temperature Raman spectrum of $LaGaO_3$ (Figure 6.8b) shows bands at 66, 108, 126, 141(sh), 146, 152, 179, 264, 284, 340, 363, 415, 433 and 453 cm^{-1}, with weak bands at 245 and 331 cm^{-1} at –196 °C, as shown in Table 6.1. The band at 92 cm^{-1} has disappeared at –196 °C and bands at 141(sh), 146 and 415 cm^{-1} have been resolved. Around half the number of modes are observed in relation to the predicted 24.

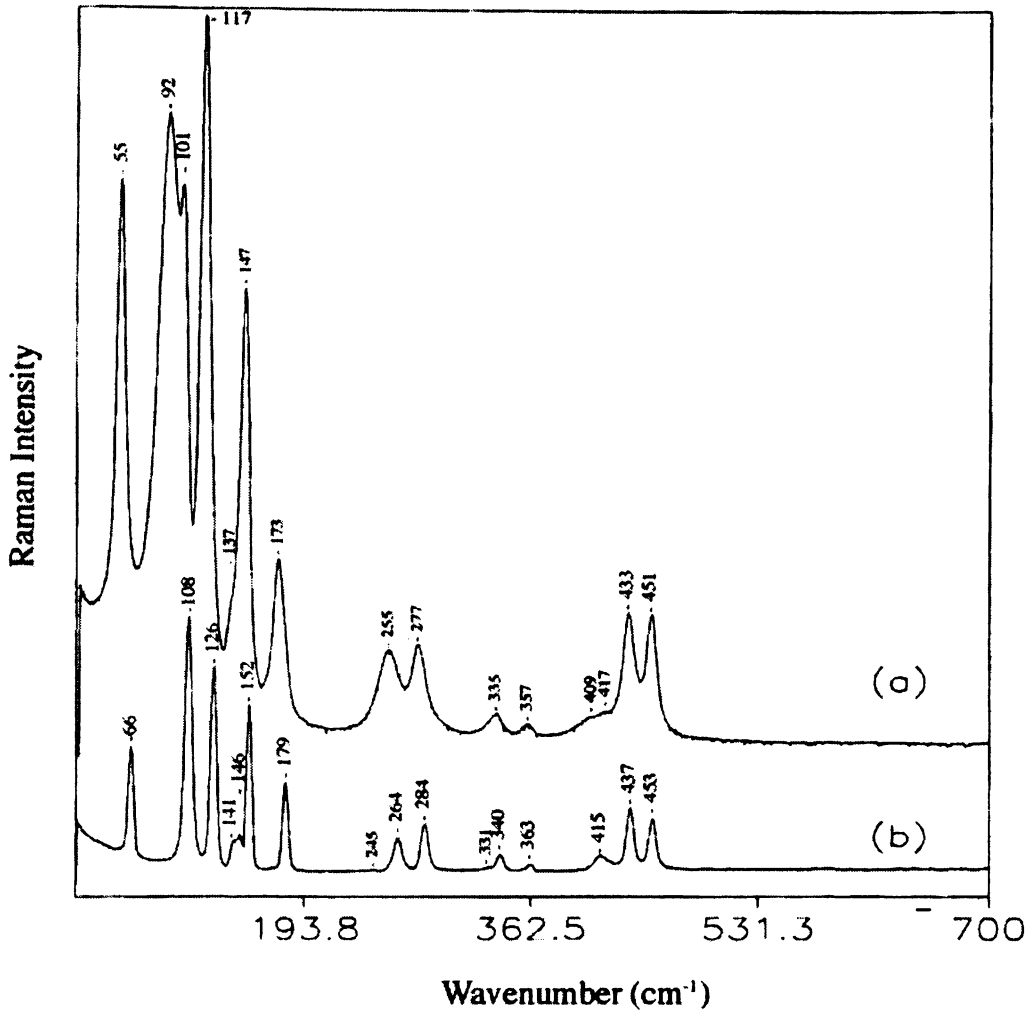

Figure 6.8. Raman spectra of $LaGaO_3$ at (a) room temperature 21 °C, and (b) –196 °C

The low temperature (LT) phase of $LaGaO_3$ can be similarly compared to known band positions and assignments of perovskite materials. Table 6.2 shows the assignment of the observed bands of LT-$LaGaO_3$ with comparison to the observed and calculated bands for $SmAlO_3$[5]. The correlation between the band positions on $SmAlO_3$ and $LaGaO_3$ was made on the basis of the spectral profiles. Bands at 584 and 708 cm^{-1} (at 21 °C) are likely overtones due to their relatively weak intensity and high wavenumber position.

Figure 6.9 shows a comparison of the Raman spectra of $LaGa_{1-y}Mg_yO_{3-\delta}$ at y = 0.1-0.2. It can be seen that the spectral profile of the orthorhombic $LaGaO_3$ remains as the Mg dopant concentration increases, however a secondary phase occurs with

Table 6.1. Raman band positions for $LaGaO_3$ and Mg-doped $LaGaO_3$

$LaGaO_3$		$LaGa_{0.8}Mg_{0.2}O_{3-\delta}$	$La_4Ga_2O_9$
RT (21 °C)	-196 °C		
55(s)	66(m)	52(s) 55(sh)	52(sh)
92(s)		90(w)	
101(s)	108(s)		104(w)
117(s)	126(s)	115(w)	
137(sh)	141(sh)		
	146(m)		
147(s)	152(s)	147(w)	
173(m)	179(m)		187(w)
	245(w)		
255(m)	264(m)	243(m)	240(m)
277(m)	284(m)		
	331(w)	295(m)	293(s)
335(w)	340(w)		
357(w)	363(w)	356(s)	354(s)
409(sh)	415(w)		405(w)
417(sh)			
433(m)	437(m)	433(w)	
451(m)	453(m)	450(w)	467(w)
584(w)		584(w)	581(w)
		654(w)	
708(w)		708(s)	704(s)

w, weak; m, medium; s, strong relative intensity and sh, shoulder.

increase in Mg dopant concentration up to 20 mol% Mg. This can be identified by the bands at 243, 295 and 356 cm^{-1} which become more predominant at 20 mol% Mg, which match those of $La_4Ga_2O_9$ (Figure 6.9f). Raman spectra of the Sr-doped and Cr-doped samples proved to be difficult due to the highly coloured nature of the samples.

Table 6.2. Mode assignment of the Raman spectra of low temperature $LaGaO_3$

Mode	$SmAlO_3$ (RT)		$LaGaO_3$ (21 °C)
	Observed[5]	Calculated[5]	
	$\tilde{\nu}$ /cm^{-1}		$\tilde{\nu}$ /cm^{-1}
B_{3g}	~530	528	451
A_g	522	527	433
B_{1g}		528	
B_{2g}/B_{2g}	508	512/507	417
B_{1g}		508	
B_{3g}	480	484	404
B_{2g}	480	476	
A_g		482	
B_{1g}		448	
B_{1g}	408	389	357
B_{2g}	390	390	331*
B_{3g}	392	390	335
A_g	345	351	277
A_g	286	271	255
B_{3g}	198	212	173
A_g	200	191	147
B_{1g}	170	188	137
B_{2g}	143	106	117
B_{3g}	136	126	101
B_{1g}	110	96	92
A_g		90	
A_g	78	85	55
B_{1g}		84	

* observed at –196 °C.

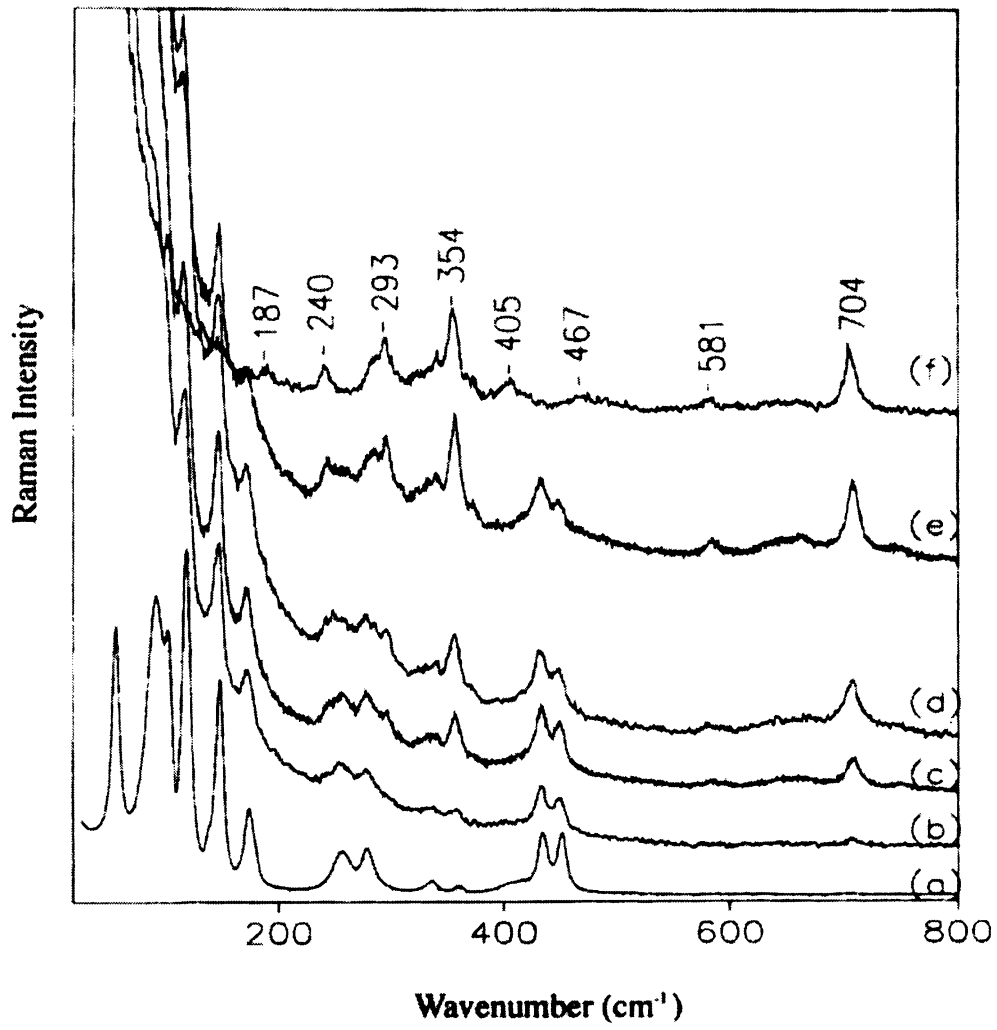

Figure 6.9. Comparison of room temperature Raman Spectra of $LaGa_{1-y}Mg_yO_{3-\delta}$: (a) y = 0) y = 0; (b) y = 0.5; (c) y = 0.1; (d) y = 0.15; (e) y = 0.2 and (f) $La_4Ga_2O_9$.

6.3 $LaFeO_3$

Like $LaGaO_3$, $LaFeO_3$ belongs to the orthorhombic perovskite group of materials having the space group P*nma* and like $LaGaO_3$, $LaFeO_3$ also undergoes a phase transition from the orthorhombic (P*nma*) structure to a rhombohedral R-*3c* phase, occurring, for $LaFeO_3$, at 980 °C[6]. However, little research exists on the doping of $LaFeO_3$ with Mg, as has been undertaken with $LaGaO_3$, in order to compare the resulting effect.

6.3.1 Mg Doped $LaFeO_3$,

Figure 6.10 shows the X-ray diffraction pattern of the system $LaFe_{1-x}Mg_xO_{3-\delta}$, where x = 0-0.2 at the sinter temperature of 1400 °C, and Table 6.3 lists the percent dopant level, sinter temperature, lattice parameters (a, b and c) and the unit cell volume for each sample studied. It can be seen that there is little change in the spectra with increasing Mg-dopant concentration and the profile remains as that of the pure $LaFeO_3$ within this dopant range. The only significant changes observed in the spectrum are those of the impurities, La_2O_3 [JCPDS #05-0602] and La_2MgO_x [JCPDS # 42-0339], marked accordingly. These impurities may have occurred due to a lack of complete reaction during the synthesis of the material. The materials were fabricated using coprecipitation, however, the ratio of nitrates to precipitant (1:4) was different to that used for coprecipitation of $LaGdO_3$ (being 1:10) and as such, it appears that the precipitation of the final product was not completed. In addition to this, one calcination step was insufficient to cause complete reaction of the material.

Table 6.3: Lattice parameters of $LaFe_{1-x}Mg_xO_{3-\delta}$, where x = 0-0.2 at differing sintering temperatures

Sinter Temp. (°C)	%Mg Dopant	Volume (Å^3)	Lattice Parameters (Å)		
			a	b	c
1350	0	241.9903	5.5579	7.844	5.5508
1350	10	242.0384	5.5545	7.8468	5.5532
1350	15	241.9351	5.556	7.8495	5.5475
1350	20	242.0676	5.557	7.8457	5.5522
1350	0	241.9903	5.5579	7.844	5.5508
1400	5	242.1475	5.5588	7.8486	5.5502
1400	10	242.1772	5.5593	7.8528	5.5474
1400	15	241.8781	5.5589	7.8486	5.544
1400	20	242.7439	5.5625	7.8419	5.5649
1350	0	241.9903	5.5579	7.844	5.5508
1450	5	242.5139	5.5606	7.8511	5.555
1450	10	241.8833	5.5552	7.8459	5.5496
1450	15	241.68	5.5546	7.8369	5.5519
1450	20	242.2013	5.5573	7.847	5.5541

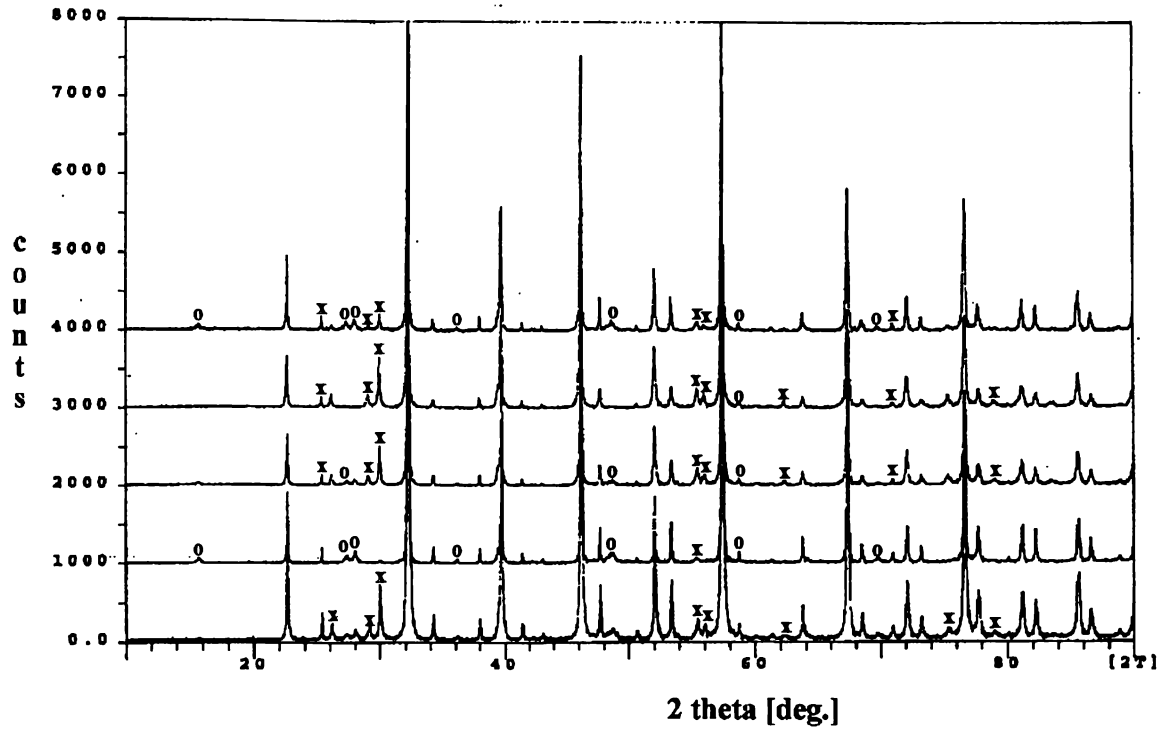

Figure 6.10: XRD pattern of the system $LaFe_{1-x}Mg_xO_{3-\delta}$, where x = 0-0.2 at sintering temperature of 1400 °C. o = La_2MgO_x and x = La_2O_3

Figure 6.11 shows the effect of increasing Mg concentration on the unit cell volume of $LaFe_{1-x}Mg_xO_{3-\delta}$ (x = 0.05-0.2) at 1450 °C. A minimum volume of 241.68 $Å^3$ at 15% Mg is the smallest unit cell volume achieved over the range studied. Table 6.3 also illustrates this point and shows that the overall change in unit cell volume is from 242.7439 $Å^3$ to 241.68 $Å^3$, an overall change of only ca. 0.4% of the unit cell volume.

Figure 6.12 shows the effect of sintering temperature on $LaFe_{1-x}Mg_xO_{3-\delta}$ where x = 0.15 and shows the unit cell volume decreasing with increasing sintering temperature. It should be noted that the increase in sintering temperature from 1400 to 1450 °C appears to cause a drop in unit cell volume (except for 5% samples), however, at temperatures lower than that, the effect is less structured.

Figure 6.13 shows the XRD patterns of $LaFe_{0.85}Mg_{0.15}O_{3-\delta}$, at sintering temperatures of 1350, 1400 and 1450 °C, where o = La_2MgO_x and x = La_2O_3. La_2O_3 appears to

increase with increasing sintering temperature, but the concentration of La_2MgO_x decreases with sintering temperature.

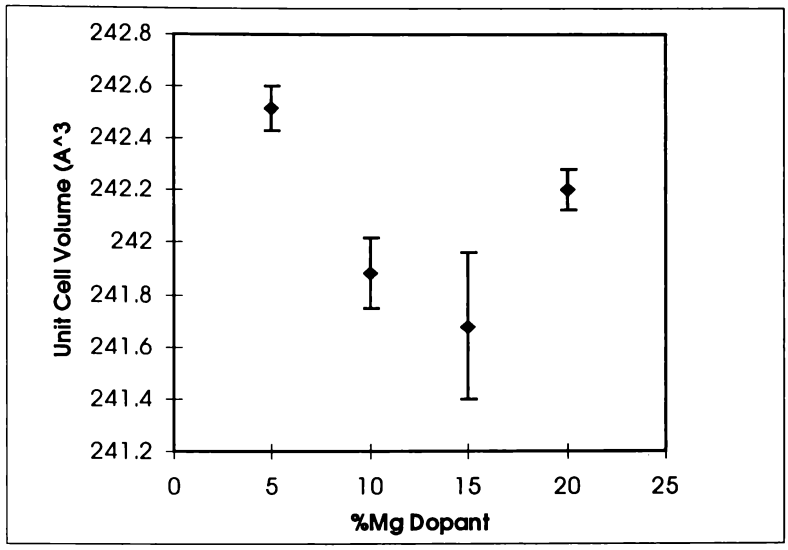

Figure 6.11: Graph of Magnesium dopant concentration (Wt %) versus unit cell volume ($Å^3$) at 1450 °C. Error bars are ± standard deviation

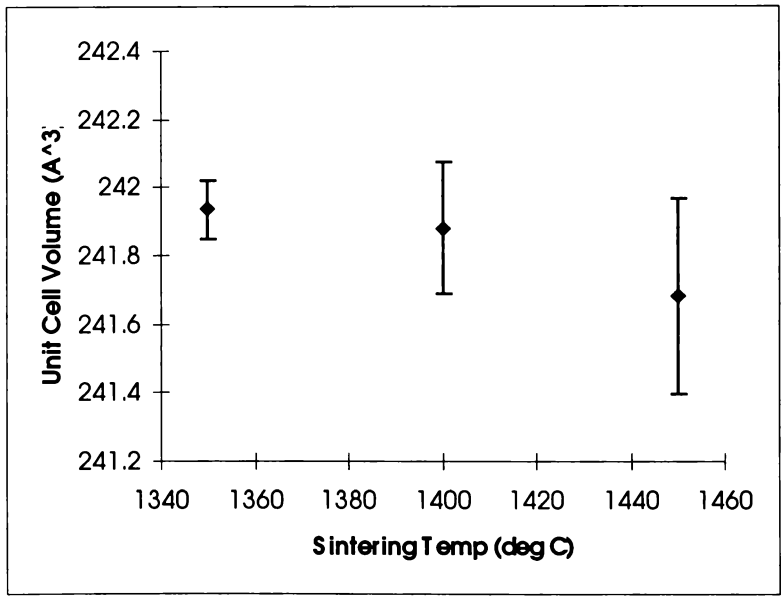

Figure 6.12: Graph of sintering temperature versus Unit cell volume for $LaFe_{0.85}Mg_{0.15}O_{3-\delta}$, at sintering temperatures of 1350, 1400 and 1450 °C. Error bars are ± standard deviation

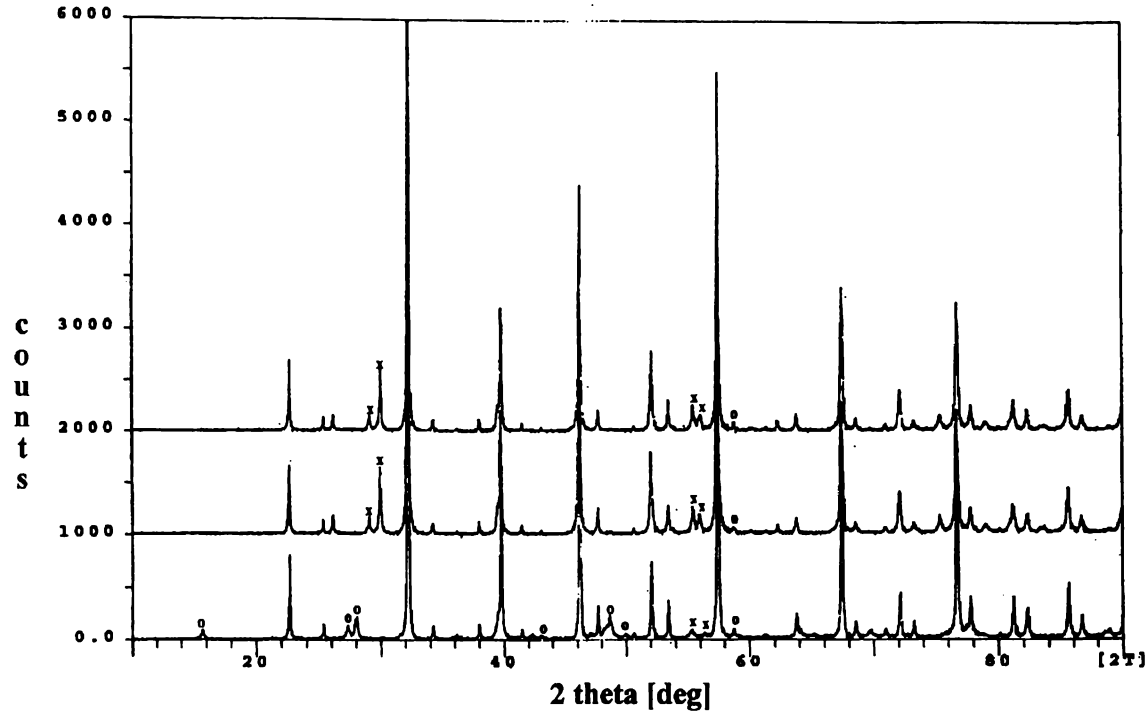

Figure 6.13: XRD pattern of the system $LaFe_{0.85}Mg_{0.15}O_{3-\delta}$, at sintering temperatures of 1350, 1400 and 1450 °C. o = La_2MgO_x and x = La_2O_3

6.3.2 Raman of $LaFeO_3$

For the two phases of $LaFeO_3$, factor group analysis has been performed to describe the number and type of modes predicted for the individual structures and thus, the number of bands observed in the spectra. Following are the irreducible representations for both the orthorhombic and rhombohedral structures, where Γ_{op} are the optical vibrational modes and Γ_{ac} are the acoustic modes. R: Raman active, ir: Infrared active, i: inactive

Orthorhombic, LT-$LaFeO_3$

Pnma (No. 62)

$$\Gamma_{op} = \underset{(R)}{7A_g} + \underset{(R)}{7B_{1g}} + \underset{(R)}{5B_{2g}} + \underset{(R)}{5B_{3g}} + \underset{(i)}{8A_u} + \underset{(ir)}{7B_{1u}} + \underset{(ir)}{9B_{2u}} + \underset{(ir)}{9B_{3u}}$$

$$\Gamma_{ac} = B_{1u} + B_{2u} + B_{3u}$$

A total of 24 Raman active, 25 infrared active and 8 inactive modes.

Rhombohedral HT-$LaFeO_3$

R-*3c* (No.167)

$\Gamma_{op} = A_g + 3A_{2g} + 4E_g + 2A_{1u} + 3A_{2u} + 5E_u$

(R) (i) (R) (i) (ir) (ir)

$\Gamma_{ac} = A_{2u} + E_u$

A total of 5 Raman active, 8 infrared active and 5 inactive modes.

Figure 6.14 shows the Raman spectrum of $LaFeO_3$ (sintered at 1450 °C) at 27 °C and –196 °C obtained using a 647.1 nm laser line. Although the signal-to-noise ratio observed for these spectra is low, likely to be due to the darkly coloured nature of the material absorbing the laser light, several bands were discernible. It can be seen that there are 9 bands observed at room temperature (27 °C) and 8 bands in the spectrum at low temperature (-196 °C). The band positions are listed in Table 6.4 and are compared with those reported in the literature for isostructural compounds: $SmAlO_3$[6] and $LaGaO_3$. Mode assignment of the observed bands was determined by comparison of the Raman profiles and relative band positions of $LaFeO_3$ to those of $SmAlO_3$ and $LaGaO_3$. The spectrum of $LaFeO_3$ (at 27 °C) is also compared to the orthorhombic (at 21 °C) and rhombohedral (at 500 °C) spectra of $LaGaO_3$, as shown in Figure 6.15. It can be seen in Figure 6.15 that the spectrum compares more closely to that of the orthorhombic phase of $LaGaO_3$, than that of the rhombohedral. The spectrum of the rhombohedral phase has only 4 Raman bands observed due to the higher symmetry of the structure. Therefore, $LaFeO_3$ has a lower symmetry than rhombohedral, and is most likely orthorhombic because the number of bands observed and the x-ray diffraction information suggests this. Features in the spectrum of $LaFeO_3$ at –196 °C, observed at 532, 605 and 779 cm^{-1} do not occur in the spectrum at room temperature and are not assigned.

Table 6.4. Raman band positions and mode assignment of $LaFeO_3$ at 27 °C and −196 °C compared with those of $SmAlO_3$ and $LaGaO_3$.

Mode	$SmAlO_3$ Band positions at RT		$LaGaO_3$ Band Positions at 21 °C[7]	$LaFeO_3$ Band Positions at 27°C this work	$LaFeO_3$ Band Positions at −196°C [this work]
					605
					532
	Observed[6]	Calculated[6]			
B_{3g}	~530	528	451	429	434
A_g	522	527	433	413	418
B_{1g}		528			
B_{2g}/B_{2g}	508	512/507	417		
B_{1g}		508			
B_{3g}	480	484	404		
B_{2g}	480	476			
A_g		482			
B_{1g}		448			
B_{1g}	408	389	357		340
B_{2g}	390	390	331*		
B_{3g}	392	390	335		
A_g	345	351	277	289	
A_g	286	271	255	261	
B_{3g}	198	212	173	227	
A_g	200	191	147	176	187
B_{1g}	170	188	137	150	167
B_{2g}	143	106	117	ca. 140(sh)	144
B_{3g}	136	126	101		
B_{1g}	110	96	92	102	
A_g		90			
A_g	78	85	55		
B_{1g}		84			

* observed at −196 °C. KEY: sh = shoulder band, RT = room temperature.

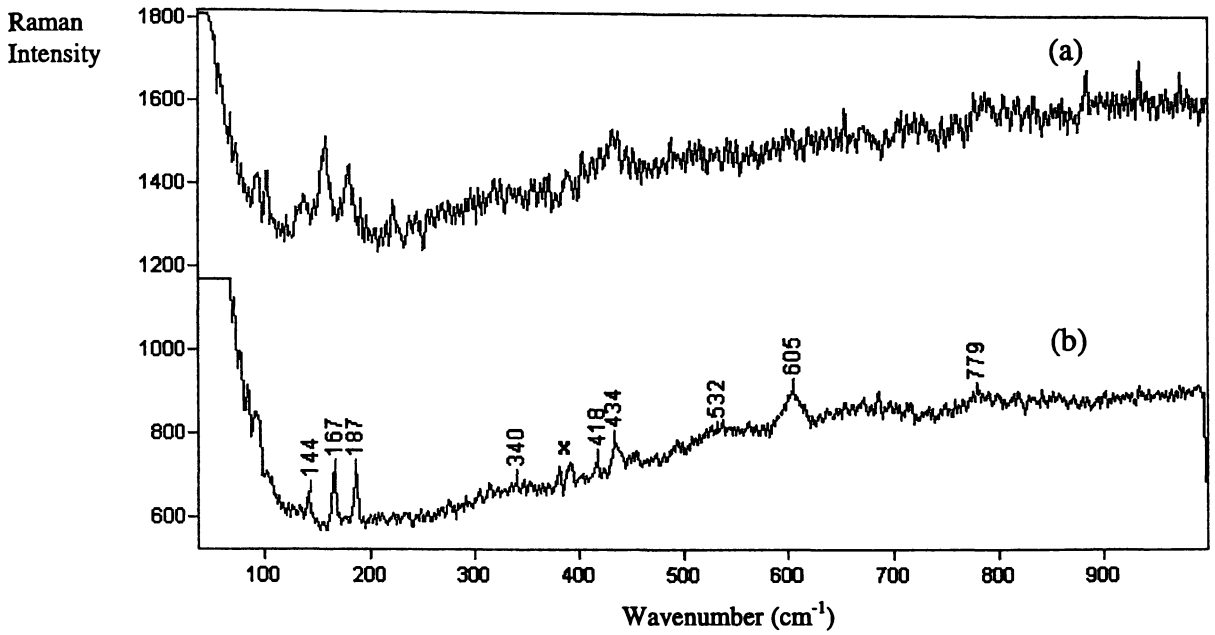

Figure 6.14 Raman spectrum of $LaFeO_3$ at (a) room temperature (27 °C) and (b) −196 °C. x = incomplete plasma line subtraction.

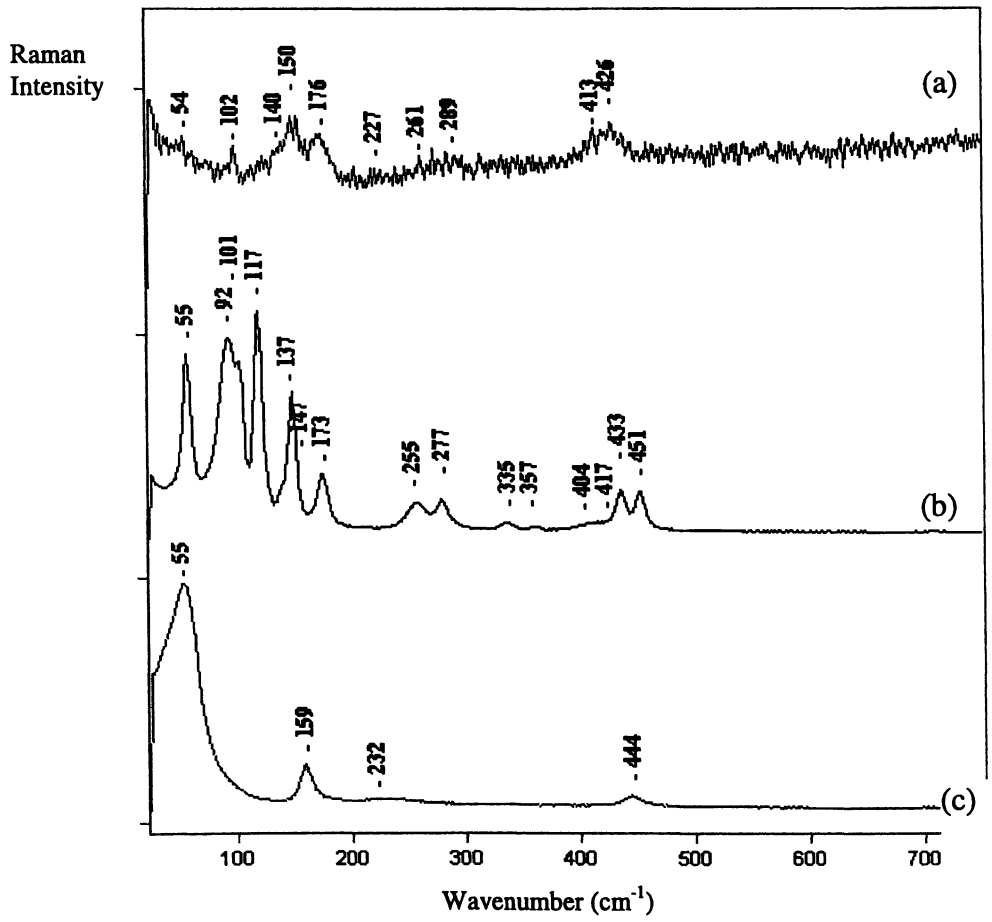

Figure 6.15 Comparison of Raman spectra of $LaFeO_3$ at 27 °C (a), $LaGaO_3$ at 25 °C (b) and 500 °C (c).

6.4 $LaGdO_3$

The synthesis of $LaGdO_3$, according to the literature, has only been undertaken using the solid state mixing technique, measuring and mixing the oxides at the required stoichiometry, then calcination and sintering at, in the case of $LaGdO_3$, a high pressure[8-10] 68-70]. In this study, a co-precipitation technique was used to fabricate $LaGdO_3$.

Figure 6.16 show the powder X-ray diffraction patterns for $LaGdO_3$ sintered at various temperatures. There appears to be a single monoclinic phase formed at each temperature. The patterns of pure La_2O_3 or Gd_2O_3 do not overlap with peaks observed in these patterns, therefore it is unlikely the starting materials are present. The cell parameters were calculated for each pattern based on the hkl values for B-Gd_2O_3 [JCPDS #42-1465] and are shown in Table 6.5. From Table 6.5, it can be seen that the cell parameters decrease in magnitude with increasing sintering temperature, except for parameter 'a', which shows an increase from 1250 °C to 1350 °C before decreasing. However, the overall cell volume shows only a small decrease with increasing sinter temperature as shown in Figure 6.17. This may be attributed to the increased peak intensity of the XRD patterns with increase in sintering temperature, allowing more accurate cell calculation. The cell volumes observed in this work are however significantly different to that observed by Wang et al.[8]. Preparation method and sintering temperature can have a significant effect on the structural type produced and cell volume for perovskites such as lanthanum strontium manganate and lanthanum chromite[11].

Figure 6.18 shows the Raman spectra of $LaGdO_3$ fired at varying temperatures of 1350, 1400 and 1450 °C. It can be seen that there is a great similarity between the profiles and it appears there is little change in the structure with firing temperature within this range. Above 1000 cm^{-1} there is a distinctive broad intense band profile in the spectra, which is likely due to fluorescent/luminescent bands.

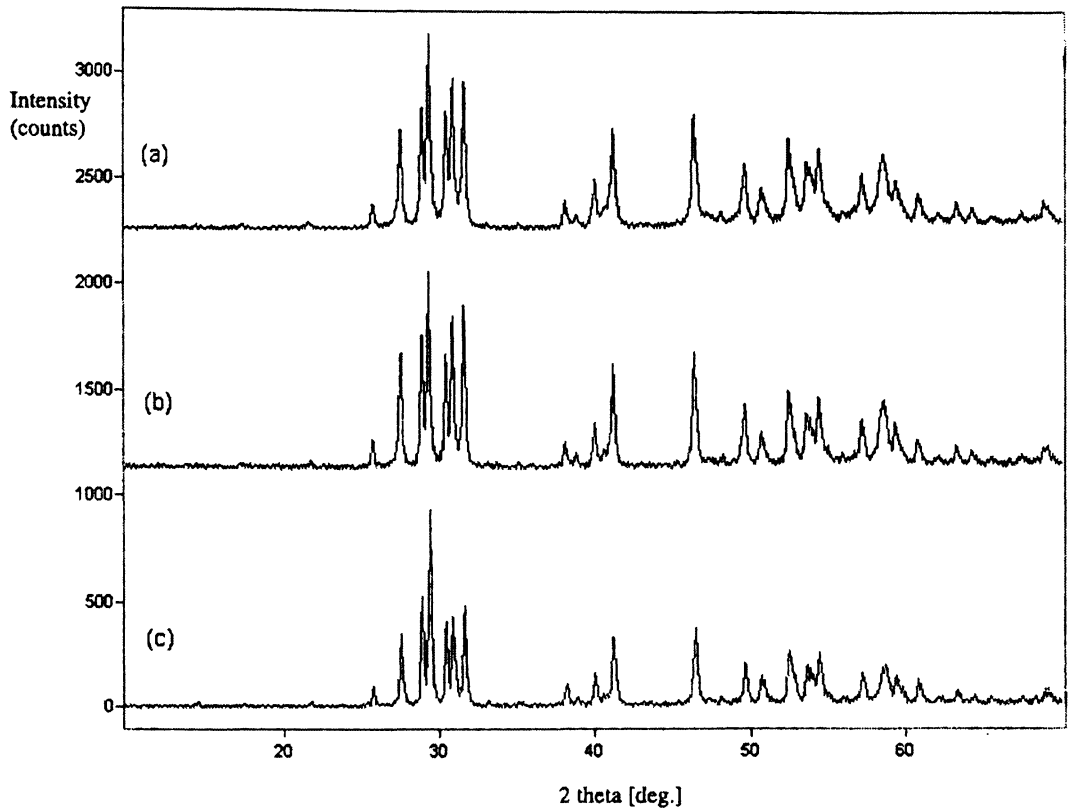

Figure 6.16. X-Ray diffraction patterns of $LaGdO_3$ prepared by sintering at various temperatures (a) 1350°C (b) 1400 °C and (c) 1450 °C.

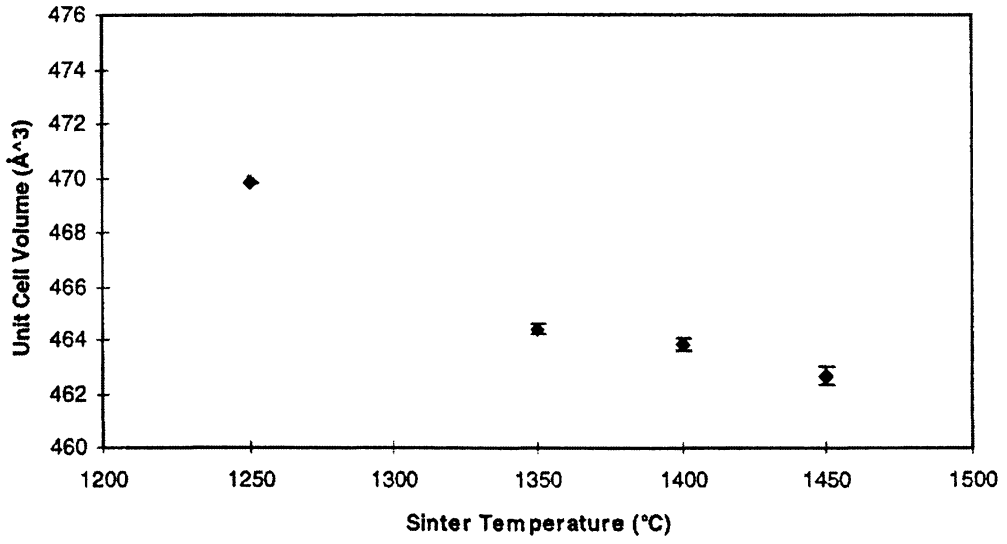

Figure 6.17. Comparison of Unit cell volume ($Å^3$) for $LaGdO_3$ versus sintering temperature (°C). Note that error bars are only given for samples prepared for this thesis.

Table 6.5. Cell parameters calculate for $LaGdO_3$ sintered at various temperatures

Sintering Temperature (°C)	Time (h)	Structure	Cell Parameters a (Å)	b (Å)	C (Å)	Cell Volume ($Å^3$)
1250 (4.0Gpa)[8]	0.5	B-type	14.374	3.697	8.990	469.795± no value
1350	6	B-type	14.3864	3.6686	8.9507	464.392± 0.1903
1400	6	B-type	14.3840	3.6654	8.9492	463.8555 ±0.2057
1450	6	B-type	14.3673	3.6616	8.9450	462.6506 ±0.3485

The structure of $LaGdO_3$ has been determined as B-type rare earth oxide solid solution. Little data exists on the Raman of this material, however, the Raman spectra of both La_2O_3 and Gd_2O_3 are well known[12,13]. Factor group analysis has been determined for these two structures and La_2O_3 is an A-type rare earth oxide with a hexagonal structure and space group P-*3ml*. The following is the irreducible representation for the hexagonal structure, where Γ_{op} is the optical vibrational modes and Γ_{ac} is the acoustic modes.

R: Raman active, ir: Infrared active, i: inactive

P-*3ml* (No. 224)

$$\Gamma_{op} = \underset{(R)}{2A_{1g}} + \underset{(R)}{2E_g} + \underset{(ir)}{2A_{2u}} + \underset{(ir)}{2E_u}$$

$$\Gamma_{ac} = A_{2u} + E_u$$

A total of 4 Raman active, 4 infrared active and no inactive or coincident modes.

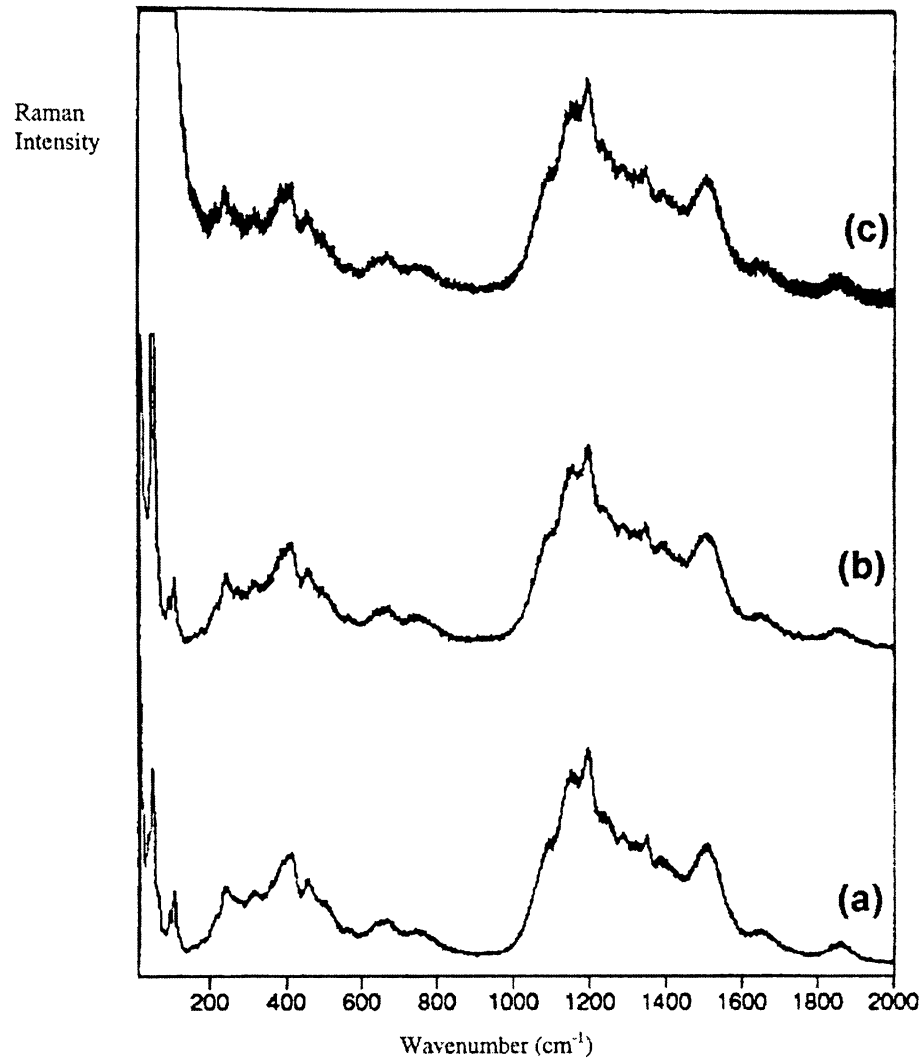

Figure 6.18. Comparison of Raman Spectra of $LaGdO_3$ prepared by sintering at various temperatures (a) 1350°C (b) 1400 °C and (c) 1450 °C.

Gd_2O_3 is a B-type rare earth oxide with a monocline structure and space group C2/*m*. The follow is the irreducible representation for monoclinic structure, where Γ_{op} is the optical vibrational modes and Γ_{ac} is the acoustic modes.

R: Raman active, ir: Infrared active, i: inactive

C2/*m* (No. 12)

$\Gamma_{op} = 14A_g + 7B_g + 7A_u + 14B_u$

(R) (R) (ir) (ir)

$\Gamma_{ac} = A_u + B_u$

A total of 21 Raman active, 21 infrared active and no inactive or coincident modes.

$LaGdO_3$ is reported as having a B-type rare earth oxide structure[14], therefore, the irreducible representation is assumed to be the same as that calculated for B-Gd_2O_3.

Figure 6.19 shows the comparison of Raman spectrum of $LaGdO_3$ (sintered at 1450 °C) at both room temperature (27 °C) and low temperature (-196 °C). Table 6.6 lists the observed band positions and they are compared to those observed for La_2O_3 and Gd_2O_3. At low temperature the spectrum between 25 and 1000 cm^{-1} is relatively simpler than that observed at room temperature (27 °C). A total of 18 bands are identified at low temperature and broad bands at 643, 665 and 747 cm^{-1} are not present in the spectrum at low temperature. These broad bands may be due to fluorescent transitions. The band positions of $LaGdO_3$ match closely to those reported[12] for Gd_2O_3 and on this basis the assignment of modes to observed bands for $LaGdO_3$ at low temperatures (-196 °C) is made. The three distinctive bands reported[13] for the Raman spectrum of hexagonal La_2O_3 phase are not observed in the spectrum of $LaGdO_3$.

Figure 6.20 shows the comparison of the same spectra from Figure 6.19 in the region 1000-2000 cm^{-1} and Table 6.6 lists the band positions of the fluorescent/luminescent bands observed. These bands appear sharper and more resolved in the spectrum at low temperature (Figure 6.19). These bands are assigned to fluorescent or luminescent modes as observed by Kjerulf-Jensen et al.[15] for yttria doped zirconia. These are attributed to electronic transition due to trace rare earth impurities present in the material.

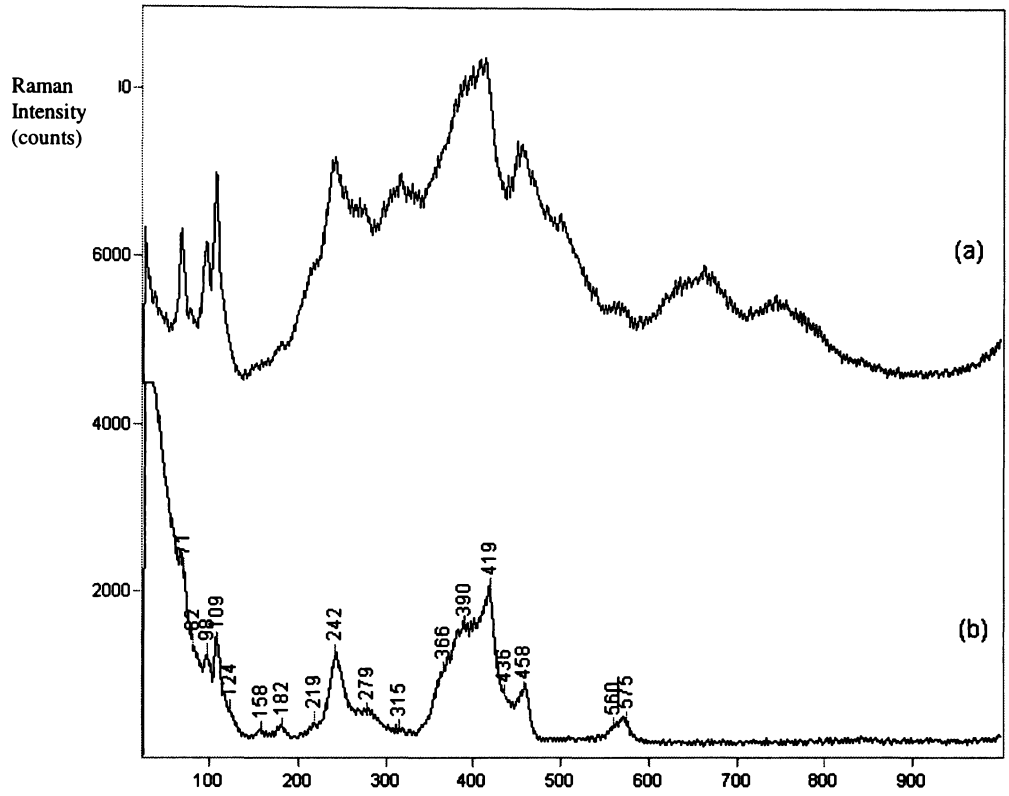

Figure 6.19. Raman Spectra of $LaGdO_3$ sintered at 1450 °C at (a) room temperature 27 °C and (b) –196 °C.

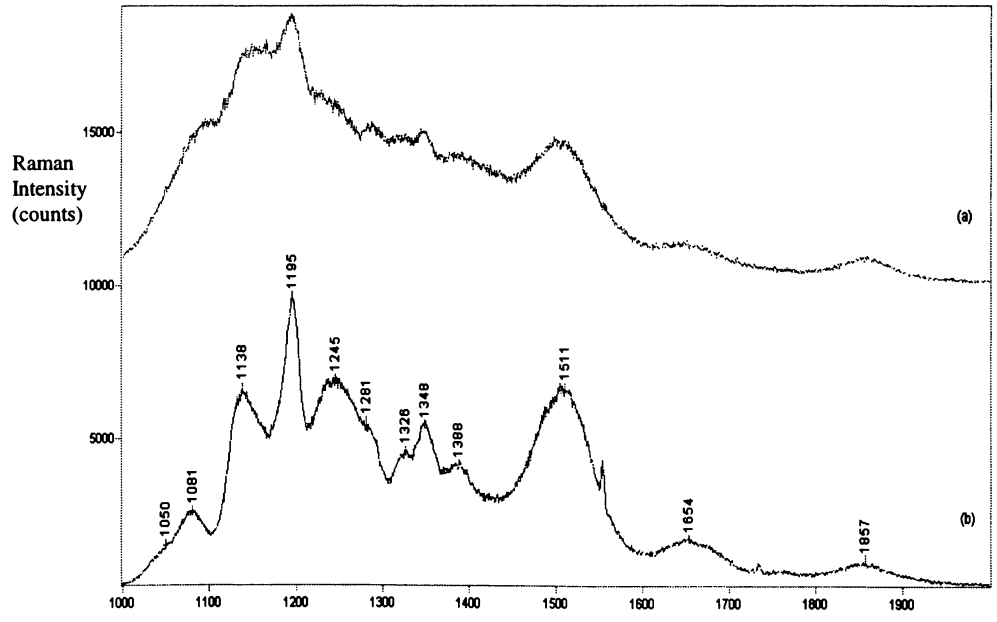

Figure 6.20. Raman Spectra of $LaGdO_3$ sintered at 1450 °C at (a) room temperature 27 °C and (b) –196 °C in the fluorescent band range 1000-2000 cm^{-1}.

Table 6.6. Raman Band positions (cm^{-1}) of $LaGdO_3$ sintered at various temperatures compared to that of La_2O_3 and Gd_2O_3.

Table 6.6. Raman Band positions (cm^{-1}) of $LaGdO_3$ sintered at various temperatures compared to that of La_2O_3 and Gd_2O_3.

$LaGdO_3$	[This work]	Gd_2O_3		Mode[13]	La_2O_3[14]
-194 °C	27 °C	-239 °C	27 °C	Assignment	RT
71 w	69 m	70	71 s	B_g	
82 sh	79 w	85	84 m	A_g	
98 w	97 m	99	98 vs	B_g	
109 m	108 m	110	109 vs	A_g	107 (E_g)
	116 sh	116	115 w	B_g	
124 sh	124 s	123		A_g	
158 w	155 w	156	~150 vw	A_g	
182 w	179 w	176	176 w	A_g	195 (A_{1g})
219 sh	216 sh	220	218 w	A_g	
242 s	241 m	257	256 mw	A_g	
279 w	273 sh	269	269 m	A_g	
315 w	316 b	302	299 m	B_g	
366 sh	366 sh	383	387 m	A_g	
390 b,s	388 sh	386	385 m	B_g	
419 vs	414 s,b	417	416 s	B_g (+A_g ?)	410(A_{1g},E_g)
		430	427 m	B_g	
436 sh	456 s,b	445	442 s	A_g	
458 m	469 sh	484	483 m	A_g	
	501 sh				
560 sh		583	~580 sh	A_g	
575 w	568 b,w	593	590 w	A_g	
	643 sh				
	665 m,b				
	747 m,b				

Key: vw = very weak, w = weak, m = medium, s = strong, vs = very strong, b = broad intensity and sh = shoulder

Table 6.7. Fluorescent band positions observed for $LaGdO_3$ in the range 1000-2000 cm^{-1}

Temperature (°C)	Fluorescent Bands (cm^{-1})
-194	1041, 1081, 1137, 1243, 1280, 1325, 1348, 1387, 1509, 1658, 1676, 1760, 1855
27	(643, 665, 747) 1097, 1119, 1194, 1230, 1246, 1285, 1318, 1384, 1506, 1651, 1856

6.5 Conclusions

6.5.1 $LaGaO_3$ based material

XRD and Raman spectroscopy has been used to characterise the electrolyte materials $La_{1-x}Sr_xGaO_{3-\delta}$ (x = 0-0.2) and $LaGa_{1-y}M_yO_{3-\delta}$ (y = 0-0.2, M = Cr, Mg). XRD of $La_{1-x}Sr_xGaO_{3-\delta}$ (x = 0-0.2) showed the secondary phase of $SrGa_3O_7$ at >5 mol% Sr. The cell deforms with increasing Sr dopant concentration. In the XRD patterns of $LaGa_{1-y}Cr_yO_{3-\delta}$ (y = 0-0.2) the cell also deforms with increasing Cr dopant concentration. The peak at ca. 32° shows a second peak at 32.37°, likely to be due to a phase change, since the peaks do not alter in relative intensity with increase in dopant concentration (above x = 0).

$LaGa_{1-y}Mg_yO_{3-\delta}$ (y = 0-0.2) showed, from the powder X-ray diffraction pattern, the formation of the secondary phase of $La_4Ga_2O_9$ at >5 mol% Mg.

Raman spectra of $LaGaO_3$ showed 18 features at room temperature, and 14 at –196 °C with the disappearance of the band at 92 cm^{-1}. Raman spectra of the doped material, $LaGa_{1-y}Mg_yO_{3-\delta}$ at y = 0-0.2 showed the formation of a secondary phase of

$La_4Ga_2O_9$ with bands at 243, 295 and 356 cm^{-1} which become more predominant at 20 mol% Mg.

6.5.2 $LaFeO_3$ based material

$LaFeO_3$ was prepared using a reverse-strike coprecipitation method. The Raman spectrum of $LaFeO_3$ were obtained at both low-temperature and room temperature, with 9 bands observed of a predicted 24 Raman active modes. Mode assignment is determined from comparison of the Raman profile and band position with perovskites with the same structure, namely, $SmAlO_3$ and $LaGaO_3$ and are as follows: 102 (B_{1g}), ca.140 (B_{2g}), 150 (B_{1g}), 176 (A_g), 227 (B_{3g}), 261 (A_g), 289 (A_g), 413 (A_g), 429 (B_{3g}).

$LaFe_{1-x}Mg_xO_3$ was prepared using a reverse-strike coprecipitation method. The XRD patterns obtained at room temperature showed single phase, but also included small amounts of impurity of La_2O_3 and La_2MgO_x. Lattice calculations based on $FeLaO_3$ showed that Mg dopant concentration had a minor effect on the overall unit cell volume, with the minimum volume achieved being 241.68Å^3 at 1450°C, 15%Mg concentration.

In summary, Mg-doped $LaFeO_3$ produced a single phase material in the range 0-20 mol% Mg as observed from X-ray diffraction. However, a small amount of impurities in each of the samples was observed, containing La_2O_3 and La_2MgO_x. The presence of the impurities suggests that an extra calcination step be included in the processing of the material.

6.5.3 $LaGdO_3$

$LaGdO_3$ was fabricated using reverse strike co-precipitation method and sintered at temperature of 1350, 1400 and 1450 °C. X-ray diffraction showed the presence of a single monoclinic phase. Raman spectroscopy showed a spectrum similar for that

reported for the B-type rare earth oxide Gd_2O_3 and the band positions of the low temperature Raman spectrum were assigned in comparison with this. A total of 18 bands were identified. Intense broad profile in the region 1000-2000 cm^{-1} was observed for $LaGdO_3$, likely due to fluorescent/luminescent bands.

6.6 References

[1] T. Ishihara, H. Matsuda and Y. Takita, *Solid State Ionics* 1995, **79**, 147

[2] T. Ishihara, H. Matsuda and Y. Takita, *J. Am. Chem. Soc.*, 1994, **116,** 3801

[3] N.M. Sammes, G. A. Tompsett, R. J. Phillips, A. M. Cartner, *Solid State Ionics*, 1998, **111**, 1

[4] J. Drennan, V. Zelizko, D. Hay, F.T. Ciacchi, S. Rajenran, S.P.S. Badwal, Ceramic Fuel Cells Limited, Internal Report, July 1996

[5] M.C. Saine and E. Husson, *Spectrochim. Acta*, 1984, **40A,** 733

[6] S. Geller and E.A. Wood, *Acta Cryst.*, 1956, **9,** 563

[7] G.A.Tompsett, N.M. Sammes and A.M. Cartner, *Solid State. Commun.*, [submitted], 1998

[8] Y. Wang, Z. Quin, X. Li, X. Ma, J. Zhou, D. Wu and W. Wenhui, *Jilin Dauxue Ziran Kezue Xuabao*, 1987, 3, 63

[9] W. Su, D. Wu, X. Li, X. Ma, J. Zhou, Z Qian, Y. Wang, W. Liu & Z. Ge, Physica 1986, **139 & 140B**, 658

[10] U. Brendt, D. Maier & C. Keller, J. Solid State Chem., 1975, **13**, 131

[11] R. W. Berg, M. M> Anderson & N. J. Bjerrum, *in Proceedings for the 2nd European Solid Oxide Fuel Cell Conference*, (Ed. B. Thorstensen), Ulf Bossell, Uberrohrdorf, Switzerland, 1996, 413

[12] J. Zarembowitch, J. Gouteron & A.M. Lejus, J. Raman Spectrosc. 1980, **9**, 263

[13] S. I. Boldish & W. B. White, Spectrochim. Acta, 1979, **35A**, 1235

[14] E. M. Levin, C.R. Robbins & H. F. McMurdie, 'Phase Diagrams for Ceramists' (Ed. M. K. Reser), The American Ceramic Society, Ohio, USA, 1964, 134

[15] N. Kjerulf-Jensen, R. W. Berg & F. W. Poulsen, *in Proceedings for the 2nd European Solid Oxide Fuel Cell Conference*, (Ed. B. Thorstensen), Ulf Bossell, Uberrohrdorf, Switzerland, 1996, 647

Chapter Seven

Results and Discussion on Protonic Conductors

7.1 Introduction

Outlined in this chapter are the results and discussion relating to the perovskite proton conductors $SrCe_{1-x}Y_xO_{3-\delta}$ (where x=0.025, 0.05, 0.075, 0.1, 0.15 and 0.2 and where $\delta = x/2$) and $Sr_{0.995}Ce_{0.95}Y_{0.05}O_{2.975}$.

$SrCeO_3$-based ceramic electrolytes have been extensively investigated both electrically and structurally, due to the interest in their proton conducting properties[1-3]. $SrCeO_3$-based ceramics are not the best proton conductors available at the moment ($BaCe_{0.8}Gd_{0.2}O_{3-\delta}$ = 1.0 $x10^{-1}$ S/cm at 1000 °C in a hydrogen gas atmosphere[4], versus $SrCe_{0.95}Yb_{0.05}O_{3-\delta}$ = 9.3 x 10^{-1} at 1000 °C in the same atmosphere, see Figure 2.4), they are however, the proton conductors that exhibit the highest t_{prot} (see Chapter 2 section 2.6.1), while still maintaining a high enough protonic conduction to be commercially viable[1]. They have a conductivity greater that 10 $mScm^{-1}$ at 600-900 °C[5]. Fuel cells based on $SrCe_{0.95}Yb_{0.05}O_{2.975}$[6] have been fabricated and have been reported to be stable under standard operating conditions. However, a full understanding of the electrical responses of the material under varying conditions (namely varying P_{O_2} and P_{H_2O}) for differing dopant concentrations has still not been achieved. It is hoped that a full understanding of the mechanisms and responses of a structure such as $Sr_{1-y}Ce_{1-x}Y_xO_{3-\delta}$ might lead to a computational model that could be applied to other materials in the search for the optimal fuel cell electrolyte material[7].

By changing the Y_2O_3 dopant concentration on the B-site of $SrCeO_3$, and studying each new variation of the material under the same standard conditions, it is hoped that *n*-type, *p*-type and ionic components of the total conductivity can be separated and identified. The response of each component to changing dopant concentration can then be verified and assigned to a conduction mechanism.

In addition to this, varying the dopant concentration of $SrCe_{1-x}Y_xO_{3-\delta}$ will also effect the structure of the material. One of the requirements of an electrolyte for a fuel cell is high density, in order to ensure that the conduction across the electrolyte is by conduction and not diffusion through hollow pathways.

The first objective of this chapter is to study the X-ray diffraction patterns of $SrCe_{1-x}Y_xO_{3-\delta}$ (where x=0.025, 0.05, 0.075, 0.1, 0.15 and 0.2) and $Sr_{0.995}Ce_{0.95}Y_{0.05}O_{2.975}$ to show the effect of varying Y_2O_3 dopant concentration on the unit cell volume and calculated and theoretical density, and to compare the effect of substoichiometry on the material when x = 0.05 and the concentration of Sr^{2+} is reduced.

The second objective of this work is to study the electrical response of the same materials over two temperatures, two differing P_{H_2O} atmospheres and a range of differing P_{O_2} atmospheres (as outlaid in Chapter 4, Table 4.2) in order to separate the total conductivity into its constituent elements, namely, *n*-, *p*- and ionic- type conductivity.

7.2 Structural Investigations

7.2.1 Unit Cell Volume (UCV) Study

Powdered samples (see Table 4.1) were scanned using room temperature X-ray diffraction, as described in Chapter 4, section 4.2.1. Unit cell dimensions were then determined by the least squares method included in the Visual-X^{pow} Stoe software,

which allowed for adjustment of a zero-shift in 2 theta (typically below 0.02 degrees). X-ray diffraction was used to confirm that the materials were single phase and then used to calculate the lattice constants of the materials (as explained in chapter 5, section 5.4), which all have an orthorhombic *Pnma* (No 62) structure. Figure 7.1 shows the calculated unit cell volume (UCV) of undoped $SrCeO_3$[8,9], 15% Y_2O_3-doped $SrCeO_3$[10], both taken from the literature, and Y_2O_3-doped $SrCeO_3$ from X-ray data obtained in the present study. Three main features are worth noting:

- The three UCV determinations for undoped $SrCeO_3$ differ by almost 0.6 $Å^3$. This is above the experimental uncertainties of the quoted high resolution X-ray[8] and neutron work[10] and can most likely be ascribed to slight deviations in A/B-ratio of the three systems.
- From x=0.025 to x=0.20 a linear decrease of unit cell volume is observed. The effective ionic radius, r, of Y^{3+} is 0.90 Å according to the tabulation of Shannon[11], compared to 0.87 Å for Ce^{4+}, for both ions in a 6-fold co-ordination. The fact that the lattice contracts when cerium is replaced by a slightly larger ion can only be interpreted as a result of tilting, or more efficient packing of the B-O octahedra, and/or relaxation of the ions around the oxygen vacancies introduced by doping. A similar study on $BaCe_{1-y}Nd_yO_{3-y/2}$[12] also showed a decrease in the unit cell volume from y=0 to y=0.12, although, in this case, the mismatch between Nd^{3+} (r=0.983Å) and Ce^{4+} is even larger.
- The linear relationship, extrapolated back to x=0, is clearly 0.6 to 1.2 $Å^3$ below the three determinations for undoped $SrCeO_3$.

One may speculate about the reason for the latter discrepancy. Given that no change in space group occurs upon doping[9,10,12], the observed variation could be due to ordering of the Y_2O_3-dopant. It could also be due to substitution of a small amount of Y^{3+} on the A-site, accompanied by evolution of a small amount of a Sr-rich phase. The ionic radius of Y^{3+} is available only for co-ordinations of 5 to 9[11], not 12, observed for the perovskite A-site. Extrapolation from the available data indicates that the ionic radius of Y^{3+} in 12-fold co-ordination would be 1.25 Å, well below that of Sr^{2+} (1.44 Å) in the same co-ordination. Thus, it may be inferred that substitution of Y_2O_3 on the A-site will reduce the unit cell volume. To clarify these effects,

further studies are required at doping levels below 2 mol%. However, it should be noted that no cross-substitution effects have been revealed by careful neutron diffraction studies on several doped cerate systems[9,10,12].

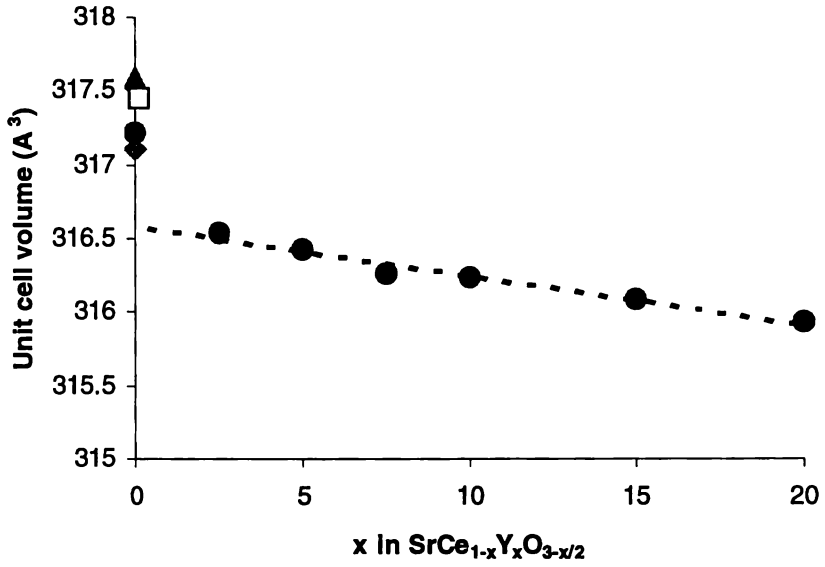

Figure 7.1. Plot of unit cell volume (Å^3) versus x in $SrCe_{1-x}Y_xO_{3-\delta}$. ●:this study, ●neutron diffraction[10], ♦:high-resolution Neutron [9], ▲:powder XRD[8], :powder XRD[12].

7.2.2 Density Studies

Theoretical density calculations were undertaken using the theory explained in chapter 5, section 5.4. Theoretical density calculations using the X-ray data described above show a decrease in density with Y_2O_3 content which may be attributed to a distortion of the unit cell, as shown in Figure 7.2. Figure 7.3 shows the relative density for the samples prepared in this study; this is low for $0.05<x\leq0.15$, according to the requirements for ceramic fuel cell electrolytes (see chapter 3, section 3.2.4(b)). The system also shows a small drop in relative density at

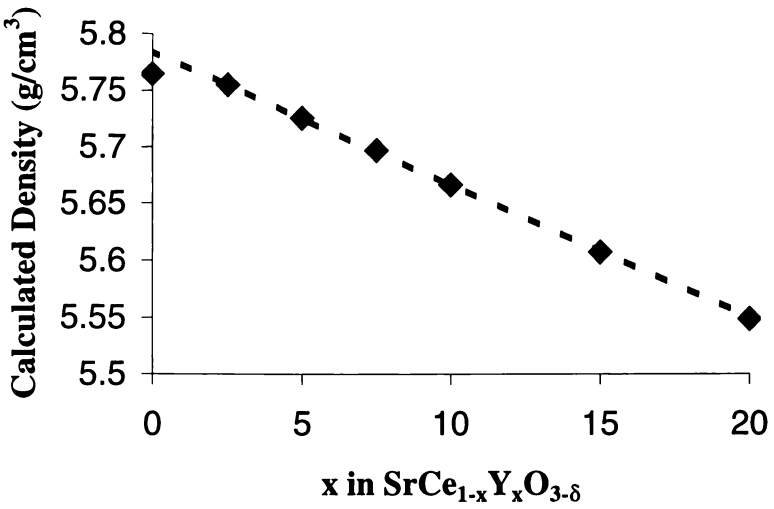

Figure 7.2. Plot of calculated density (g/cm^3) versus x in $SrCe_{1-x}Y_xO_{3-\delta}$.

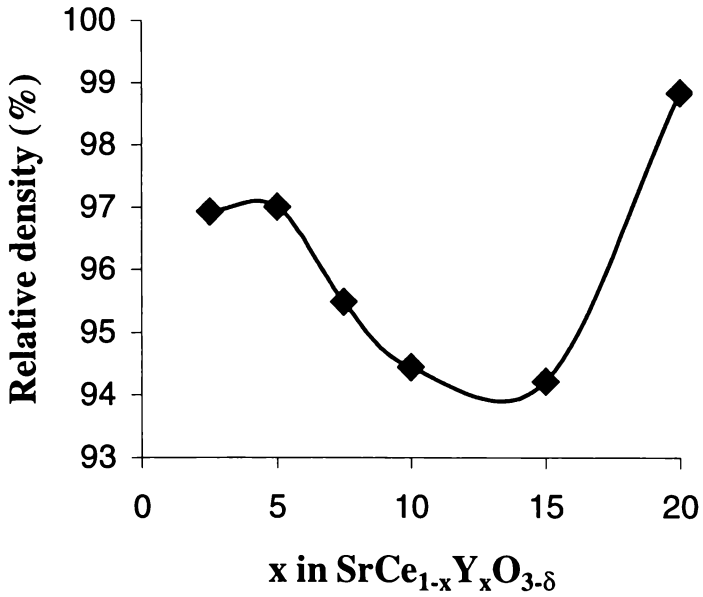

Figure 7.3. Plot of measured relative density versus x in $SrCe_{1-x}Y_xO_{3-\delta}$.

$SrCe_{0.975}Y_{0.025}O_{2.9875}$, moreover this sample is atypical in colour, being orange, unlike the compositions with $x \geq 0.05$, which were greyish-green.

7.3 Electrical Studies

The conductivities of $SrCe_{1-x}Y_xO_{3-\delta}$ samples were measured as a function of the partial pressure of oxygen (P_{O_2}=1 to 10^{-25} atm.) at 600 and 800 °C, and at water vapour pressures of P_{H_2O}=0.01 and 0.001 atm. Comparison with earlier measurements at lower temperatures, where grain and grain boundary relaxations could be resolved[13], indicated that the total conductivity at higher temperatures was essentially the bulk conductivity. The results were analysed according to equation (2.7) to distinguish the various conductivity components. Corresponding results for $Sr_{0.995}Ce_{0.95}Y_{0.05}O_{2.975}$ have been reported[13], which indicated the existence of an ionic conductivity component, independent of P_{O_2}, and two further components, designated *p*- and *n*-type electronic on the basis of their P_{O_2}-dependencies. A similar conclusion was reached with the Yb_2O_3-doped analogue[14]. However, according to Ahlgren[15], thermoelectric power studies of $SrCe_{0.95}Y_{0.05}O_{2.975}$ did not show any indication of *n*-type conductivity, and recent studies of $Sr_{0.995}Ce_{0.95}Y_{0.05}O_{2.975}$[7] have shown that the conductivity component appearing at low P_{O_2} displays an H/D isotope effect and, therefore, should be re-assigned to protonic. Accordingly, in this thesis, the component appearing at low P_{O_2} has been provisionally been given the subscript "*q*" rather than "*n*".

7.3.1 Electrical studies of $SrCe_{1-x}Y_xO_{3-\delta}$ at 800 °C and P_{H_2O} = 0.01 atm.

Typical plots of electrical conductivity, determined as a function of P_{O_2} at T=800 °C and P_{H_2O}=0.01 atm. are shown in Figure 7.4a and 7.4b. Figure 7.4a shows a typical set of data covering the range of P_{O_2}=1 to $1x10^{-25}$atm. for $SrCe_{0.9}Y_{0.1}O_{2.95}$, while Figure 7.4b shows similar data for $SrCe_{0.85}Y_{0.15}O_{2.925}$. The solid lines on each figure

are fits to equation (2.7), in which the exponents in the P_{O_2} dependencies of *p*-type and *q*-type conductivity were constrained to ¼ and –¼ respectively.

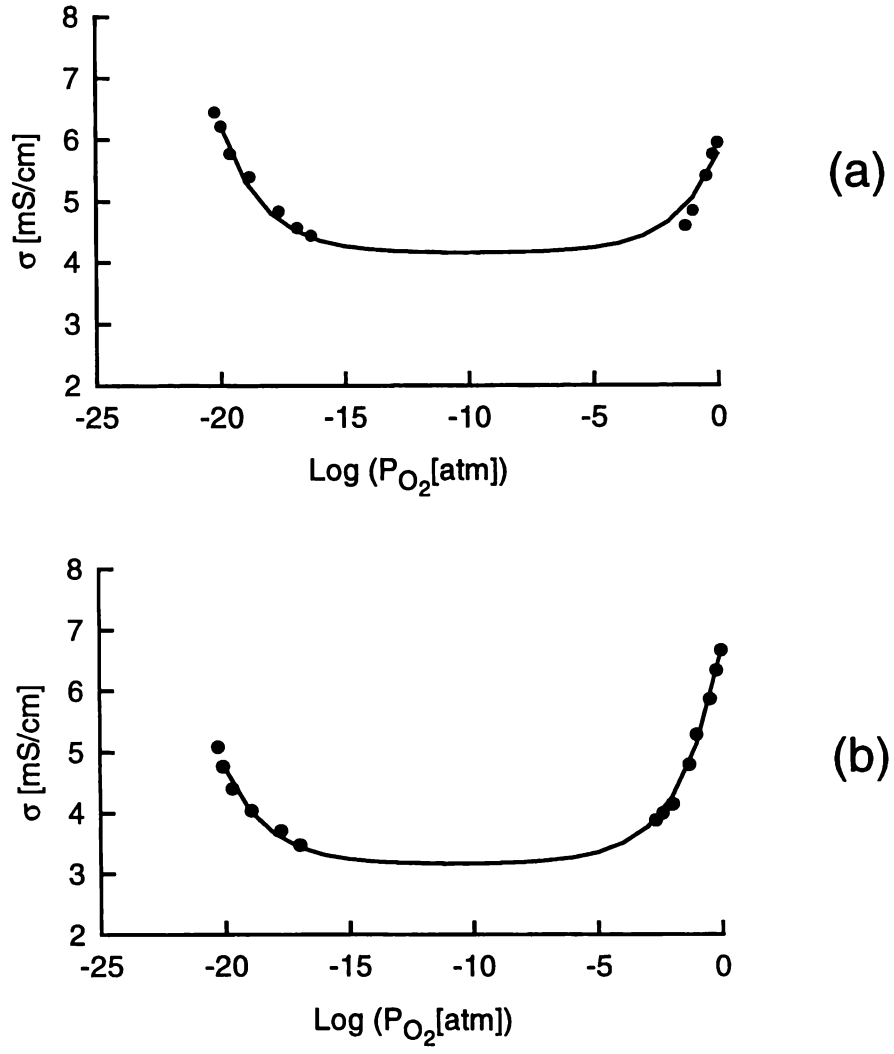

Figure 7.4: Plot of conductivity versus PO_2 at T=800 °C and P_{H_2O}=0.01 atm. for (a) $SrCe_{0.9}Y_{0.1}O_{2.95}$ and (b) $SrCe_{0.85}Y_{0.15}O_{2.925}$.

The results give conductivity contributions from each component. Inspection of equation (2.7) shows that parameters σ_p and σ_q have the physical meaning of the

respective conductivities extrapolated to a partial pressure of 1 atm. as shown by Figure 2.3.

At 800 °C and P_{H_2O}=0.01 atm., these results were corrected for porosity using equation (2.8) and plotted as each component versus dopant concentration in Figure 7.5a,b,c. As the figure shows, the three conductivity components behave quite differently.

The P_{O_2}-independent ionic component, σ_i (Figure 7.5a), does not vary linearly with the change in doping level, as might be expected from a simple point defect description. Instead, it displays a maximum at x=0.10, where it reaches 5 mS/cm. There is evidence of a threshold for the onset of ionic conductivity at a doping level somewhere below x=0.05. The occurrence of the maximum is not surprising, since this is known to occur in other cerate systems, for example $BaCe_{1-x}Gd_xO_{3-\delta}$ [16]. It should be remembered that the present measurements were made at constant water vapour pressure which, for different doping levels, may correspond to different levels of saturation. The threshold effect, which is more difficult to explain, has also been reported for the related system $SrCe_{1-x}Yb_xO_{3-\delta}$ [6] at lower temperatures, where the conductivity is mainly protonic.

The *p*-type component, σ^o_p (Figure 7.5b), shows the same threshold as the ionic component, but thereafter increases almost linearly with x. This is entirely consistent with the behaviour of σ_i, since both the protonic carriers and the holes are generated from oxide ion vacancies according to rather similar equations (2.2 to 2.4). The fact that σ^o_p shows no maximum can be qualitatively explained by the fact that the holes are minority defects and their behaviour deviates less from the predicted behaviour than that of protons. In other words, the oxygen dissolution equilibrium (eqn. 2.3) is largely displaced to the left-hand side, making the hole concentration

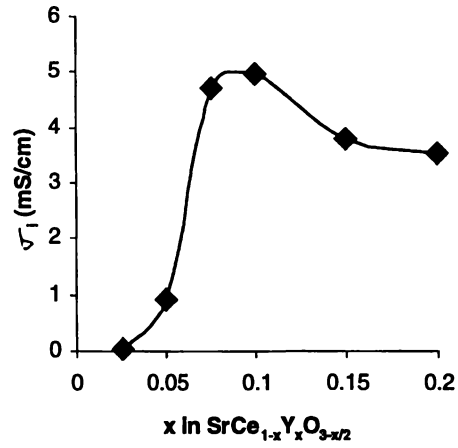

(a)

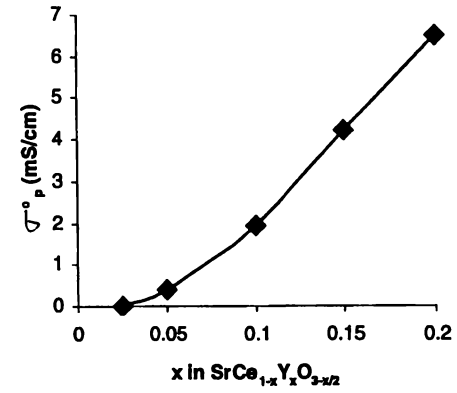

(b)

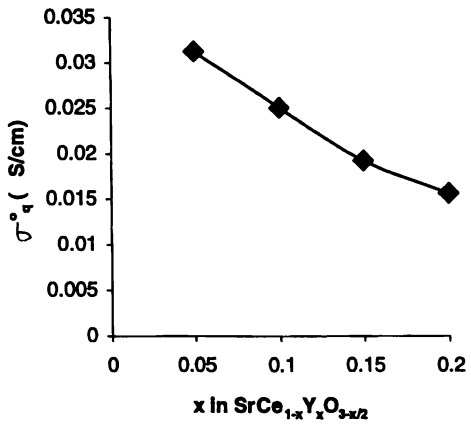

(c)

Figure 7.5: Conductivity parameters, as determined using equation (2.7) for $SrCe_{1-x}Y_xO_{3-\delta}$ versus atomic % of yttrium dopant (x) for (a) ionic, (b), *p*-type and (c) '*q*'-type conductivity at T=800 °C and P_{H_2O}=0.01 atm.

low and therefore less affected by dopant concentration. This conclusion is in agreement with recent defect simulations[7].

The component denoted by "*q*" (Figure 7.5c), displays the opposite behaviour to the *p*-type component, decreasing monotonically with doping level, indicating that it is related to the concentration of electrons. As argued elsewhere[7], this component could be either *n*-type electronic as previously assumed, or protonic due to an excess of protons whose charge is balanced by the electrons. Recent preliminary work[7] showing that this component displays a H/D isotope effect, if confirmed, would indicate that this conductivity is at least partially protonic in nature.

Returning to the apparent threshold effect in doping, two tentative explanations have been offered for this effect[17]. One is that at very low doping levels, the yttrium is concentrated at the grain boundaries and is, therefore, depleted in the bulk of the material; further addition (i.e. increasing Y_2O_3 concentration) of dopant produces the expected increase in conductivity. It has been suggested that doping with aliovalent cations would increase the concentration of charge carriers[18]. For example, substitution of Y^{3+} for Ce^{4+} (Y'_{Ce}) in $SrCeO_3$ would provide oxygen vacancies $V_o^{\bullet\bullet}$ as a result of charge compensation

$$Y^{3+} \rightarrow Y'_{Ce} + \frac{1}{2}V_o^{\bullet\bullet} \qquad (7.1)$$

Electron holes may arise under equilibrium between oxygen vacancies ($V_o^{\bullet\bullet}$) and oxygen gas

$$V_o^{\bullet\bullet} + \frac{1}{2}O_2 \xleftrightarrow{K(7.2)} O_o^x + 2h^{\bullet} \qquad (7.2)$$

Where $h^{\bullet}$ represents an electron hole, O_o^x an oxide ion on a normal lattice site and $K_{7.2}$ is the equilibrium constant for equation 7.2. Therefore, the higher the Y_2O_3 dopant concentration, the more oxygen vacancies formed and, thus, more electron holes present in the material causing an increase in conductivity.

An alternative explanation is partial substitution of Y_2O_3-dopant substitutes equally on the A-and B-sites, which would generate no oxide ion vacancies and therefore no ionic conductivity (protonic or oxide ion). The data presented in Figure 7.5 does not give cause for preferring one or other explanations. On the other hand, a small degree of cross-substitution of Y^{3+} on the A-site would be qualitatively consistent with both the observed discontinuity of the unit cell volume, and the conductivity threshold for ionic and *p*-type components.

7.3.2 Electrical studies of $SrCe_{1-x}Y_xO_{3-\delta}$ at 800 °C and P_{H_2O} = 0.001 atm.

The results for $SrCe_{1-x}Y_xO_{3-\delta}$ at 800 °C and P_{H_2O} = 0.001 atm. were treated in the same manner as those for P_{H_2O} = 0.01 atm. The conductivity results were extrapolated to give the physical meaning of the respective conductivities at a partial pressure of 1 atm. and were corrected for porosity using equation (4.1). Each component was then plotted against dopant concentration as shown in Figure 7.6a,b,c. As this figure shows, the three conductivity components behave quite differently, but in general, follow the same trend as their higher P_{H_2O}=0.01atm. counterparts.

The P_{O_2}-independent ionic component, σ_i (Figure 7.6a), does not vary linearly with the doping level, and remains very close to the same values of those of the higher P_{H_2O} atmosphere. This is consistent with research that has shown that σ_i is independent of P_{H_2O}[18]. Equation 7.2 illustrates the equilibrium that may arise between oxygen vacancies and oxygen gas and the equilibrium constant $K_{7.2}$ may be given by,

$$K_{7.2} = [O_o^x][h^\bullet]^2 / [V_o^{\bullet\bullet}]P_{o_2}^{\frac{1}{2}} \qquad (7.3)$$

illustrating that P_{H_2O} does not effect the equilibrium reaction. Again, there does seem to be a threshold effect, which is consistent with the higher P_{H_2O} values. Given that total conductivity is a linear function of $P_{H_2O}^{1/2}$ at constant P_{O_2}[18], a change from 0.01 to 0.001 atm. of water vapour pressure would cause only a very small resultant change.

The *p*-type component σ^{o}_{p} (Figure 7.6b) shows the same threshold effect as the ionic component but thereafter increases with increasing x. This is entirely consistent with the threshold behaviour of σ_i, as explained for the higher P_{H_2O} series. Also, a decrease in P_{H_2O} has the effect of causing a major increase in the *p*-type component[18]. Comparing Figure 7.6b with Figure 7.5b, it can be seen that there is nearly a four times increase in each value. Figure 2.11 (Chapter 2) shows that a move from 0.01 atm. to 0.001 atm. P_{H_2O} would cause an increase in protonic conduction. As the charge carriers in this oxide are protons and holes, the total conductivity σ_{total} is expressed as $\sigma_{total} = \sigma_H^{\bullet} + \sigma_h^{\bullet}$ (where $\sigma_H^{\bullet}$ = protonic component and $\sigma_h^{\bullet}$ = *p*-type component or hole conduction); an increase in water vapour pressure would cause an increase in *p*-type conduction.

The component denoted by '*q*' (Figure 7.6c), displays the opposite behaviour to the *p*-type component, decreasing monotonically with doping level following Figure 7.5(c) except for that observed for the x=20 at% point, which shows an increase. The decrease in P_{H_2O} from 0.01 to 0.001 atm. seems to have little effect on the '*q*'-type electronic conduction.

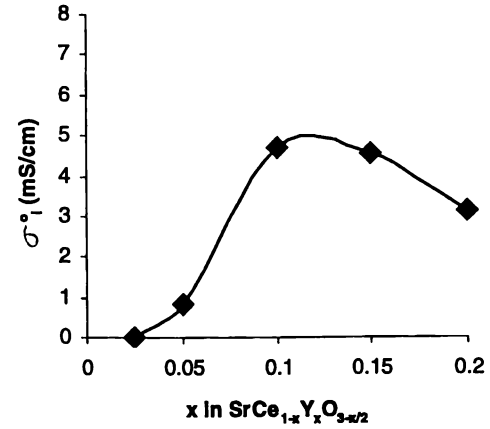

(a)

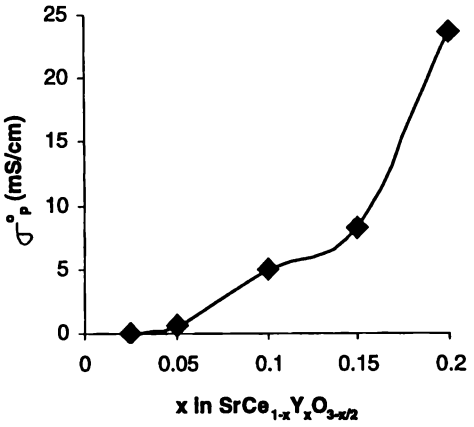

(b)

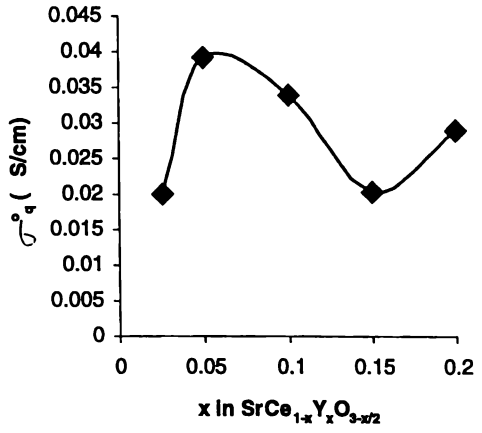

(c)

Figure 7.6 Conductivity parameters, as determined using equation (2.7) for $SrCe_{1-x}Y_xO_{3-\delta}$ versus atomic % of yttrium dopant (x) for (a) ionic, (b), *p*-type and (c) '*q*'-type conductivity at T=800 °C and P_{H_2O}=0.001 atm.

7.3.3 Electrical studies of $SrCe_{1-x}Y_xO_{3-\delta}$ at 600 °C and P_{H_2O} = 0.01 and 0.001 atm.

Studies of $SrCe_{1-x}Y_xO_{3-\delta}$ were incomplete due to erroneous results that lead to unusual curve fitting values. These were discarded and therefore, only a partial set of curves were achieved for the P_{H_2O} = 0.01 and 0.001 atm. at T = 600 °C, (as shown in Figure 7.7), and thus only general comments can be made. Results show an expected drop in all conductivity values, due to higher impedance values at lower temperatures, and the trends shown at higher temperatures for each component appear to hold for the lower temperature of 600 °C.

The P_{O_2}-independent ionic component, σ_i (Figure 7.7a) at P_{H_2O}=0.01 atm. shows an increase in conductivity with increasing doping level. However, with only a few points to compare, any conclusion would be difficult to validate. Also, as one of the set of results is x=2.5 at.%, and as there appears to be a threshold effect under x=5 at.%, these results may be erroneous. Varying from P_{H_2O} = 0.01 to 0.001 atm. does not appear to cause a great variation of σ_i. This is in agreement with research to date, as explained in section 7.3.2.

The *p*-type component σ^o_p (Figure 7.7b) at P_{H_2O} = 0.01 atm. shows a maximum at x=10 at.% doping level, but as with the σ_i component, there are not enough results to draw a valid conclusion. However, comparing these results with the results gained at P_{H_2O}=0.001 atm. shows that overall, there is an increase in *p*-type electronic conductivity with the change from P_{H_2O}=0.01 to 0.001 atm. This trend is also seen in the higher temperature data and is consistent with the current research.

Comparing the component denoted by '*q*' (Figure 7.7c) between P_{H_2O} = 0.01 and 0.001 atm. shows little change in electronic conductivity with changing P_{H_2O}. These results are similar to those observed for the higher temperature values.

7.3.4 Substoichiometric material $Sr_{0.995}Ce_{0.95}Y_{0.05}O_{3-\delta}$

It should be noted that the only substoichiometric material studied, that of $Sr_{0.995}Ce_{0.95}Y_{0.05}O_{2.975}$, showed a drop in unit cell volume of approximately 0.34 $Å^3$ compared to its stoichiometric partner, $SrCe_{0.95}Y_{0.05}O_{2.975}$. Ahlgren et al[13] observed that varying y in $Sr_{1-y}Ce_{0.95}Y_{0.05}O_{3-\delta}$ from 0.990 to 1.005 caused no significant change in the unit cell volume. Given the experimental errors listed in Table 7.1 for the data presented in this thesis, which may be greater because of uncertainty in the indexing of some small peaks, it could be possible that the change in unit cell volume is not significant. Although further research would be needed to clarify this finding, see Chapter 8.

Figures 7.8 and 7.9 show similar results to those presented at T=800 °C and P_{H_2O} = 0.01 and 0.001 atm. The square symbol represents the substoichiometric sample measurements for each component in each graph. It can be seen that these values vary greatly from their stoichiometric partner, $SrCe_{0.95}Y_{0.05}O_{2.975}$. In all cases the conductivity component is higher than the stoichiometric material, except for the '*q*'-type component at P_{H_2O} = 0.001atm.

At 800 °C, the P_{O_2} independent ionic component is much higher than its stoichiometric partner, being approximately 7 mS/cm for both P_{H_2O} levels. The *p*-

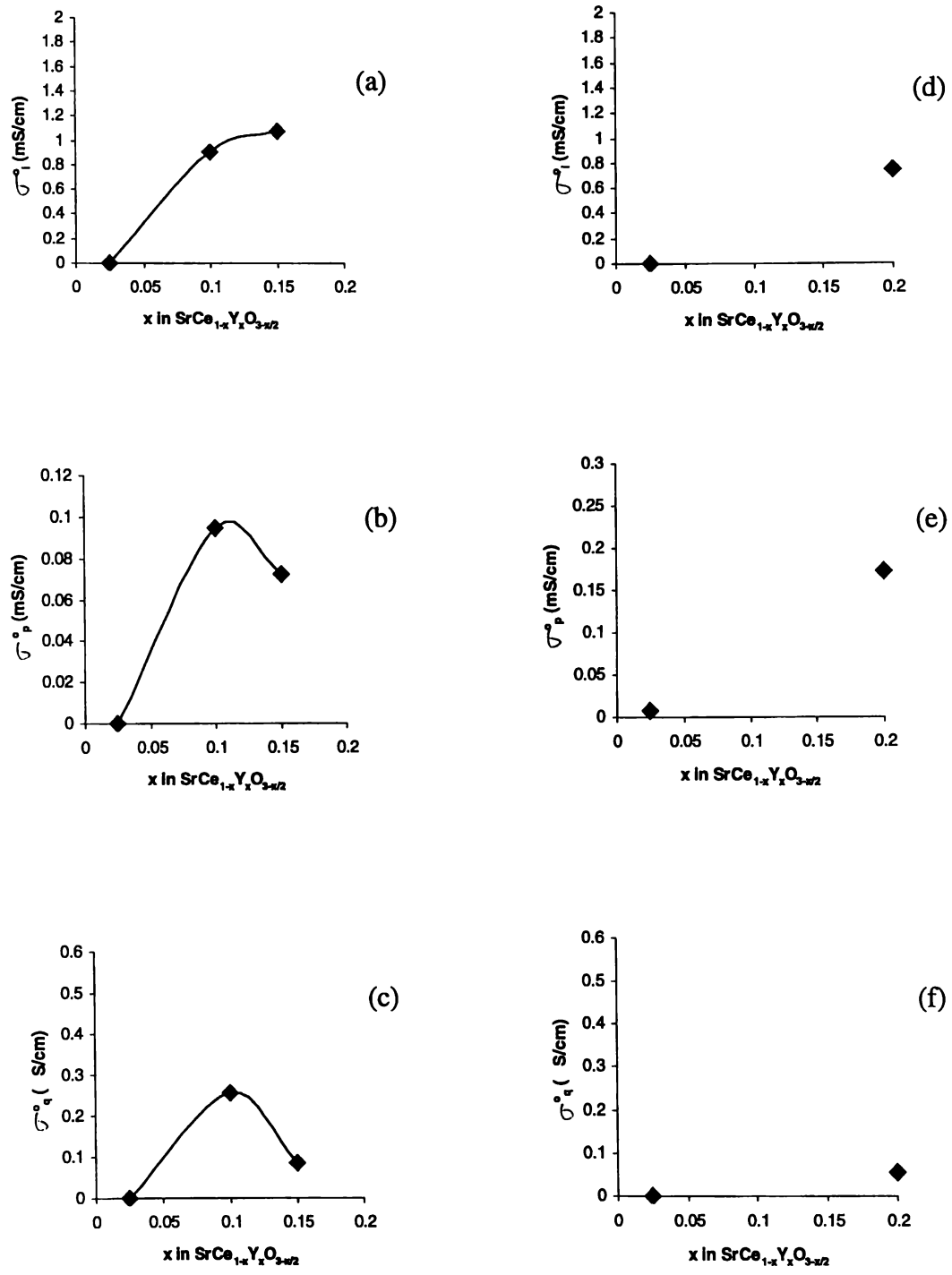

Figure 7.7: Conductivity parameters, as determined using equation (2.7) for $SrCe_{1-x}Y_xO_{3-\delta}$ versus atomic % of yttrium dopant (x) for (a) ionic, (b), *p*-type and (c) '*q*'-type conductivity at T=600 °C and P_{H_2O}=0.01 atm. and (d) ionic, (e), *p*-type and (f) '*q*'-type conductivity at T=600 °C and P_{H_2O}=0.001 atm.

type component, σ^{o}_{p}, is also higher, nearly doubling from 8 mS/cm to 14 mS/cm with decreasing P_{H_2O}. The '*q*'-type component shows a major decrease with decreasing P_{H_2O}, from 0.13 μS/cm to 0.012 μS/cm. However, with such small values, any comparisons become less significant.

Table 7.1 Error values for Unit Cell volume results for $SrCe_{1-x}Y_xO_{3-\delta}$ and $Sr_{0.995}Ce_{0.95}Y_{0.05}O_{3-\delta}$

Y_2O_3 dopant concentration. (mol%)	Unit Cell volume ($Å^3$)	Error ($\pm Å^3$)
2.5	316.55	0.22
5	316.43	0.32
5 (A site substoichiometric)	316.09	0.15
7.5	316.27	0.07
10	316.24	0.11
15	316.09	0.14
20	315.93	0.14

At 600 °C, σ_i shows similar results as observed for T=800 °C, i.e., the trend remains the same, but with lower values at approximately 1.8 mS/cm. The *p*-type component shows an increase with decreasing P_{H_2O}, from 0.07 to 0.26 mS/cm, the same as for T=800 °C, but also decreases in electronic conductivity with the lower temperature. The '*q*'-type component shows little change with decreasing P_{H_2O} and is of course lower than its T=800 °C counterpart.

It has been speculated that the large deviations of each conductivity parameter caused by being substoichiometric on the A-site may be attributed to an increase in defect concentration. Sub-stoichiometry on the A site of an ABO_3 structure may introduce vacancies into the crystal structure, in the same way that doping with a lower valency ion causes vacancies, however, this explanation is unsubstantiated at this point; more

research is required to clarify this effect, see Chapter 8. Also speculated has been the accuracy of the stoichiometry of any give material. There is always slight variations from the 'perfect ABO_3' stoichiometry, and perhaps a lowering of the A site content actually fabricates a material closer to the 'perfect ABO_3' structure than those fabricated in this work.

7.4 Conclusions

Changing the yttrium content in $SrCe_{1-x}Y_xO_{3-\delta}$ affects the electrical and structural properties of the system. Unit cell volume and calculated density decrease with increasing yttrium content. The ionic and p-type component of the conductivity show threshold effect with Y-doping, which may be related to the double substitution of Y on both A- and B-sites. A maximum ionic conductivity of 5 mS/cm is found at 10% Y, whereas p-type conductivity increases with increasing yttrium. A conductivity component appearing at low oxygen partial pressure decreases with yttrium doping.

P_{H_2O}=0.01 atm.

P_{H_2O}=0.001 atm.

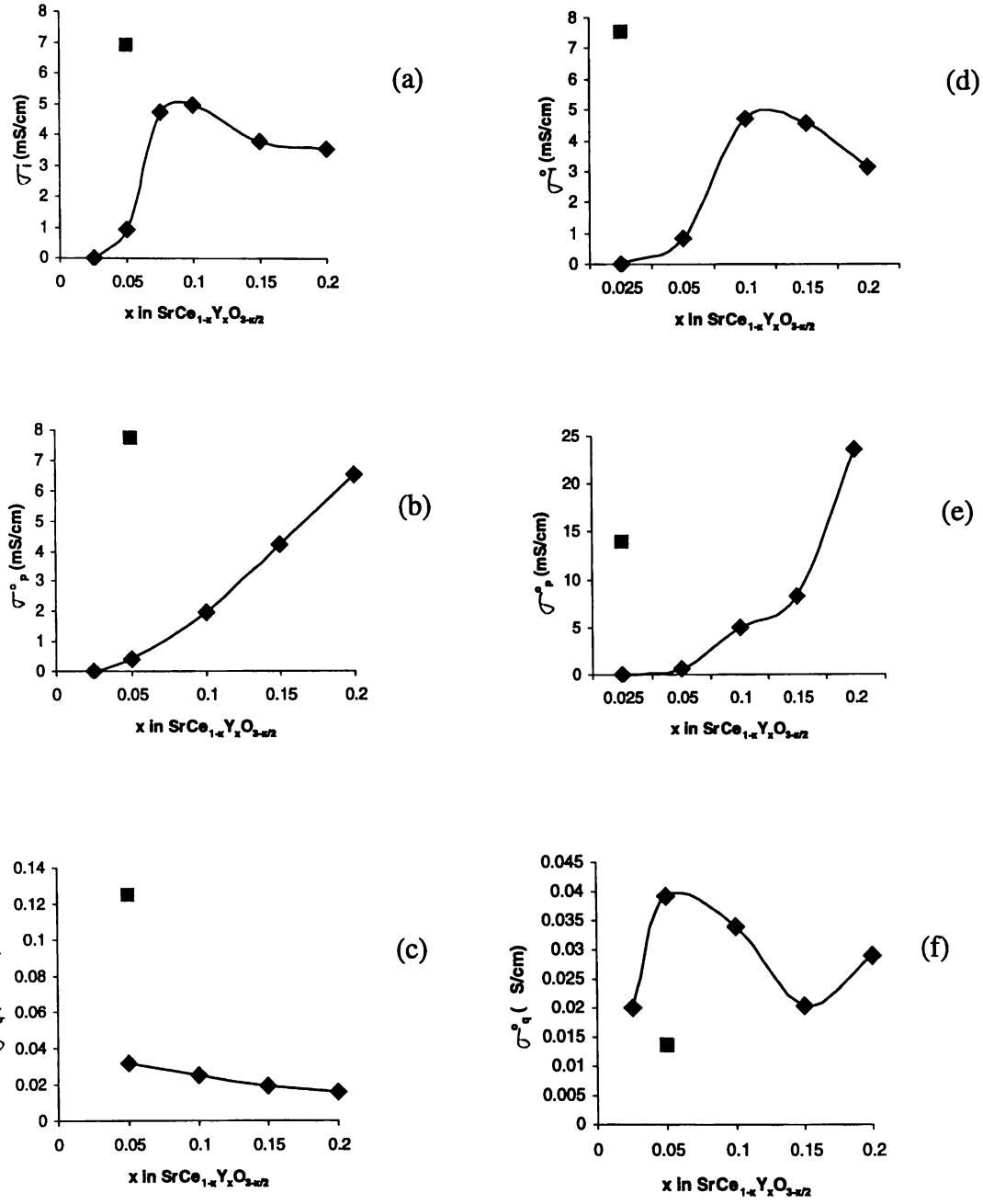

Figure 7.8 Conductivity parameters, as determined using equation (2.7) for $SrCe_{1-x}Y_xO_{3-\delta}$ (♦) versus atomic % of yttrium dopant (x) for (a) ionic, (b), *p*-type and (c) '*q*'-type conductivity at T=600 °C and P_{H_2O}=0.01 atm. and (d) ionic, (e), *p*-type and (f) '*q*'-type conductivity at T=600 °C and P_{H_2O}=0.001 atm. where in each graph the square symbol (■) represents the substoichiometric material $Sr_{0.995}Ce_{0.95}Y_{0.05}O_{3-\delta}$

P_{H_2O}=0.01 atm. P_{H_2O}=0.001 atm.

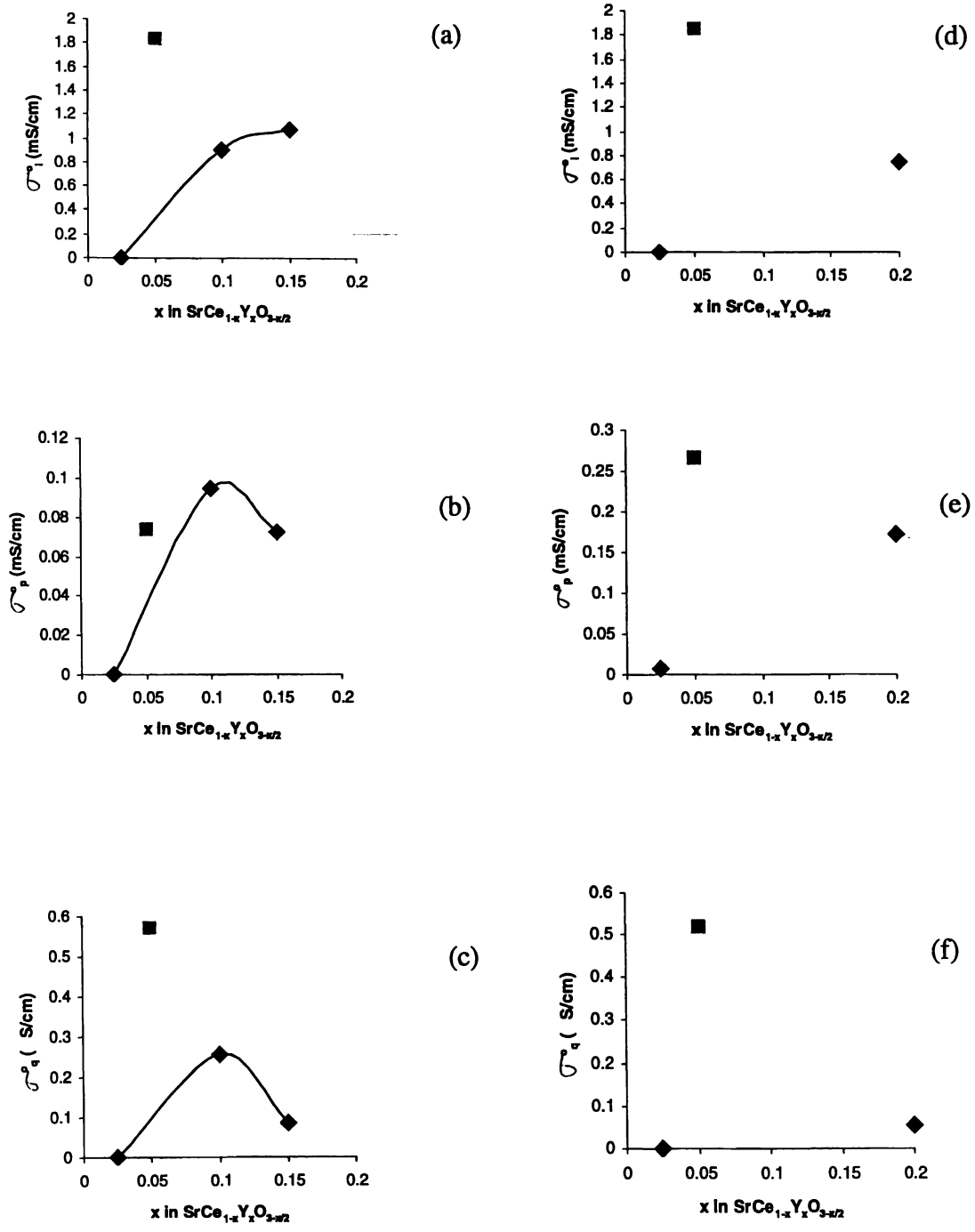

Figure 7.9 Conductivity parameters, as determined using equation (2.7) for $SrCe_{1-x}Y_xO_{3-\delta}$ (♦) versus atomic % of yttrium dopant (x) for (a) ionic, (b), *p*-type and (c) '*q*'-type conductivity at T=600 °C and P_{H_2O}=0.01 atm. and (d) ionic, (e), *p*-type and (f) '*q*'-type conductivity at T=600 °C and P_{H_2O}=0.001 atm. where in each graph the square symbol (■) represents the substoichiometric material $Sr_{0.995}Ce_{0.95}Y_{0.05}O_{3-\delta}$

7.5 References

[1] H. Iwahara, T. Esaka, H. Uchida & N. Maeda, *Solid State Ionics*, 1981, **3/4**, 359.

[2] H. Iwahara, *Solid State Ionics*, 1988, **28-30**, 573.

[3] I. Kosacki & H. L. Tuller, *Solid State Ionics*, 1995, **80**, 223.

[4] H. Iwahara, *Solid State Ionics*, 1996, **86-88**, 9

[5] N. Bonanos, Proceedings on Symposium on Materials Science, edited by F. W. Poulsen et al, Risö, Denmark, 1993, 19

[6] H. Iwahara, H. Uchida & S. Tanaka, *Solid State Ionics*, 1983, **9/10**, 1021

[7] N. Bonanos & F. W. Poulsen, accepted for publication in *J. Mater. Chem*, 1999.

[8] J. Ranløv & K. Nielsen, *J. Mater. Chem*, 1994, **4**, 868.

[9] K. S. Knight & N. Bonanos, *Mat. Res. Bull.* 1995, **30**,347.

[10] J. Ranløv, B. Lebech and K. Nielsen, *J. Mater. Chem.*, 1995, **5**, 743.

[11] R. D. Shannon, *Acta Crystallogr.*, 1976, **A32**, 751.

[12] M. Danelon Mastromonaco, I. Barbariol & A. Cocco, *Ann. Chim.* (Rome) 1969, **59**, 465

[13] E. O. Ahlgren, J. R. Hansen, N. Bonanos, F. W. Poulsen & M. Mogensen, Proc. 17th Risø International Symposium on Materials Science. Editors, F. W. Poulsen, N. Bonanos, S. Linderoth, M. Mogensen and B. Zachau-Christiansen 1996.

[14] I. Kosacki & H. L. Tuller, *Solid State Ionics*, 1995, **80**, 223

[15] E. O. Ahlgren, *Solid State Ionics*, 1997, **97**, 489.

[16] N. Bonanos, B. Ellis, K. S. Knight & N. M. Mahmood, *Solid State Ionics*, 1989, **35**, 179.

[17] J. F. Liu & A. S. Nowick, *Solid State Ionics*, 1992, **50**, 131.

[18] H. Uchida, N. Maeda & H. Iwahara, *Solid State Ionics*, 1983, **11**, 117

Chapter Eight

Conclusions and Recommendations

8.1 Conclusions

8.1.1 $LaGaO_3$ doped material

Powder X-ray diffraction and Raman spectroscopy have been used to characterise the electrolyte materials $La_{1-x}Sr_xGaO_{3-\delta}$ (x = 0-0.2) and $LaGa_{1-y}M_yO_{3-\delta}$ (y = 0-0.2, M = Cr, Mg). XRD of $La_{1-x}Sr_xGaO_{3-\delta}$ (x = 0-0.2) showed the secondary phase of $SrGa_3O_7$ at >5 mol% Sr. The cell deforms with increasing Sr dopant concentration. In the XRD patterns of $LaGa_{1-y}Cr_yO_{3-\delta}$ (y = 0-0.2) the cell also deforms with increasing Cr dopant concentration. The peak at ca. 32° shows a second peak at 32.37°, likely to be due to a phase change, since the peaks do not alter in relative intensity with increase in dopant concentration (above x = 0).

$LaGa_{1-y}Mg_yO_{3-\delta}$ (y = 0-0.2) showed, from the powder X-ray diffraction pattern, the formation of the secondary phase of $La_4Ga_2O_9$ at >5 mol% Mg.

Raman spectra of $LaGaO_3$ showed 18 features at room temperature, and 14 at −196 °C with the disappearance of the band at 92 cm^{-1}. Raman spectra of the doped material, $LaGa_{1-y}Mg_yO_{3-\delta}$ at y = 0-0.2 showed the formation of a secondary phase of $La_4Ga_2O_9$ with bands at 243, 295 and 356 cm^{-1} which become more predominant at 20 mol% Mg.

8.1.2 $LaFeO_3$ based material

$LaFeO_3$ was prepared using a reverse-strike coprecipitation method. The Raman spectrum of $LaFeO_3$ were obtained at both low-temperature and room temperature, with 9 bands observed of a predicted 24 Raman active modes. Mode assignment is determined from comparison of the Raman profile and band position with perovskites with the same structure, namely, $SmAlO_3$ and $LaGaO_3$ and are as follows: 102 (B_{1g}), ca.140 (B_{2g}), 150 (B_{1g}), 176 (A_g), 227 (B_{3g}), 261 (A_g), 289 (A_g), 413 (A_g), 429 (B_{3g}).

$LaFe_{1-x}Mg_xO_3$ was prepared using a reverse-strike coprecipitation method. The XRD patterns obtained at room temperature showed single phase, but also included small amounts of impurity of La_2O_3 and La_2MgO_x. Lattice calculations based on $FeLaO_3$ showed that Mg dopant concentration had a minor effect on the overall unit cell volume, with the minimum volume achieved being 241.68Å^3 at 1450°C, 15%Mg concentration.

In summary, Mg-doped $LaFeO_3$ produced a single phase material in the range 0-20 mol% Mg as observed from X-ray diffraction. However, a small amount of impurities in each of the samples was observed, containing La_2O_3 and La_2MgO_x. The presence of the impurities suggests that an extra calcination step be included in the processing of the material.

8.1.3 $LaGdO_3$

$LaGdO_3$ was fabricated using reverse strike co-precipitation method and sintered at temperature of 1350, 1400 and 1450 °C. X-ray diffraction showed the presence of a single monoclinic phase. Raman spectroscopy showed a spectrum similar for that reported for the B-type rare earth oxide Gd_2O_3 and the band positions of the low temperature Raman spectrum were assigned in comparison with this. A total of 18 bands were identified. Intense broad profile in the region 1000-2000 cm^{-1} was observed for $LaGdO_3$, likely due to fluorescent/luminescent bands.

8.1.4 $SrCeO_3$ doped material

Changing the yttrium content in $SrCe_{1-x}Y_xO_{3-\delta}$ affects the electrical and structural properties of the system. Unit cell volume and calculated density decrease with increasing yttrium content. The ionic and *p*-type component of the conductivity show threshold effect with Y-doping, which may be related to the double substitution of Y on both A- and B-sites. A maximum ionic conductivity of 5 mS/cm is found at 10% Y, whereas p-type conductivity increases with increasing yttrium. A conductivity component appearing at low oxygen partial pressure decreases with yttrium doping.

8.2 Recommendations

Future work should include further characterisation of the Y doped $SrCeO_3$ material by Raman spectroscopy in order to determine the overall structural effect of the A-site substoichiometry. A more in-depth electrical study of the A-site substoichiometric material, by varying y in $Sr_yCe_{0.95}Y_{0.05}O_{3-\delta}$ and studying the effect of varying temperature and P_{H_2O} over a P_{O_2} range would enable ionic, *n*- and *p*-type conductivity to be determined as a function of A-site substoichiometry.

A more complete set of data for $SrCe_{1-x}Y_xO_{3-\delta}$ over both temperature and P_{H_2O} would allow for better understanding of the response of each separate electrical component. The results could be used to allow for the calculation of defect equilibrium equations, and help enhance a model to be used for the simulation of responses of materials under proton conducting conditions, with the prediction of possible new conductors.

Reprocessing of the Mg doped $LaFeO_3$ material with the correct ratio of precipitant to nitrate, and an extra calcination step would be of interest to ensure the proper fabrication of the material. $LaFe_{1-x}Mg_xO_{3-\delta}$ does have structural similarities to $LaGa_{1-x}Mg_xO_{3-\delta}$ and as such, might enhance the understanding of dopant influence on materials such as LSGM, that have important fuel cell applications.

Appendix I

Kröger-Vink Notation

For impurity N on M site for N^{3+} and M^{4+} cations, and X anion:

$$N_2M_3 \xrightarrow{MX_2} 2\,N_M' + V_x^{\bullet\bullet} + 3X_x^x$$

Where,

- • Represents positive charge
- ' Represents negative charge, and
- x Represents neutral charge

Defect Nomenclature definitions:[1]

For a fixed proportion of M lattice sites to X lattice sites ina crystal MX:

- M_M M atom on M site
- X_X X atom on X site
- M_i M atom on interstitial site
- X_i X atom on interstitial site
- N_M Impurity N on M site
- V_M Vacancy on M site
- V_X Vacancy on X site
- e' Electron in conduction band
- $h^{\bullet}$ Hole in valence band

[1] Based on F. A. Kröger et al., Philips Research Reports, 1959, **14**, 557

Appendix II

1260 Solartron AC Impedance/Gain Phase Analyser Settings

Generator amplitude	2.000E-01 V
Generator Bias	+0.000E00 V
Autointegration	0
Integration time	Int.t (sec): +1.000E+01
Min Frequency	1.00E-01 Hz
Max Frequency	1.00E+6 Hz
Sweep inc	Log Down pts/sweep 40
Monitor enable	00
Monitor voltage limit	+3.00E+0
Monitor error	+5.00E+0
Monitor current limit	+6.00E-2
Current measure resistor	9.9999E-3 ohm
Temp and Pressure on/off	ON
Nyquist plot & initialising	Plot On, No Init
Multiplexer channel set	Only 1 multiplexer channel
Frequency	+1.00E-1 Hz
Waveform	0
Current amplitude	0.00E+0 mA
Current bias	0.00E+0 mA
Delay	0.00 sec
Range	ch1 auto ch2 auto ch3 auto
Coupling	ch1DC ch2 DC ch3 DC
Input	ch1 diff ch2 single
Outer	ch1 ground ch2 ground
Source	Z1
V,I,Z Coord.	V: a,b,I: a,b,Z: R,Z
Bell	on
Variable	freq
Phase	norm
V-amplitude	v.ampl min: +0.0E0V Max: 3.0E0V
V-Bias	v.bias min: +0.0E0V Max: 0.0E0V

Appendix III

Calculation for P_{O_2}

P_{O_2} Sensor Transform, used to convert mV to P_{O_2} in atm., using an 8 mol% yttria stabilised zirconia sensor running at 1000 °C

n=4
Pair=0.21
R=8.3145
F=96485
a=-5.803
b=25922

f=3; column no. for mV versus air (input)
g=6; column no. for PO2 of sample (output)

Csens=1000 ;Sensor temp (deg C)
Csamp=col(5) ; Sample temp (deg C)

E=col(f) mV reading from P_{O_2} sensor

Tsens=Csens+273
Tsamp=Csamp+273

Ksens=10^(a+b/Tsens)

Ksamp=10^(a+b/Tsamp)

Psens=exp(E*n*F/R/Tsens/1000)*Pair

Psamp=Psens*Ksens/Ksamp

Col(g)=Psamp

Curve Fit Transform

[Parameters]
si=5 Approximate starting values for i,n and p,
sn=0.001
sp=5

[Variables]
x=col(6) col(6)=conductivity
y=col(7) col(7)=P_{O_2}(atm.)
w=1/y

[Equations]
sigtot=si+sn*x^-0.25+sp*x^0.25 fit to equation 2.7

fit sigtot to y weight w

[Constraints]

[Options]
stepsize=1

Density correction and Theoretical density transform

AVGN=6.02205*10e23	Avogadro's number (mol^{-1})
SR=87.62	Strontium – atomic mass
CE=140.12	Cerium – atomic mass
YT=88.9059	Yttrium – atomic mass
OX=16	Oxygen – atomic mass
X=col(1)/100	col(1) is % YT
FW=SR+CE*(1-x)+YT*x+OX*(3-x/2)	calculating formula weight using $SrCe_{1-x}Y_xO_{3-x/2}$
col(4)=FW	
col(5)=FW*4	
col(7)=col(5)/AVGN/col(6)*1e-24)	col(6) is unit cell volume from XRD/unit cell volume results, gives calculated density
col(9)=col(8)/col(7)*100	gives theoretical density (%)
p=(100-col(9))/100	
corf=1/(1-3*p/2)	from equation 4.1, mitoff correction factor, taking into account density, when calculating total conductivity
col(10)=corf	

Appendix IV

X-Ray diffraction data for gallium, gadolinium and iron based oxides. The data is sourced from standard JCPDS files.

NdGaO3

Neodymium Gallium Oxide

Rad.: CrKa λ: 2.2909 Filter: V Beta. d-sp: Debye-Shcerrer

Cut off: Int.: Estimation I/Icor.:

Ref: Marezio, Remeika, Dernier, Inorg. Chem., 7, 1337 (1968)

Sys.: Orthorhombic S.G.:

a: 5.431 b: 5.499 c: 7.710 A: 0.9876 C: 1.4021

α: β: γ: Z: [4] mp:

Ref: Ibid.

Dx: 7.557 Dm: SS/FOM: F_{30}=2(.117,112)

C.D. Cell: a=5.499, b=7.710, c=5.431, a/b=0.7132, c/b=0.7044, S.G.=. Mwt: 261.96. Volume[CD]: 230.26.

d Å	Int	h	k	l	d Å	Int	h	k	l
3.84000	40	0	0	2	1.22100	60	3	3	2
3.44000	40	1	1	1	1.21900	70	1	1	6
2.74400	40	0	2	0	1.21700	40	4	2	0
2.72000	100	2	0	0	1.21100	70	2	4	1
2.58300	40	0	2	1	1.20500	40	2	2	5
2.31800	40	2	1	1	1.20200	20	4	2	1
2.23300	50	0	2	2	1.17300	20	4	1	3
2.21600	50	2	0	2	1.15300	60	1	3	5
2.13700	40	1	1	3	1.15100	60			
1.92700	70	0	0	4					
1.87100	50	2	2	1					
1.72100	20	3	1	0					
1.69200	50	1	3	1					
1.67700	20	3	1	1					
1.57900	60	0	2	4					
1.56800	70	3	1	2					
1.54200	20	0	0	5					
1.43700	50	1	3	3					
1.37300	40	0	4	0					
1.36300	60	2	2	4					
1.35700	40	4	0	0					
1.27000	50	3	3	1					
1.22600	40	2	4	0					

Gd2O3

Gadolinium Oxide

Rad.: CuKa λ: 1.5418 Filter: Graph Mono. d-sp: Diffractometer

Cut off: 15.0 Int.: Diffract. I/Icor.: 0.9

Ref: Martin, K., McCarthy, G., North Dakota State University, Fargo, North Dakota, USA, ICDD Grant-in-Aid, (1990)

Sys.: Monoclinic S.G.: C2/m (12)

a: 14.095(2) b: 3.5765(1) c: 8.7692(6) A: 3.9410 C: 2.4519

α: β: 100.08(1) γ: Z: 6 mp:

Ref: Ibid.

Dx: 8.298 Dm: SS/FOM: F_{30}=35(.0127, 67)

Color: White
Peak height intensity. Sample obtained from Research Chemicals of Phoenix, Arizona, USA. Sample annealed for 48 hours at 1300 C. Average relative standard deviation in intensity of the ten strongest reflections for three specimen mounts=2.6%. Validated by calculated pattern. 03 Sm2 type. Silicon used as an internal stand. Single-crystal data used. PSC: mC30. To replace 12-474. Mwt: 362.50. Volume[CD]: 435.24.

d Å	Int	h	k	l	d Å	Int	h	k	l
5.95000	6	$\bar{2}$	0	1	1.66570	18	$\bar{4}$	0	5
3.98900	6	$\bar{2}$	0	2	1.66570	18	6	0	3
3.43000	5	$\bar{4}$	0	1	1.65730	17	$\bar{5}$	1	4
3.40800	16	2	0	2	1.65240	24	0	2	2
3.16700	71	1	1	1	1.65240	24	7	1	1
3.04000	77	4	0	1	1.63830	6	5	1	3
2.97000	100	$\bar{4}$	0	2	1.63370	4	3	1	4
2.87800	60	0	0	3	1.61120	2	2	0	5
2.83000	81	$\bar{3}$	1	0	1.58340	3	2	2	2
2.76100	77	$\bar{1}$	1	2	1.57310	10	$\bar{1}$	1	5
2.64800	3	1	1	2	1.54980	6	$\bar{3}$	1	5
2.50800	3	2	0	3	1.54080	15	4	2	1
2.31300	12	6	0	0	1.53170	16	$\bar{4}$	2	2
2.26300	4	$\bar{1}$	1	3	1.53000	14	7	1	2
2.19900	16	$\bar{5}$	1	1	1.51960	14	1	1	5
2.17100	7	$\bar{2}$	0	4	1.51960	14	0	2	3
2.16600	7	1	1	3	1.51380	7	$\bar{2}$	2	3
2.13500	37	$\bar{3}$	1	3	1.48500	5	$\bar{6}$	0	4
1.91800	36	3	1	3	1.46080	2	$\bar{2}$	0	6
1.90550	7	6	0	2	1.45840	3	$\bar{5}$	1	5
1.87420	3	$\bar{5}$	1	3	1.45610	2	6	0	4
1.86920	4	$\bar{1}$	1	4	1.45610	2	2	2	3
1.85510	4	5	1	2	1.43880	4	0	0	6
1.79640	9	1	1	4	1.43500	3	$\bar{9}$	1	1
1.78840	17	0	2	0	1.42050	2	$\bar{6}$	2	1
1.76140	10	$\bar{8}$	0	1	1.42050	2	$\bar{4}$	0	6
1.75020	5	0	2	1	1.41630	3	$\bar{9}$	1	0
1.71190	5	$\bar{2}$	2	1	1.41450	2	$\bar{6}$	2	0
1.70200	28	$\bar{7}$	1	2	1.41450	2	$\bar{9}$	1	2

d Å	Int	h	k	l
1.36260	2	9	1	1
1.36260	2	2	0	6

15-0196 Wavelength= 2.2909

GdFeO3

Gadolinium Iron Oxide

Rad.: CrKa λ: 2.2909 Filter: d-sp:

Cut off: Int.: Estimation I/Icor.:

Ref: Geller, Wood, Acta Crystallogr., 9, 563 (1956)

Sys.: Orthorhombic S.G.: Pbnm (62)

a: 5.346 b: 5.616 c: 7.668 A: 0.9519 C: 1.3654

α: β: γ: Z: 4 mp:

Ref: Ibid.

Dx: 7.533 Dm: SS/FOM: F_{30}=9(.066, 51)

Cell made up of 4 distorted perovskite units. C.D. Cell: a=5.616, b=7.668, c=5.346, a/b=0.7324, c/b=0.6972, S.G.=Pnma(62). PSC: oP20. Plus 11 additional reflections to 1.152. Mwt: 261.10. Volume[CD]: 230.22.

d Å	Int	h	k	l	d Å	Int	h	k	l
3.88000	70	1	1	0	1.54400	40	2	2	3
3.83100	10	0	0	2	1.45300	70	1	3	3
3.46100	80	1	1	1	1.42600	20	1	1	5
2.81000	70	0	2	0	1.41600	10	3	1	3
2.72500	100	1	1	2	1.38000	40	0	4	1
2.67700	70	2	0	0	1.36200	70	2	2	4
2.63600	50	0	2	1	1.34600	30	0	2	5
2.30400	30	2	1	1	1.33700	40	1	4	1
2.26800	40	0	2	2	1.28200	20	4	1	1
2.20000	50	2	0	2	1.27200	70	3	1	4
2.13400	50	1	1	3	1.26600	20			
2.08300	10	1	2	2	1.23000	20	0	4	3
1.93600	70	2	2	0	1.22600	70	2	4	1
1.91600	40	0	0	4	1.22300	40	3	3	2
1.89000	50	0	2	3					
1.87700	50	2	2	1					
1.75700	20	2	1	3					
1.74100	10	3	0	1					
1.72000	80	1	3	1					
1.70000	10	3	1	0					
1.65900	30	3	1	1					
1.60400	50	1	3	2					
1.58300	50	0	2	4					
1.55800	20	2	0	4					
1.55300	90	3	1	2					

33-0701 Wavelength= 1.5405 *

LaCrO3

Lanthanum Chromium Oxide

Rad.: CuKa1 λ: 1.5405 Filter: Mono. d-sp: Guinier

Cut off: Int.: Film I/Icor.:

Ref: Wustenberg, H., Hahn, Inst. fur Kristallogr., Technische Hochschule, Aachen, Germany, ICDD Grant-in-Aid, (1981)

Sys.: Orthorhombic S.G.: Pnma (62)

a: 5.5157 b: 7.7596 c: 5.4796 A: 0.7108 C: 0.7062

α: β: γ: Z: 4 mp: 2430

Ref: Ibid.

Dx: 6.766 Dm: SS/FOM: F_{30}=47(.0068, 95)

Color: Green

Sample was spray-dried from aqueous solution and sintered at 1450 C for 2 hours. Room temperature form. The cell parameters reported in 24-1016 agree with the present data; a number of reflections caused by the orthorhombic distortion are not listed in the rhombohedral structure II (R-3m) at 271 C. Melting point at 2430 C reported by Tresvjatskiy et al., Rev. Int. Haute Temper. Refract., 5 45-50 (1968). Form III. Perovskite type. Silicon used as an internal stand. PSC: oP20. Mwt: 238.90. Volume[CD]: 234.52.

d Å	Int	h	k	l	d Å	Int	h	k	l
3.88700	50	1	0	1	1.16959	12	2	2	4
3.47700	9	1	1	1	1.16959	12	0	6	2
2.75800	65	2	0	0	1.12380	14	4	4	0
2.74700	100	1	2	1	1.11904	12	0	4	4
2.74000	90	0	0	2					
2.34700	9	2	1	1					
2.24800	50	2	2	0					
2.23800	55	0	2	2					
1.94400	70	2	0	2					
1.94000	60	0	4	0					
1.88600	5	2	3	0					
1.88600	5	2	1	2					
1.74320	5	3	0	1					
1.73630	8	1	4	1					
1.69250	7	1	1	3					
1.59000	60	3	2	1					
1.58660	40	2	4	0					
1.58310	60	0	4	2					
1.58310	60	1	2	3					
1.37890	14	4	0	0					
1.37300	40	2	4	2					
1.36980	14	0	0	4					
1.29650	7	3	4	1					
1.29280	8	1	4	3					
1.23178	12	4	0	2					
1.22905	25	3	2	3					
1.22699	30	1	6	1					
1.22699	30	2	0	4					
1.21167	6	2	1	4					
1.17409	7	4	2	2					

La4Ga2O9

Lanthanum Gallium Oxide

Rad.: CuKa λ: 1.5418 Filter: Ni Beta.M d-sp: Diffractometer

Cut off: Int.: Diffract. I/Icor.:

Ref: Mizuno, M., Government Industrial Research Institute, Nagoya, Japan, Private Communication, (1986)

Sys.: Monoclinic S.G.:

a: 7.974 b: 10.968 c: 11.569 A: 0.7270 C: 1.0548

α: β: 108.30 γ: Z: mp: 1704

Ref: Ibid.

Dx: Dm: SS/FOM: F_{30}=4(.032,235)

εα: 1.93 ηωβ: εγ: 1.95 Sign: 2V:

Ref: Ibid.

Sample fused with a solar furnace and air quenched. Pattern made at 25 C. C.D. Cell: a=11.569, b=10.968, c=7.974, β=108.30, a/b=1.0548, c/b=0.7270, S.G.=. Mwt: 839.06. Volume[CD]: 960.64.

d Å	Int	h	k	l	d Å	Int	h	k	l
7.77500	8	0	1	1	1.80300	7	0	6	1
5.49000	6	0	0	2	1.75200	4	4	1	1
4.90000	8	0	1	2	1.71800	10	[$\bar{4}$	3	3]
4.90000	8	0	2	1	1.70500	6	4	1	$\bar{5}$
4.77000	3	1	1	$\bar{2}$	1.68800	5	[4	2	1]
3.86500	6	0	2	2	1.68500	5	2	3	$\bar{6}$
3.47000	25	0	1	3	1.66000	3	2	6	$\bar{1}$
3.22100	100	2	2	$\bar{1}$	1.64600	2	4	3	$\bar{4}$
3.11200	20	2	2	0	1.64600	2	4	2	$\bar{5}$
3.04500	65	0	2	3	1.63600	2	0	6	3
3.04500	65	0	3	2					
3.04200	45	1	3	1					
2.74000	5	0	4	0					
2.73700	10	2	0	2					
2.65500	10	2	1	$\bar{2}$					
2.65300	7	2	0	$\bar{4}$					
2.60100	6	[1	2	3]					
2.60100	6	2	3	$\bar{2}$					
2.43700	3	2	3	1					
2.39800	2	2	3	$\bar{3}$					
2.19000	7	2	3	2					
2.14500	10	2	3	$\bar{4}$					
2.14500	10	3	3	$\bar{1}$					
2.10000	3	2	4	1					
1.99000	15	1	4	$\bar{4}$					
1.93700	15	2	4	2					
1.91700	6	2	1	4					
1.90300	5	$\bar{2}$	3	5					
1.82000	10	2	5	1					

05-0602 Wavelength= 1.5405 *

La2O3

Lanthanum Oxide

Rad.: CuKa1 λ: 1.5405 Filter: Ni Beta.M d-sp:

Cut off: Int.: Diffract. I/Icor.:

Ref: Swanson, Fuyat, Natl. Bur. Stand. (U.S.), Circ. 539, III, 33 (1954)

Sys.: Hexagonal S.G.: $P\bar{3}m1$ (164)

a: 3.9373 b: c: 6.1299 A: C: 1.5569

α: β: γ: Z: 1 mp:

Ref: Ibid.

Dx: 6.574 Dm: SS/FOM: F_{30}=47(.0160, 40)

Color: Colorless
Pattern taken at 26 C. Sample from Fairmount Chemical Company. Sample was annealed at 1200 C for one hour and mounted in petrolatum to prevent reabsorption of C 02 + H2 0. Spectroscopic analysis: <0.01% Ca, Mg, Si; <0.001% Al, Cu, Fe, Pb. Merck Index, 8th Ed., p. 608. Opaque mineral optical data on specimen from Nanseke, Uganda: R3R%=14.2, Disp.=Std., VHN100=782-813, Ref.: IMA Commission on Ore Microscopy QDF. Pattern reviewed by Holzer, J., McCarthy, G., North Dakota State Univ., Fargo, ND, USA, ICDD Grant-in-Aid (1990. Validated by calculated pattern except for the following: 2.278 23 102; 1.968 28 110; 1.753 23 103. Calculated pattern indicates that the following reflections might be observable: 6.130 <1 001; 2.043 <1 003; 1.8744 <1 111; 1.4177 <1 113; 1.2260 <1 005. La2 03 type. PSC: hP5. Mwt: 325.81. Volume[CD]: 82.30.

d Å	Int	h	k	l	d Å	Int	h	k	l
3.41000	34	1	0	0	.844300	1	4	0	1
3.06300	31	0	0	2	.828300	2	2	2	4
2.98000	100	1	0	1	.805000	1	3	1	4
2.27800	58	1	0	2	.800700	2	2	1	6
1.96800	63	1	1	0					
1.75300	52	1	0	3					
1.70500	4	2	0	0					
1.65600	24	1	1	2					
1.64200	17	2	0	1					
1.53200	3	0	0	4					
1.49000	5	2	0	2					
1.39800	2	1	0	4					
1.30900	7	2	0	3					
1.28900	2	2	1	0					
1.26100	12	2	1	1					
1.20900	6	1	1	4					
1.18790	4	2	1	2					
1.15380	4	1	0	5					
1.13960	2	2	0	4					
1.13670	4	3	0	0					
1.09010	7	2	1	3					
1.06580	4	3	0	2					
1.02200	<1	0	0	6					
.995200	3	2	0	5					
.984000	3	2	2	0					
.978700	1	1	0	6					
.945900	<1	3	1	0					
.937200	3	2	2	2					
.934500	5	3	1	1					
.913100	2	3	0	4					
.907000	2	1	1	6					
.888300	5	2	1	5					
.876600	1	2	0	6					
.858300	4	3	1	3					
.848000	2	1	0	7					

La2MgOx

Magnesium Lanthanum Oxide

Rad.: CuKa1 λ: 1.5406 Filter: Graph Mono. d-sp: Diffractometer

Cut off: Int.: Diffract. I/Icor.:

Ref: Acharya, B., Muralidhar, J., Rajeev, Pradhan, L., Regional Research Lab., Orissa, India, ICDD Grant-in-Aid, (1991)

Sys.: S.G.:

a: b: c: A: C:

α: β: γ: Z: mp:

Ref:

Dx: Dm: SS/FOM: F =<1(,)

0 assigned because unindexed. Lanthanum and magnesium chloride solutions mixed in La2 03:MgO- molecular proportions and the hydroxides were precipitated by the addition of sodium carbonate solution: filtered and washed. The precipitate was heated at 850 C and 1000 C for 4 hours respectively. For the formula, x=4+δ. Silicon used as an external stand. Delete: formula incorrect, La (O H)3; WFM 12/94.

d Å	Int	h	k	l	d Å	Int	h	k	l
5.68000	100				1.08700	10			
3.27000	97				1.08400	10			
3.19000	93				1.03900	13			
2.88000	5				1.03700	13			
2.83000	32				1.02900	12			
2.50000	8								
2.28000	85								
2.14000	22								
2.11000	3								
1.93000	13								
1.89000	68								
1.87000	93								
1.83000	10								
1.66000	22								
1.63000	17								
1.59000	7								
1.57000	10								
1.45400	27								
1.43500	8								
1.41900	3								
1.41400	5								
1.34900	17								
1.32900	8								
1.29800	3								
1.24800	10								
1.23400	34								
1.17200	7								
1.10300	10								